UNDERSTANDING SHAPE CONTROL IN GOLD NANOPARTICLES FROM MOLECULAR DYNAMICS SIMULATIONS

Dissertation

"zur Erlangung des Grades"

Doktor der Naturwissenschaften

im Promotionsfach FB09

am Fachberich Chemie, Pharmazie und Geowissenschaften

der Johannes Gutenberg-Universität Mainz

SANTOSH KUMAR MEENA

Mainz, 2016

JOHANNES GUTENBERG
UNIVERSITÄT MAINZ

Date of the Exam: 20 April, 2016

ABSTRACT

Gold nanoparticles are widely used in many areas such as photothermal cancer therapy, biochemical sensing and medical imaging due to their size and shape-dependent optical properties. Directly manipulating and controlling the size and shape of gold nanoparticles is, therefore, a key step for their tailored applications.

We use molecular dynamics simulations in order to understand the microscopic origin of the asymmetric growth mechanism in gold nanorods. The different factors influencing the growth are selectively included in the models in order to unravel the role of the surfactants and ions. In particular, both infinite planes models, representing the mature stage of the growth, and nanoseed models in the size of a few nanometers are used to understand how asymmetry between the different facets of the nanorods builds up.

We find that on all the investigated surfaces, cetyltrimethylammonium bromide forms a layer of distorted cylindrical micelles where channels among micelles provide direct ion access to the surface. When the low index facets are examined, a lower surface density of surfactant is found on the Au(111) facets, with respect to the Au(100) and Au(110) facets. In addition, a higher electrostatic potential difference is measured between the gold surface and the bulk solution at the Au(111) interface, which would provide a stronger driving force for the diffusion of negatively charged $AuCl_2^-$ species, which are reduced at the gold surface. The two factors together would result into higher diffusion flux of the gold reactant toward the Au(111) facets and could result into a preferential growth of the Au(111) surfaces.

In order to investigate if the anisotropy is preserved at the nanoscale, we also investigate penta-twinned decahedral seeds and a cuboctahedral seed, whose dimensions are comparable to those of the cetyltrimethylammonium

bromide micelle. We find that the asymmetry in adsorption behavior between the different low index facets, which characterized the infinite planes, shows up even more dramatically on the nanoseeds. Indeed, the Au(100) and Au(110) facets show structures similar to the ones observed on the infinite planes in both the cuboctahedral as well as penta-twinned seeds. The (111) facets, which e.g. form the tips of the penta-twinned nanoseeds, on the other hand show basically no micellar adsorption. This huge difference in the coverage of the early stage seeds would then promote a symmetry breaking in the penta-twinned seeds and, therefore, an anisotropic growth of nanocrystals.

Simulations also provides a microscopic understanding of the role of halides in controlling the anisotropic growth. In particular, we find that bromide adsorption on the gold nanorods is not only responsible for surface passivation, but also acts as the driving force for micelle adsorption and stabilization on the gold surface in a facet-dependent way. Partial replacement of bromide by chloride decreases the difference between facets and the surfactant density. Finally, while only chloride is present in the growing solution, no halides or micellar structure protect the gold surface and further gold reduction should be uniformly possible.

Finally, we also address the role of the silver ions. We find that silver ions have a strong propensity to adsorb on the gold surface where they form AgBr islands with different specific geometry depending on the surface plane. Although the structure of the micellar layer is not qualitatively modified by the addition of silver, silver substantially increases the Br^- concentration at the interface, resulting into an increased surface passivation. Overall the asymmetry between facets is maintained, with a lower Br^- surface density at the Au(111) interface with respect to that at the Au(100) and Au(110) interfaces.

ZUSAMMENFASSUNG

Gold-Nanopartikel werden aufgrund ihrer größen- und form-abhängigen optischen Eigenschaften in vielen Bereichen, wie z.B. photothermischer Tumortherapie, biochemischer Sensorik und medizinischer Bildgebung verwendet. Direktes Manipulieren und Steuern der Größe und Form der Metallnanopartikel ist deshalb ein wichtiger Schritt für ihre maßgeschneiderten Anwendungen.

Wir verwenden Moleküldynamiksimulationen, um den mikroskopischen Ursprung des asymmetrischen Wachstumsmechanismus in Gold Nanostäbchen zu verstehen. Die verschiedenen Faktoren, die das Wachstum beeinflussen, werden selektiv in den Modellen angewendet, um die Rolle der Tenside und Ionen zu entschlüsseln. Insbesondere werden sowohl unendliche Ebenen-Modelle, die die reife Phase des Wachstums darstellen, sowie nanoseed Modelle in der Größe von wenigen Nanometern verwendet, um zu verstehen, wie Asymmetrie zwischen den verschiedenen Facetten der Nanostäbchen entsteht um schlussendlich anisotrope Partikel zu formen.

Wir finden, dass Cetyltrimethylammoniumbromid auf allen untersuchten Oberflächen eine Schicht aus verzerrten zylindrischen Mizellen bildet. Zwischen den Mizellen stellen Kanäle den direkten Ionen-Zugang zur Oberfläche bereit. Wenn die niedrig indizierten Kristallfacetten untersucht werden, wird eine geringere Flächendichte des Tensids auf der Au(111) Facette im Vergleich mit den Flächendichten auf den Au(100) und Au(110) Facetten gefunden. Zusätzlich wird eine höhere elektrostatische Potentialdifferenz zwischen der Gold (111) oberfläche und der Lösung gemessen, die eine stärkere Triebkraft für die negativ geladenen $AuCl_2^-$ Spezies liefern würde, die an der Goldoberfläche reduziert wird. Diese beiden Faktoren würden zusammen zu einem höheren Diffusionsstrom der Gold Reaktanden und damit zu einem bevorzugten Wachstum an den Au(111) Oberflächen führen. Um zu

untersuchen, ob die Anisotropie im Nanobereich erhalten bleibt, untersuchen wir auch fünffach verzwillingt-dekaedrische Keime und kuboktaedrischen Keime, deren Abmessungen vergleichbar mit der Größe der Cetyltrimethylammoniumbromid Mizellen ist. Wir zeigen, dass die Asymmetrie im Adsorptionsverhalten des Tensids an den verschiedenen niedrig indizierten Facetten, die auf den unendlichen Ebenen beobachtet wird, sich an nanoseeds noch dramatischer zeigt. Die Au(100) und Au(110) Facetten zeigen ähnliche Strukturen, zu denen die auf den unendlichen Ebenen beobachtet wurden, sowohl auf den kuboktaedrischen wie auch fünffach verzwillingt Keimen. Die Au(111) Facetten hingegen, die unter anderem die Spitzen der fünffach verzwillingt Keime bilden, zeigen im Grunde keine Adsorption. Dieser große Unterschied im Bedeckungsgrad der verschiedenen Facetten auf den frühen Keimen würde dann einen Symmetriebruch in den fünffach verzwillingt Kristallkeimen hervorrufen und damit ein anisotropes Wachstum von Nanokristallen fördern.

Simulationen liefern auch ein mikroskopisches Verständnis der Rolle der Halogenide bei der Steuerung des anisotropen Wachstums. Insbesondere finden wir, dass Bromid Adsorption auf den Gold- Nanostäbchen nicht nur für die Oberflächenpassivierung verantwortlich ist, sondern auch facettenabhängig als die treibende Kraft für die Adsorption und Stabilisierung der Tensidmizelle auf der Goldoberfläche wirkt. Ersetzt man Bromid teilweise durch Chlorid, verringert sich die Differenz in den Tensid-Dichten zwischen den Facetten. Schließlich, wenn nur Chlorid in der Wachstumslösung vorliegt, schützen keine Halogenide oder Mizellenstrukturen die Goldoberfläche und eine weitere Goldreduktion sollte gleichmäßig möglich sein und somit zu isotropem Wachstum führen. Schließlich beschäftigen wir uns auch mit der Rolle der Silberionen. Wir finden, dass Silberionen eine starke Neigung haben, auf der Goldoberfläche zu adsorbieren. Hier bilden sie $AgBr^-$Inseln mit verschiedenen speziell-facettenabhängigen Geometrien. Obwohl die Struktur der micellaren Schicht qualitativ nicht durch die Zugabe von Silber modifiziert wird, erhöht Silber die Br^- Konzentration an der Grenzfläche. Die erhöhte Bromid Konzentration führt zu einer verstärkten

Oberflächenpassivierung. Insgesamt wird die Asymmetrie zwischen den Facetten beibehalten. Die Bromiddichte an der Au(111) Grenzfläche ist signifikant geringer als an den Au(100) und Au(110) Grenzflächen.

PUBLICATIONS

Santosh Kumar Meena and Marialore Sulpizi. Understanding the microscopic origin of gold nanoparticle anisotropic growth from molecular dynamics simulations. *Langmuir*, 29 (48):14954–14961, 2013.

Santosh Kumar Meena, Sirin Celiksoy, Philipp Schäfer, Andreas Henkel, Carsten Sönnichsen, and Marialore Sulpizi. The role of halide ions in the anisotropic growth of gold nanoparticles: a microscopic, atomistic perspective. *Phys. Chem. Chem. Phys.*, 2015 (DOI:10.1039/C6CP01076H).

Santosh Kumar Meena and Marialore Sulpizi. Mechanism of adsorption of CTAB on higher index facets of gold nanorods. 2016 (To be submitted).

ACKNOWLEDGEMENTS

I would like to thank my advisor, Prof. M. S., for guiding and supporting me during these four years, without her guidance and helpful discussion this thesis would not have been possible. I would also like to thank Prof. G. D.for useful discussions.

I am particularly grateful to C. S. and his group for the possibility to establish a very interesting collaboration which provided the experimental validation to the predictions from simulations. I would like to especially thank Dr. A. H. for the useful discussions about the nanorod synthesis which were particularly precious in the formulation of the project. I am also grateful to S. and P. for their experimental contribution to this work.

I would like to thank all my colleagues, L. S., H. G., I. L. G., R. K. and A. L. for their support and for providing a great working atmosphere.

Also, I am very grateful to C. A.and D. R. for their continuous support in the practical and bureaucratic aspect of my life in Mainz.

Finally, a special thank to my family for all their love and encouragement which gave me support and strength all these years.

I thank the Condensed Matter Theory Group KOMET 331 for providing access to its computational facilities and the Deutsche Forschungsgemeinschaft for financial support under grant no. SU 752/1.

All the simulations were performed on the Mogon ZDV cluster.

CONTENTS

LIST OF FIGURES

LIST OF TABLES

1

INTRODUCTION

1.1 INTRODUCTION

Nanoparticles are particles with dimension between 1 and 100 nm. In the field of nanotechnology, the optimized synthesis and development of metal nanoparticles have been accelerating at a rapid pace in the last few decades due to their potential use in a variety of promising applications, including sensing, medical imaging, and photothermal cancer therapy [1]. The properties of nanoparticles are highly dependent not only on material composition but also on size and shape. Therefore, the design and synthesis of nanoparticles with tailored shape and size is a fundamental goal in the nanotechnology.

The electronic confinement by a nanoparticle provides the most powerful means to manipulate the electronic, optical, and magnetic properties of a solid material. In particular, the optical properties of gold and silver nanoparticles are tunable throughout as a function of the size, shape, aggregation state and local environment [2]. For example, gold and silver nanoparticles exhibit strong absorption in the visible, near-infrared spectral range, which is the result of plasmon excitation [3]. The resonance wavelength depends on the surroundings of the particle and especially on its shape [4]–[6]. By synthesizing particles of appropriate shapes, the resonance wavelength can be tuned to a wide spectral range, even to infrared. This effect can be harnessed for example in medicine, to either destroy tissue by local heating or release payload molecules of therapeutic importance. In particular, for the applications in imaging and therapy, gold nanorods of high aspect ratio are required for better absorption of light in a selected spectral

window [1]. Gold nanoparticles can also be conjugated to biologically active moieties, providing possibilities for targeting to particular tissues [7].

Metal nanoparticles are also employed in catalysis. In this case, it is well established that the activity of a metal nanocrystal can be enhanced by reducing its size [8], [9]. The selectivity, however, is most sensitive to the packing of atoms on the surface or the exposed facets of a nanocrystal which is determined by the geometric shape of the nanoparticles [10], [11]. Such examples clearly demonstrate the critical importance of shape control to the efficient utilization of metal nanoparticles in a wide variety of applications.

1.2 SYNTHESIS OF METAL NANOPARTICLES

For the gold nanorods synthesis, several solution based methods such as electrochemical reduction through template-directed or templateless synthesis, seed-mediated growth synthesis and photochemical reduction have been developed. Among these methods, the seed-mediated growth is the most popular approach to the synthesis of gold nanorods due to its procedural simplicity, easily tunable control of the particle aspect ratio, and flexibility of further surface modification.

1.2.1 *Seed-mediated growth technique*

The seed-mediated growth is a two-step synthesis technique. This technique was initially devised by Murphy, El-Sayed and co-workers and includes cetyltrimethylammonium bromide (CTAB) surfactant as the capping agent, gold reactant ($HAuCl_4$), gold seeds, and ascorbic acid as a week reducing agent [12]–[14].

In the first step, metal seeds are prepared, which require the nucleation of seeds and the growth of the seed up to certain minimal size (4-5 nm). The gold seed particles are synthesized separately than the nanorods, *via* the reduction of $HAuCl_4$ using a strong reducing agent, $NaBH_4$ in the pres-

ence of a stabilizing agent. Usually, CTAB, cetyltrimethylammonium chloride (CTAC) and sodium citrate are used as stabilizing agents for gold seeds. Sodium citrate is not a surfactant but it can stabilize the particles by binding on their surface, which in turn prevents the particles aggregation. The use of a strong reducing agent insures the rapid reduction of the gold reactant and simultaneous nucleation, which results into small and monodisperse seed particles in the solution. The choice of the surfactant or stabilizing agent can also affect the crystallinity of seed. E.g., with sodium citrate, multiply twinned and planar-twinned seeds are obtained, while with CTAB mostly single crystalline seeds are obtained (Figure 1.1).

In the second step, the newly formed metal seeds are added to the growing solution which contains the gold reactant in a capping agent solution (CTAB solution) also including the weak reducing agent, ascorbic acid. The gold reactant is selectively reduced by the ascorbic acid from Au^{3+} to Au^{+} in the growing solution before the addition of the seeds. The addition of the seed catalyzes the further reduction of Au^{+} on their surface [12], [14], [16]. Subsequently, a weak reducing agent is chosen to prevent additional nucleation and to favor growth onto the pre-synthesized seeds, as well as to slow particle growth enough to allow for control of nanoparticle shape through the shape directive additives. The strength of ascorbic acid decreases at lower pH values. Reduction of Au^{3+} to Au^{+} by ascorbic acid is rapid, but the reduction from Au^{+} to Au^{0} is very slow and is negligible in the absence of the seed particles. Therefore, the seed particles act as a catalyst for the second reduction step of the gold reactant.

This process was slightly modified by including $AgNO_3$ in the growing solution with CATB and ascorbic acid. Yield of nanorods is raised to nearly 100% by Ag^{+} ions, compared to 20-40% in the absence of Ag^{+}. However, the highest aspect ratio of the gold nanorods obtainable with silver ion is about 6, compared to 25 in the absence of silver. In particular, short gold nanorods with higher yield are obtained in the presence of silver ions, while the longer gold nanorods with lower yield are obtained without silver ions [13], [14].

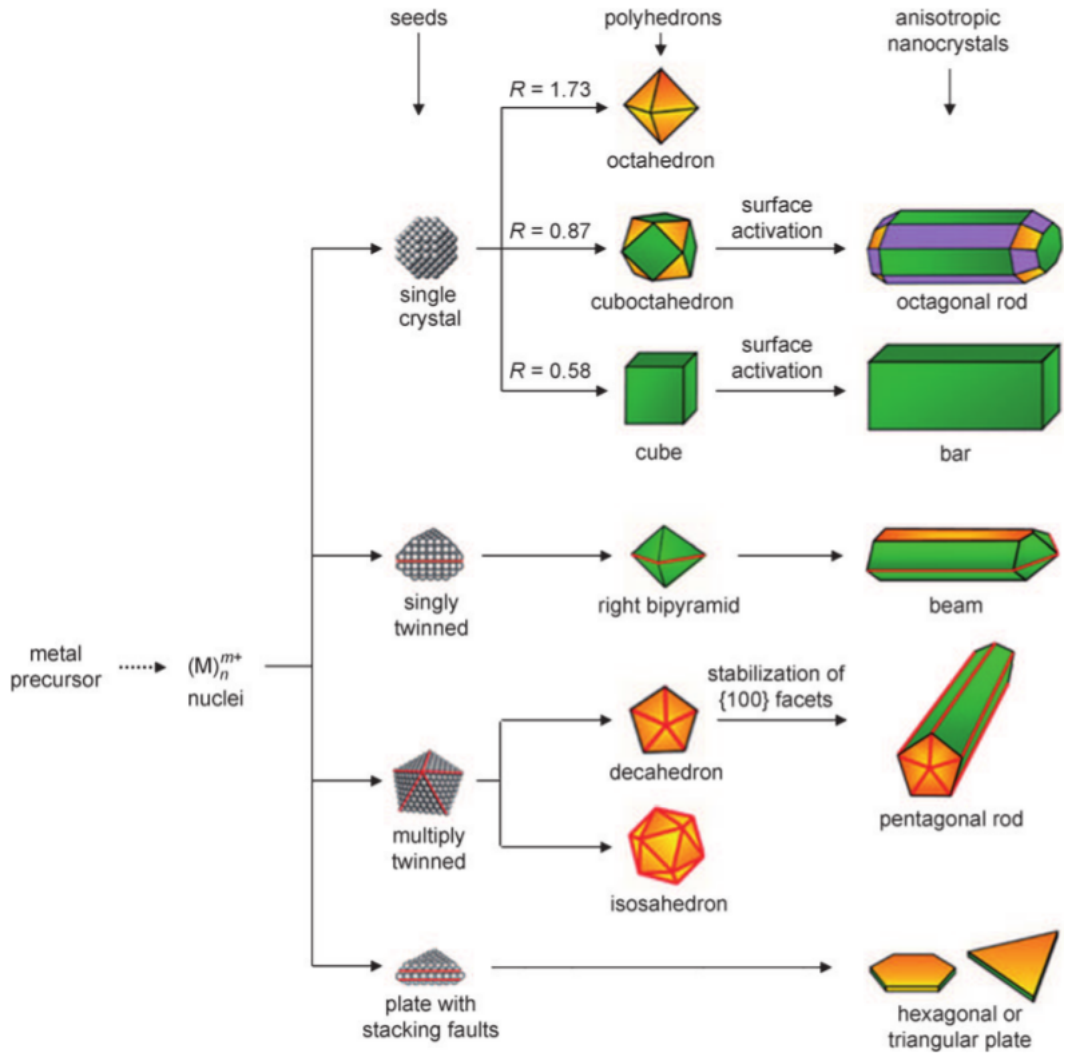

Figure 1.1: The reaction pathway which leads to fcc metal nanocrystals with different shapes. First, a precursor is reduced or decomposed to form the nuclei. Once the nuclei have grown past a certain size, they become seeds with a single-crystal, singly twinned, or multiply twinned face areas than a cube of the same structure. If stacking faults are introduced, plate-like seeds will be formed. The green, orange, and purple colors represent the Au(100), Au(111) and Au(110) facets, respectively. Twin planes are drawn with red lines. The parameter R is defined as the ratio between the growth rates along the (110) and (111) directions. This figure has been adopted from the ref. [15].

Other surfactants and reducing agents have been used to produce gold nanorods, but they were unable to provide the same finely tunable control over the morphology if used without CTAB [17]. In addition, it has

been shown that the purity of CTAB highly influences the ability to synthesize gold nanorods [18]. In certain synthesis recipes for gold nanoparticles, halide ions (chloride, bromide and iodide) are also present in water in addition to the surfactant [16], [18]–[31]. These anions significantly influence the morphology of gold nanoparticles during their growth [32], [33]. The use of CTAC or the introduction of KI to the synthesis can completely change the morphology of the primary product [29]. Smith *et al.* showed that low concentrations (<3.0 ppm) of iodide impurities present in CTAB would prevent the formation of gold nanorod in the silver-assisted synthesis [18], [23]. When the iodide concentration in the CTAB rises above 50 μM, the formation of pentagonally twinned nanorods is suppressed and nanoprisms/nanoplates are obtained. Zhang *et al.* demonstrated that the use of CTAB led to the formation of tetrahexahedra, while the use of CTAC promoted the formation of concave cubes [26]. Mirkin *et al.* showed that the ratio of silver nitrate to halide and the selection of the appropriate halide counterion with cetyltrimethylammonium cation (CTA^+) could be used to rationally prepare a variety of anisotropic gold nanoparticles [29]. In the presence of bromide as counterions with CTA^+ mostly well defined gold nanorods are obtained, while in the presence of chloride as counterions mostly spherical particles are obtained. In the presence of iodide as counterions, nanoprisms/nanoplates or irregularly shaped particles are obtained (Figure 1.2).

Considering the fact that growth of the nanoparticles takes place in rather a complex environment, one need to systematically examine the role of shape of initial seed, surfactant, halide ions and silver ions [20], [21], [32]–[35].

1.3 THERMODYNAMIC AND KINETIC ASPECTS OF NANOPARTICLES GROWTH

If one considers the synthesis of nanoparticles as a chemical reaction like the organic compounds, the atoms derived from a metal reactant can be viewed as reactants while the nanoparticles with different shapes being products. Figure 1.3a shows a schematic illustration which is typically used in the

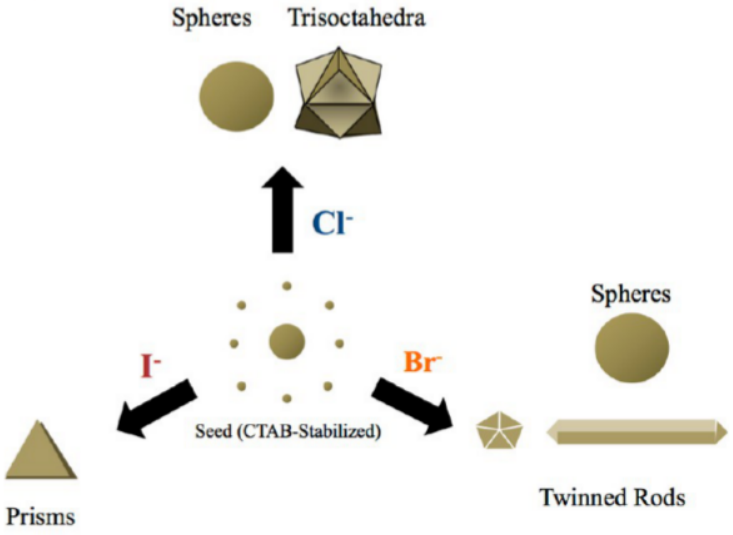

(a)

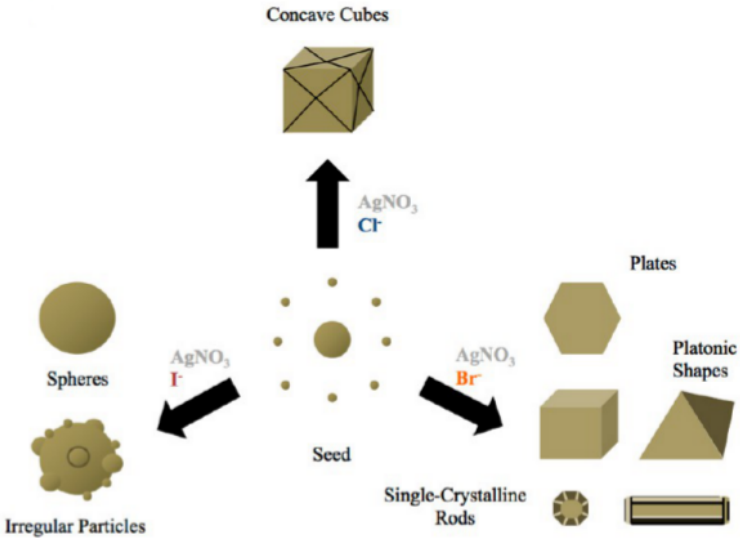

(b)

Figure 1.2: Schematic representation of gold nanoparticles shapes typically formed using each halide (a) in the absence of silver nitrate and (b) in the presence of silver nitrate. This figure has been adopted from the ref. [33].

literature to explain the concept of thermodynamic versus kinetic control. In this case, the product I (nanoparticle with shape I) is thermodynamically less stable than the product II (nanoparticle with shape II). However, the activation energy barrier E_a involved in the formation of product I is lower than that for the formation of product II. As a consequence product II, with a lower energy, will be in dominance when the synthesis is conducted under

thermodynamic control, whereas product I will be prevalent if the synthesis is switched to the condition of the kinetic control.

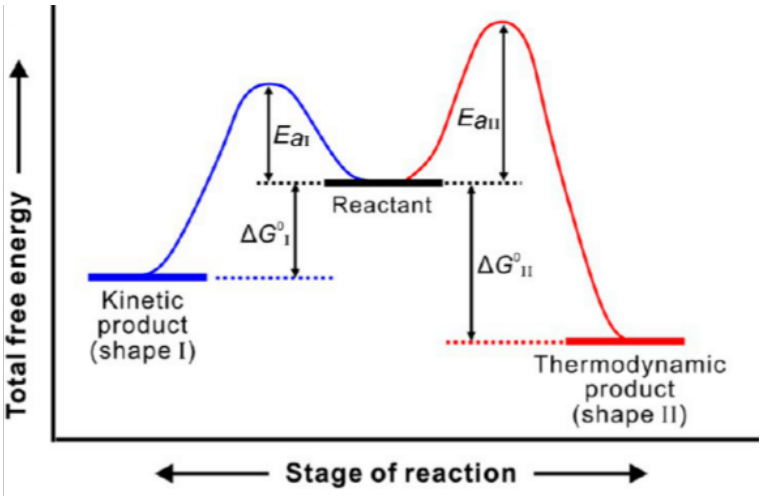

(a)

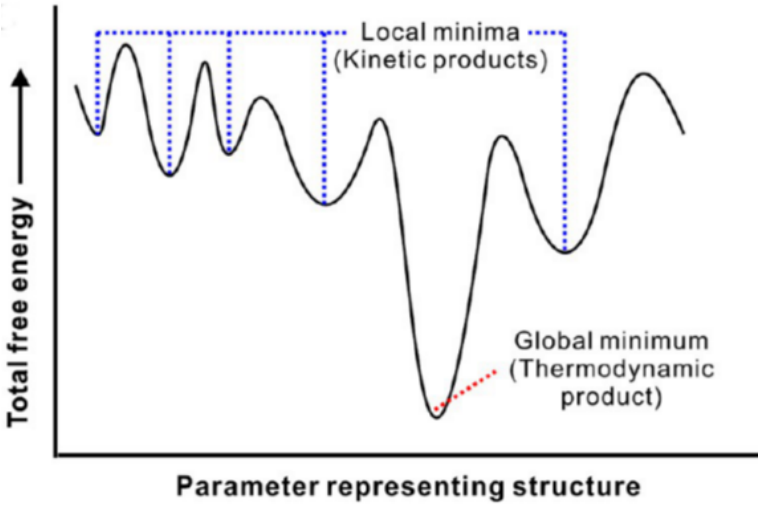

(b)

Figure 1.3: Schematic representation of two different scenarios of thermodynamic versus kinetic control that involve (a) two parallel reactions and (b) a series of sequential reactions. In both scenarios the thermodynamic product, which is with the one with the lowest Gibbs free energy is highlighted. This figure has been adopted from the ref. [36].

The main difference between the synthesis of nanoparticles and organic compounds is that nanoparticles may also correspond to the products of a set of sequential reactions, as described in the energy landscape of Figure 1.3b. In this scenario, thermodynamically controlled products would

be represented by the global minimum in the Gibbs free energy. However, the product could be easily trapped in many states (or nanoparticle shapes) corresponding to local minima when the synthesis is conducted under kinetically controlled conditions.

The shape obtained under thermodynamic control can be considered as an equilibrium state defined by a set of experimental parameters, including temperature, pressure, and surrounding medium. As such, whenever there is a perturbation to any one of these parameters, the state and thus the shape will be altered accordingly.

In general, a nanoparticle should be in its equilibrium shape when its total Gibbs free energy reaches the global minimum. The total Gibbs free energy of a nanoparticle can be expressed as the sum of a term for the bulk and an excess term caused by the surface (Equation 1.1):

$$\delta G = \delta G_{bulk} + \gamma \delta A \tag{1.1}$$

where γ denotes the specific surface free energy (per unit area) and A is the surface area. At a fixed volume, the total Gibbs free energy will reach the minimum value under the condition of a minimized total surface free energy (Equation 1.2):

$$\int \gamma_i \delta A_i = \text{minimum} \tag{1.2}$$

where the integral is taken over the entire surface of a nanoparticle. This equation implies that a nanoparticle should take an equilibrium shape when its total surface free energy is minimized. If the specific surface free energy does not depend on the direction, as in an isotropic system like a noncrystalline material (a liquid or an amorphous solid), the total surface free energy is solely proportional to the total surface area. In this case, the total surface free energy will be minimized when the nanoparticle has a spherical shape, which minimizes the total surface area at a fixed volume. For a crystalline material, however, the surface free energies of different crystallographic planes tend to differ from each other because of the intrinsic anisotropy in atomic arrangement. As a result, one has to know the specific

surface free energies of different crystallographic planes in order to derive the equilibrium shape of a nanoparticle in a vacuum. The specific surface free energy is defined as the increase in free energy per unit area when a new surface is created. When atoms are tightly bound to each other, the bonds between them need to be broken in order to create a pair of new surfaces. In a sense, the surface free energy reflects the cost in energy when bonds are broken and is thus determined by the number and strength of bonds involved. Theoretically, the equilibrium shape of a nanocrystal in a vacuum can be derived using the Wulff construction [37]–[39].

According to Wulff theorem, a single-crystal seed made of an fcc metal grows in vacuum under thermodynamic control should evolve isotropically into a truncated octahedron with increasingly larger sizes. The lattice of a metal has a highly symmetric structure, so there is no intrinsic driving force for it to grow anisotropically with geometric symmetry different from its unit cell. A single-crystal seed made of an fcc metal, tends to grow with an isotropic shape such as cube, cuboctahedron, or octahedron depending on the relative growth rates along the (100) and (111) directions. Since the equilibrium shape of a nanoparticle is determined by the relative magnitudes of specific surface free energies associated with different crystallographic facets, it is possible to alter the ratios between the specific surface free energies to obtain nanoparticles with shapes other than the one predicted using the Wulff theorem. In particular the equilibrium shape of a nanocrystal can be modified in gas phase by the presence of an adsorbate, which can effectively reduce the specific surface free energy [40]–[44].

Analogously, when considering the growth in solution, capping agents can also change the equilibrium shape. Capping agents such as halide ions, surfactant, small molecules, or macromolecules, can selectively bind to different types of facets altering the specific surface free energies and thus, in turn, their proportions in terms of area. When a capping agent is introduced into a growing solution, the type of facet stabilized by the capping agent will exhibit a lower specific surface free energy, leading to the forma-

tion of nanoparticles with a shape that maximizes the expression of that type of facet.

In addition to the Wulff theorem, the shape taken by a growing nanoparticle can also be understood from a kinetic perspective on the basis of the relative growth rates of different crystallographic planes. Since the capping agent, chemisorbed or physisorbed on a facet, will hinder or prevent the deposition of atoms onto this facet, surface capping will eventually lead to the formation of a shape with that particular facet preferentially expressed. In other words, the facet covered by the capping agent will take a slower growth rate and thus a greater proportion on the surface.

Packing densities of the capping agent on the surfaces of nanoparticles are often unknown. As a result, an excess amount of the capping agent has to be introduced into a synthesis to ensure effective passivation of the newly formed surface in order to control the size and shape of the growing nanopaticles. Most of these syntheses lack a mechanistic understanding and/or experimental control.

Anisotropic nanoparticles can only be obtained by breaking the intrinsic confinement imposed by the cubic symmetry of its unit cell during the course of growth. In general, anisotropy can be introduced through three major mechanisms: (i) incorporation of twin defects or stacking faults into the crystal lattice in the nucleation step; (ii) induction of an asymmetric deposition pattern for a symmetric seed in the growth step; and (iii) aggregation or attachment of seeds during growth. The first approach can naturally break the symmetry of an fcc lattice through the inclusion of twin defects. These kinds of twin defects and asymmetric pattern can be introduced using surface adsorption of chemical species (atomic, ionic, molecular such as capping agents, or macromolecular) in the solution phase. As a result, decahedral, icosahedral, and plate-like seeds are formed in growth solution with followed by their growth into five-fold twinned nanorods or nanowires with a pentagonal cross-section or nanoplates with a triangular or hexagonal profile [15].

Despite the collective effort for controlling the shape of nanoparticles in the past, the mechanisms responsible for the appearance of twin defects or stacking faults during self-nucleation of seed and its anisotropic growth is still unknown or not complete. Mechanisms revealing the role played by a capping agent in manipulating the shape of a nanoparticle at an atomic/-molecular level are required.

1.4 GROWTH OF GOLD NANORODS: PROPOSED MECHANISMS

In the following we will focus our discussion on the anisotropic growth of the gold nanoparticles with particular emphasis to the adsorption of the capping agents on different surfaces and their implication for the asymmetric growth.

1.4.1 *Growth without silver ions*

The mechanism of formation of rod-shaped gold nanoparticles in aqueous surfactant media remains unclear or incomplete. Some experimental groups, proposed that CTAB absorbs on the gold nanorod surface in the form of a bilayer, with the trimethylammonium headgroups of the first monolayer facing the gold surface [45]. Electron diffraction analysis and electron microscopy have been used to determine the structure of the gold nanorods prepared by seed-mediated surfactant-direct synthesis. The nano-rods have an idealized 3D prism morphology with five Au(111) surface at the two ends and five Au(100) or Au(110) side facets [46]. The shape of a nanorod shape implies that the ends of the rod grow at a faster rate than sides. Different mechanisms have been proposed to explain the growth of gold nanorods in solution. Among the first proposals is the formation of twinned structures where the growth of more strained facets inhibited causing elongation in the unstrained direction [47]. In particular, the seed crystals are initially transformed into decahedral pentatwinned crystals. This could explain the break-

ing of the initial spherical symmetry, but has been criticized as a mechanism for further growth in the direction of the rod. Murphy and co-workers [48] proposed that the CTAB headgroups preferentially adsorb on the side facets of pentahedrally twinned rods, therefore slowing down their further growth (Figure 1.4). In such a scenario, the growth of gold nanorods would thus be governed by preferential adsorption of CTAB to different crystal facets during the growth [48]. Considering the preferential adsorption of CTAB to the different facets in a bilayer fashion [45], [48], [49], a "zipping" mechanism was proposed taking into account the van der Waals interactions between surfactant tails within the surfactant bilayer, on the gold surface, that may promote the formation of longer nanorods from more stable bilayers (Figure 1.5).

Perez-Juste *et al*. proposed that surface potential decays more rapidly at the nanorod tip than along its length, and thus $AuCl_2^-$ loaded micelle can more readily approach the tips of the rods than the sides and allow deposition of gold (Figure 1.6) [16].

The growth kinetic of nanorods was also investigated using SAXS and optical spectroscopy by Henkel *et al*.. They found that the initial growth rate at the ends of nanorod is 5 times higher than that at the side but with time both rate decrease exponentially which leads to a switch from 1D to 3D growth [50].

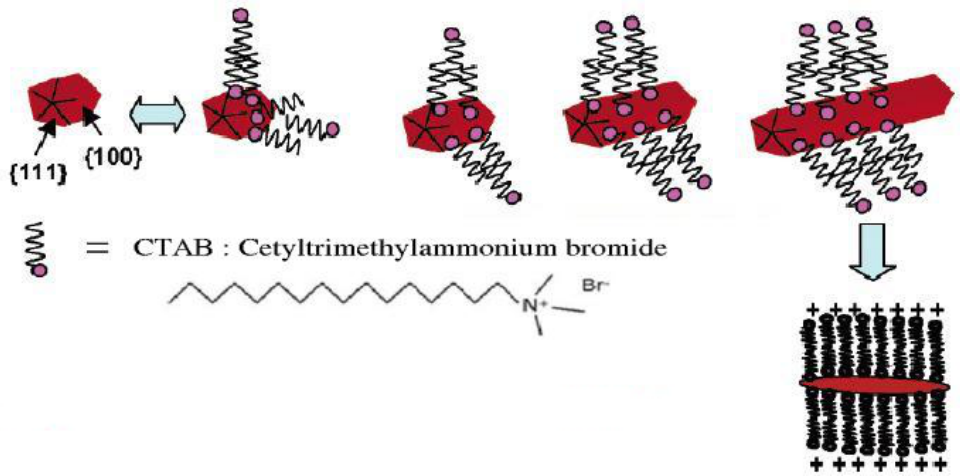

Figure 1.4: Schematic representation of mechanism of preferential adsorption of CTAB on gold nanorod. This figure has been adopted from the ref. [14].

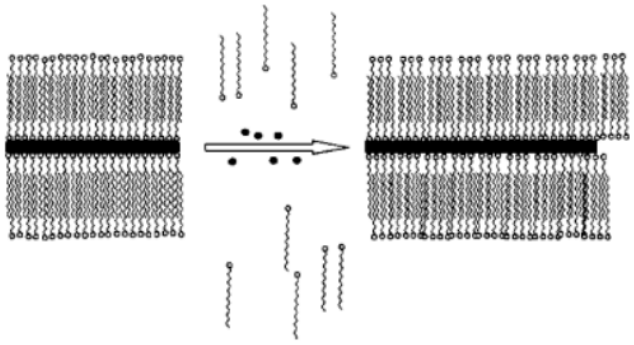

Figure 1.5: Schematic representation of "zipping" mechanism: the formation of the bilayer of CTAB (squiggles) on the nanorod (black rectangle) surface may assist nanorod formation as more gold ions (black dots) are introduced. This figure has been adopted from the ref. [49].

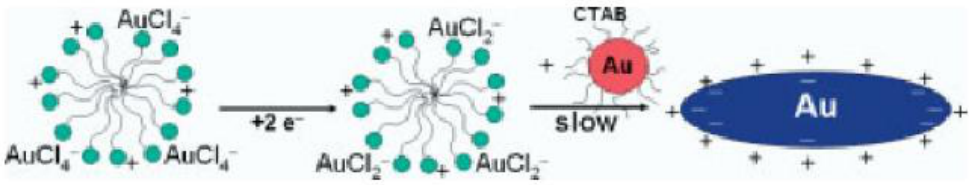

Figure 1.6: Schematic representation of growth of nanorod due to elongated interaction between CTAB micelle and tip of the nanorod. This figure has been adopted from the ref. [16].

1.4.2 *Growth in the presence of silver ions*

The presence of silver ions (silver nitrate) allows for a better control of the shape of gold nanorods synthesized by the electrochemical method. Murphy and co-workers proposed a variation of the initial procedure for long nanorods, in order to increase the yield of rod-shaped nanoparticles (up to 50%) and to control the aspect ratio of shorter nanorods and spheroids [12]. Under identical experimental conditions, a small amount of silver nitrate is added (5×10^{-6} M) prior to the growth step. The aspect ratio of the spheroids and nanorods can be controlled by varying the ratio of seed to metal salt. The mechanism by which Ag^{+} ions modify the metal nanopar-

ticle shape is not really understood. It has been hypothesized that Ag^+ adsorbs at the particle surface in the form of AgBr (Br^- coming from CTAB) and restricts the growth of the passivated crystal facets [12]. The possibility that the silver ions themselves are reduced under these experimental conditions (pH 2.8) can be neglected [51].

It has been observed that, after adding silver ions to the growing solution, the characteristic silver surface plasmon band at 400 nm could not be observed, but when pH of the solution was increased, silver nanoparticles formation was observed. This suggests that silver ions are not reduced to the elemental metal during the growth of the nanorods. It is observed that silver ions in an aqueous CTAB solution can be reduced to its elemental form by ascorbic acid only above pH = 8 [12]. However, in a typical synthesis of gold nanorods, the pH of the growing solution is about 3. Therefore, silver ions should not be reduced to form silver metal in the bulk. But, silver ions could still deposit on the gold surface *via* underpotential deposition (UPD). Liu and Guyot-Sionnest suggested that underpotential deposition of metallic silver occurs on the different crystal facets of gold, leading to symmetry-breaking and rod formation. The UPD shift of silver on gold surfaces decreases in the order Au(110) > Au(100) > Au(111). This is consistent with the UPD data suggesting that the higher the coordination number for the adatom, the higher the UPD shift, and the nobler is the deposition metal monolayer [22].

UPD can also explain the symmetry breaking required to initiate rod growth. For example, slower growth of Au(110) side facets and faster growth of Au(100) end facets lead to the breaking of the growth symmetry. However, this does not explain the crucial fact that single crystalline rods grow along the (100) direction, and yet the Au(100) facets on the edges of the rods do not grow. It may be possible that UPD on silver occurs on most of the facets, but lower coverage of silver on the tips than the side facets leads to anisotropic growth of gold nanoparticles. It has been hypothesized that silver monolayer has strong binding on Au(110), inhibiting further growth [22]. It is also possible that the gold nanorod tips are only partially covered

by silver, and, therefore, grow faster, that leads to one-dimensional growth along the tip of the nanorod.

The nanorods produced in the presence of silver ions are also single crystalline, where the longitudinal growth occurs in the (100) direction, the tip is bound by Au(111) and Au(110) facets, the side of the nanorod by eight higher index Au(250) facets [52]. Park *et al.* [53] suggested that the Au(250) facets are developed through adatom migration as the gold nanorod matures during synthesis, and that the nanorod is bound by alternating Au(100) and Au(110) facets at the early stage on the side. Nanorods with higher index facets are obtained in the presence of Ag^+ ions that consist of octagonal side facets Au(5120), the rod ends terminate in a pyramid with Au(130) facets, and each pyramid is connected to sides by four small Au(5120) "bridging" facets [54].

1.5 MOTIVATION AND OUTLINE OF THE THESIS

Up to date, a microscopic investigation/validation of the proposed growth mechanisms as described in the paragraphs above is still missing. From the theoretical point of view, to date, there have been a number of models to describe the growth of gold nanorods.

Classical theories, utilizing methods of continuum thermodynamics and kinetics, have been used to describe the evolution of discrete structures occupying the nano to microscales [55]. A surface area limited model for nanoparticle evolution *via* coarsening has been proposed [56], which is consistent with established classical theories [57], [58] but facilitates the modeling of faceted nanoparticles and anisotropic nanostructures using a limited set of input parameters. Empirical models have also been used, which allow the structure and shape optimization of nanoparticles using the efficient energetic approach for the metal-environment interaction, while mimicking interaction types ranging from covalent-like, through pair-wise, up to strongly coordination-dependent [59]. For example, the role of the environment in the stability of anisotropic gold nanoparticle has been studied using

the simulations which include metal-metal interactions via a many body expression derived from the second-moment approximation (SMA) to the tight binding model and the metal-environment interaction by an additional many body potential which modifies the energy of the outermost nanoparticle atoms in a way which depends on their coordination [60]. However, In such simulations, species of the environment are not explicitly included.

Atomistic molecular dynamics simulations can help to reveal the role played by capping agent, halide ions and silver ions in controlling the shape of a nanoparticle at a microscopic molecular level. This indeed the main aim of this thesis.

MD simulations have been quite successful in complementing experimental techniques in the study of surfactant solutions. For examples, MD simulation techniques are used to study the monolayer of CTAB formed at the air/water interface [61], the combination of MD results with a molecular thermodynamic model to predict some fundamental parameters of CTAB and other surfactants [62], studies of decyltrimethylammonium chloride micelles [63] and characterization of its hydration layer [64].

Moreover, MD simulations have been quite successful in complementing experimental techniques in the study of adsorption of organic molecules on the metal surfaces. For example, the self-organization of nonionic surfactant, n-alkyl poly(ethylene oxide) at a planar graphite-like surface in water has been studied by means of coarse-grain MD simulations. Surfactants with a short chain form a monolayer on the graphite surface with a thickness roughly equal to that of the alkane tail, on the other hand, longer-tail surfactants form continuous hemicylinders on the surface with diameter 5.0 nm [65].

MD simulations have also been used to investigate the mechanism of the growth and shape control of silver nanoparticles. The interaction energies between surfactant (i.e. CTAB) and Ag(100), Ag(110) and Ag(111) have been calculated [66]. MD simulations have been used to reveal a microscopic picture of the molecular mechanism of peptide binding on gold facets [67], [68]. Facets selectivity of ligands such as citrate, monocarboxylates, dicarboxy-

lates, and tricarboxylates on Ag(111) and Ag(100) has also been addressed [69].

The microscopic mechanism of formation of gold nanostructures in ionic liquids has been also addressed using quantum mechanical and MD simulations. Structure and energetics of the self-assembly of ionic liquids on metal surfaces from single ion pairs to multilayers, using the example of 1-ethyl-3-methylimidazolium ethyl sulfate ([EMIM][ES]) on the Au(111), Au(100) and Au(110) facets of gold. Adsorption is controlled by the interplay of soft epitaxy, ionic interactions, induced charges, and steric effects related to the geometry of the cation and anion [70].

MD simulations are an ideal tool to investigate microscopic growth mechanisms of gold nanorods, since the atomistic details of the metal surface, as well as of the surfactants, ions and of the solvent can be naturally included.

Here we aim to use MD simulations to investigate the following issues related to the growth mechanism of gold nanorod:

- Structure and dynamics of the surfactant layer at the gold/electrolyte interface: quantitative analysis of packing densities and their dependence on the different facets.
- Ions distribution and electrolyte potential drop across the gold/surfactant/water interface.
- Diffusion mechanism of gold reactant ($AuCl_2^-$) across the CTAB layer on gold surfaces.
- Role of the higher index facets; how does the surfactant layer compare to that on the lower index facets.
- Influence of tip and curvature/structure of nanorod on the packing of the surfactants molecules.
- Microscopic origin of the strong impact of halides ions on the anisotropy growth of gold nanoparticles.
- Effect of the addition of silver ions to the growing solution with particular emphasis on the silver ion distribution and binding to the CTAB

micelle or CTAB layer. How silver ions specifically interact with the different facets.

The structure of the thesis is the following: In chapter 2 an overview of the molecular dynamics simulations, methods and force field used in the simulation is provided.

In chapter 3, the structure of the surfactant layer on the gold surface in contact with electrolyte solution has been investigated. An innovative aspect is the inclusion of the role of the surfactants, which is explicitly modeled on the different surfaces. The atomistic simulations provide a microscopic understanding of how macroscopic quantities such as surfactant thickness, surfactant surface (packing) density and its structure influence the growth.

In chapter 4, the surfactant coverage on higher index facets has been investigated and compared with the surfactant coverage on the lower index facets. In particular, the adsorption of CTAB on different higher index facets of gold nanorods has been studied and compared with adsorption on lower index facets. Moreover realistic models of the cuboctahedral nanoseed, the penta-twinned nanoseed and nanorod have been built and simulated in the growing electrolyte solution including the CTAB surfactant. The adsorption of CTAB has been investigated in order to understand how tips and edges of the nanocrystal influence the adsorption of CTAB on nanorod as compared to that on flat surfaces.

In chapter 5, the role of halides in controlling the anisotropic growth of gold nanorods has been investigated through a combined computational and experimental approach. In particular, we discuss how the halide ions influence the surfactant layer and surfactant coverage on the different surfaces at different concentration of CTAB/CTAC, which can help to elucidate how different nanoparticles shape can be obtained in the experiments with different CTAB/CTAC concentration. The thickness of the CTAB and CTAC layers from the simulations has been compared with the analogous experimental quantity obtained from the measurements of the plasmon resonance shift.

Finally in chapter 6, silver ions have been introduced in the simulated growing solution in order to investigate how their adsorbed on different gold surfaces and how they affect the structure of the surfactant layer.

2

MOLECULAR DYNAMICS SIMULATIONS

2.1 INTRODUCTION

Molecular dynamic (MD) simulation is a useful tool to compute the macroscopic behavior of a system from the microscopic interactions. Predictions from MD simulations can be used to understand and interpret the experimental results and to reproduce conditions which are difficult to access in the laboratory. In particular, classical MD simulations consider atoms in the system as point particles and the motion of these particles can be described by classical mechanics, where quantum mechanical effects are only implicitly included in the potential energy. In an MD simulation, Newton's equations of motion for a molecular system are solved, obtaining trajectories for all the atoms in the system. From these atomic trajectories, a variety of macroscopic thermodynamic properties can be calculated which can be compared with experiments or can be used to explain the certain experiential results.

2.1.1 *Equations of motion*

In the N particle system, particles are described by their positions $\mathbf{R}_i$ and momenta $\mathbf{P}_i = m_i \mathbf{V}_i$. Where $\mathbf{V}$ are the particles velocities and m_i is the mass of the particle i. The Hamiltonian H of the system can be written as

$$H(\mathbf{P}^N, \mathbf{R}^N) = \sum_{i=1}^{N} \frac{\mathbf{P}_i^2}{2m_i} + U(\mathbf{R}^N), \tag{2.1}$$

here, $\mathbf{P}^N$ is the union of all momenta, $\{\mathbf{P}_1, \mathbf{P}_2, ..., \mathbf{P}_N\}$ and $\mathbf{R}^N$ is the union of all positions, $\{\mathbf{R}_1, \mathbf{R}_2, ..., \mathbf{R}_N\}$ and $U(\mathbf{R}^N)$ is the potential energy as a function of the positions [71]. Details on the form of the potential energy will be

provided later in this chapter. The forces acting on the particles are derived from the potential as

$$F_i(\mathbf{R}^N) = -\frac{\partial U(\mathbf{R}^N)}{\partial \mathbf{R}_i}. \tag{2.2}$$

The equations of motion are according to the Hamiltonian's equation

$$\dot{\mathbf{R}}_i = \frac{\partial H}{\partial \mathbf{P}_i} = \frac{\mathbf{P}_i}{m_i}, \tag{2.3}$$

$$\dot{\mathbf{P}}_i = -\frac{\partial H}{\partial \mathbf{R}_i} = -\frac{\partial U}{\partial \mathbf{R}_i} = F_i(\mathbf{R}^N). \tag{2.4}$$

2.1.2 *Integration of the equation of motion*

Different algorithms have been introduced to integrate the equations of motion in an MD simulation. I will describe here the verlet algorithm which has been employed in this work. This algorithm is time reversible, conserves the phase space volume and is efficient as the expensive force calculations are only performed once per time step in contrast to other algorithms [71], [72]. The algorithm can be derived using Taylor expansion of the coordinate $\mathbf{R}_i$ of a particle at time $t + \Delta t$

$$\mathbf{R}_i(t+\Delta t) = \mathbf{R}_i(t) + \mathbf{V}_i(t)\Delta t + \frac{F_i(t)}{2m_i}\Delta t^2 + \frac{\Delta t^3}{3!}\dddot{\mathbf{R}}_i + \mathcal{O}(\Delta t^4) \tag{2.5}$$

similarly,

$$\mathbf{R}_i(t-\Delta t) = \mathbf{R}_i(t) - \mathbf{V}_i(t)\Delta t + \frac{F_i(t)}{2m_i}\Delta t^2 - \frac{\Delta t^3}{3!}\dddot{\mathbf{R}}_i + \mathcal{O}(\Delta t^4) \tag{2.6}$$

by summing equation 2.5 and equation 2.6, equation 2.7 is obtained

$$\mathbf{R}_i(t+\Delta t) + \mathbf{R}_i(t-\Delta t) = 2\mathbf{R}_i(t) + \frac{F_i(t)}{m_i}\Delta t^2 + \mathcal{O}(\Delta t^4) \tag{2.7}$$

or equivalently

$$\mathbf{R}_i(t+\Delta t) = 2\mathbf{R}_i(t) - \mathbf{R}_i(t-\Delta t) + \frac{F_i(t)}{m_i}\Delta t^2 + \mathcal{O}(\Delta t^4) \tag{2.8}$$

The estimated error in the new position is of order Δt^4, where Δt is the time step for molecular dynamics simulation. The Verlet algorithm does not

use the velocity to compute the new position, however, the velocity of the particle can be obtained from the position of the particle at time t and $t+\Delta t$, using the following:

$$\mathbf{R}_i(t+\Delta t) - \mathbf{R}_i(t-\Delta t) = 2\mathbf{V}_i(t)\Delta t + \mathcal{O}(\Delta t^3) \tag{2.9}$$

or

$$\mathbf{V}_i(t) = \frac{\mathbf{R}_i(t+\Delta t) - \mathbf{R}_i(t-\Delta t)}{2\Delta t} + \mathcal{O}(\Delta t^2). \tag{2.10}$$

The estimated error in the velocity is of order Δt^2. At each time step, the temperature, potential energy and the total energy of the system are calculated. The total energy should be conserved throughout the MD simulation. After all calculations are completed, the old positions and velocities at time $t-\Delta t$ can be discarded. The new positions and the velocities become the next starting point. Such process is repeated a given number of times such that the desired time frame is reached.

2.2 ENSEMBLES

In a conventional molecular dynamic simulation, using the above equations (equation 2.4 and equation 2.3), a microcanonical (NVE) ensemble (constant number of particles N, volume V and energy E) is generated. However, MD simulations at constant temperature are desirable in order to simulate, e.g., the experimental conditions. Therefore, the temperature of a simulated system needs to be controlled. For this purpose, the velocity rescaling thermostat was used to generate canonical (NVT) ensemble. The average kinetic energy at a given target temperature, T is given by $\bar{K} = \frac{1}{2}N_f k_B T$, where N_f is the number of degrees of freedom, k_B is the Boltzmann constant. In order to get the desired temperature, all particle velocities are multiplied by the rescaling factor α,

$$\alpha = \sqrt{\frac{\bar{K}}{K}}, \tag{2.11}$$

where K is the average kinetic energy at the system temperature [71].

In the above approach, the average kinetic energy is fixed and the canonical equilibrium distribution of the kinetic energy is not sampled. Bussi et al. [73] have modified the way the rescaling factor is calculated in the above equation in order to enforce a canonical distribution for the kinetic energy. Instead of forcing the kinetic energy to be exactly equal to $\bar{K}$, its target value K_t have been selected with a stochastic procedure aimed at obtaining the desired ensemble. To this effect, the velocity-rescaling factor is evaluated as

$$\alpha = \sqrt{\frac{K_t}{K}}, \tag{2.12}$$

where K_t is drawn from the canonical equilibrium distribution for the kinetic energy:

$$\bar{p}(K_t)dK_t = K_t{}^{(\frac{N_f}{2}-1)}e^{-\beta K_t}dK_t. \tag{2.13}$$

The usual equations of motion are used to propagate the rescaling. In this manner, the correct sampling of the canonical NVT ensembles is possible.

Most of the experiments are usually performed at controlled temperature and pressure. Therefore pre-equilibration and final production run were performed with the isothermal-isobaric (NPT) ensemble. In this ensemble, the volume V, of the system fluctuates such that the average pressure of the system, $< P_{int} >$ is equal to an externally applied pressure P_{ext}. Therefore, in NPT ensemble, the volume is a dynamical variable. A thermostat is employed to ensure that both instantaneous temperature and pressure fluctuations are generated properly. The equations of motion for NPT ensemble proposed by Tuckerman and Martyna [74] for the positions and momenta are

$$\dot{\mathbf{R}}_i = \frac{\mathbf{P}_i}{m_i} + \frac{P_\epsilon}{W}\mathbf{R}_i, \tag{2.14}$$

$$\dot{\mathbf{P}}_i = F_i - (1+\frac{1}{N})\frac{P_\epsilon}{W}\mathbf{P}_i - \frac{P_\eta}{Q}\mathbf{P}_i, \tag{2.15}$$

$$\epsilon = \ln(\frac{V}{V(0)}), \tag{2.16}$$

where $V(0)$ is the volume at $t = 0$, W is the mass parameter associated to ϵ, and P_ϵ is the momentum conjugate to the logarithm of the volume, W is its associated mass parameter.

$$\dot{V}_i = \frac{dV_{P_\epsilon}}{W}, \tag{2.17}$$

$$\dot{P}_\epsilon = dV(P_{int} - P_{ext}) + \frac{1}{N}\sum_{i=1}^{N}\frac{\mathbf{P}_i^2}{2m_i} - \frac{P_\eta}{Q}P_\epsilon, \tag{2.18}$$

$$\dot{\eta} = \frac{P_\eta}{Q}, \tag{2.19}$$

$$\dot{P}_\eta = \sum_{i=1}^{N}\frac{\mathbf{P}_i^2}{2m_i} + \frac{P_\epsilon^2}{W} - (dN+1)kT, \tag{2.20}$$

In these equations P_{ext} is the external pressure, which is imposed. P_{int} is the internal pressure of the system given by

$$P_{int} = \frac{1}{dV}\left[\sum_{i=1}^{N}\frac{\mathbf{P}_i^2}{m_i} + \sum_{i=1}^{N}\mathbf{R}_i F_i - (dV)\frac{\partial U}{\partial V}\right]. \tag{2.21}$$

The variable P_ϵ acts as a "barostat" which drives the system to the steady state $< P_{int} >= P_{ext}$. The compressibility associated with equation 2.20 is

$$\kappa = -(dN+1)\frac{P_\eta}{Q} = -(dN+1)\dot{\eta}. \tag{2.22}$$

2.3 INTERACTION POTENTIALS

Performing molecular dynamics simulation of a system requires the numerical solution of equations of motion. For this purpose, an explicit expression for the total interaction potential $U(\mathbf{R}^N)$ is required. Typically the total interaction potential is described by the sum of the non-bonded interactions and the bonded interactions.

$$U_{total} = U_{non-bonded} + U_{bonded} \tag{2.23}$$

The non-bonded interactions are pair-additive and centrosymmetric. They include the electrostatic interactions and the Lennard-Jones potential. The non-bonded interactions between two atoms i and j, separated by a distance $r_{ij} = |r_i - r_j|$, can be described as

$$\begin{aligned} U_{non-bonded}(r_{ij}) &= U_{Coulomb}(r_{ij}) + U_{LJ}(r_{ij}), \\ &= \frac{q_i q_j}{4\pi\epsilon_0 r_{ij}} + \frac{C12_{ij}}{r_{ij}^{12}} - \frac{C6_{ij}}{r_{ij}^{6}}, \\ &= \frac{q_i q_j}{4\pi\epsilon_0 r_{ij}} + 4\epsilon_{ij}\left[\left(\frac{\sigma_{ij}}{r_{ij}}\right)^{12} - \left(\frac{\sigma_{ij}}{r_{ij}}\right)^{6}\right]. \end{aligned} \tag{2.24}$$

where q_i and q_j are the point charges on the atoms i and j, respectively. ϵ_0 is the permittivity of vacuum and ϵ_r is the relative dielectric constant. In all-atom MD simulations, a value of 1 is usually adopted for ϵ_r, since all atoms are explicitly included and so electrostatic screening should be accounted for directly. The parameters $C12_{ij}$ and $C6_{ij}$ for the atom pair i, j are obtained from $C12_{ii}$, $C12_{jj}$, and $C6_{ii}$, $C6_{jj}$ parameters, defined for each atom type, using the geometric combination rules [75]:

$$C12_{ij} = \sqrt{C12_{ii}C12_{jj}} \qquad C6_{ij} = \sqrt{C6_{ii}C6_{jj}}. \tag{2.25}$$

The bonded interactions describe the chemical binding within the molecule and include the contributions from all the bonds, angles, dihedrals and improper dihedrals terms. The bonded interactions are the sum of the bond (two-body), bond angle (three-body) and dihedral angle (four-body) potentials (equation 2.26).

$$\begin{aligned} U_{bonded} = \sum_{bonds} U_b(r_{ij}) + \sum_{angles} U_a(\theta_{ijk}) + \sum_{dihedrals} U_d(\phi_{ijkl}) \\ + \sum_{imp-dihedrals} U_{id}(\xi_{ijkl}) \end{aligned} \tag{2.26}$$

The bond interaction between atoms i and j is represented by a harmonic potential with the equilibrium bond length b_{ij} and force constant k_{ij}^b:

$$U_b(r_{ij}) = \frac{1}{2}k_{ij}^b\left(r_{ij} - b_{ij}\right)^2. \tag{2.27}$$

The bond angle vibration between a triplet of atoms i, j and k is also defined by a harmonic potential with the equilibrium bond angle θ^0_{ijk} and the force constant k^θ_{ijk}

$$U_a(\theta_{ijk}) = \frac{1}{2} k^\theta_{ijk} \left(\theta_{ijk} - \theta^0_{ijk}\right)^2. \tag{2.28}$$

The dihedral angle potentials describe the interaction arising from torsional forces in molecules using four atoms (i, j, k and l) that are connected by three consecutive bonds. The dihedral potential is given as

$$U_d(\phi_{ijkl}) = k^\phi_{ijkl} \left(1 + \cos\left(n_{ijkl}\phi - \delta\right)\right), \tag{2.29}$$

where the dihedral angle, ϕ is the angle between the normal vectors of the plane that consist atoms i, j, k and the plane j, k, l. The multiplicity n that is restricted to positive integers in order to maintain periodicity, k is the factor and δ is the phase shift.

Improper dihedrals are used to restrict the geometry of molecules to maintain a certain structure and to prevent molecules from flipping over to their mirror images. The dihedral potential is described as

$$U_{id}(\xi_{ijkl}) = \frac{1}{2} k^\xi_{ijkl} \left(\xi_{ijkl} - \xi^0_{ijkl}\right)^2. \tag{2.30}$$

2.4 CUT-OFF SCHEME AND TREATMENT OF LONG RANGE INTERACTIONS

The calculation of the pairwise interactions of a particle becomes very expensive when the large surrounding is considered around the particle. Therefore, the evaluation of pairwise interactions, $U(r_{ij})$ is normally limited to a local surrounding within the radius of cutoff distance. Lennard-Jones interactions are treated with a cutoff distance in the range 1.0 to 1.2 nm. To avoid numerical problems associated with a truncated (discontinuous) potential, the Lennard-Jones 12-6 potential is often modified by a switch/shift function that assures that the energy smoothly goes to zero when approaching the cutoff.

The Particle Mesh Ewald (PME) summation technique is the preferred method for evaluating electrostatic interactions in an MD simulation. It

splits the electrostatic interactions into two contributions, a short-range and a long-range part. While the former part is evaluated in real space, the latter one is solved in Fourier space and includes the interactions of the respective charge with all its period images.

2.5 PERIODIC BOUNDARY CONDITIONS

The use of periodic boundary conditions is usually necessary due to the limited system sizes of MD simulations. Periodic boundary conditions were employed to replicate the simulation box throughout space to form an infinite lattice. In the course of the simulation, as an atom moves in the original box, its periodic image in each of the neighboring boxes moves in exactly the same way. Thus, as an atom leaves the central box, one of its images will enter through the opposite face. There are no walls at the boundary of the central box, and no surface atoms. This box simply forms a convenient axis system for measuring the coordinates of the N atoms. The number density in the central box (and hence in the entire system) is conserved. It is not necessary to store the coordinates of the images in a simulation, only the coordinates of the atoms in the central box are saved. The periodic boundary conditions are combined with the minimum image convention such which means only one, the nearest image of each particle is considered for short-range non-bonded interaction terms. For long-range electrostatic interactions, lattice sum methods such as PME are employed [71].

2.6 FORCEFIELD PARAMETERS

There are several forcefields available for the interaction potentials parameters in the equations. These forcefield parameters must have a physically sound functional form and must reproduce the correct behaviour of the reference system. These forcefields should also be transferable to other systems and conditions. In this work, the biomolecular forcefield GROMOS96

53a6 [76] was employed. Which has been specifically developed for solutions containing biomolecules such as surfactant, peptides, proteins, sugars, nucleotides or lipids and have been used successfully to simulate biomolecular systems. The parameterization of the GROMOS force field is based primarily on reproducing the free enthalpies of hydration and apolar solvation for a range of biomolecules [76]. In this work, our systems typically include, a slab of gold surface/gold nanoparticles in contact with surfactants (CTAB and CTAC) and ions in water. Systems including halide ions and silver bromide in water on gold slab have also been simulated. In particular the cetyltrimethylammonium cation (CTA^+) model proposed and validated by Wang and Larson [77] has been used in combination with the SPC water model. The charge assignment for CTA^+ is such that the three methyl groups in the head group and the methylene group adjacent to the nitrogen carry a partial positive point charge of + 0.25e each and the central nitrogen atom is set to be neutral [77]. The Lennard-Jones parameters of gold and halide ions are reported in Table 5.3. The Lennard-Jones parameters for bromide ion are from Van-Gunsteren [78]. The Lennard-Jones parameters for gold from Heinz et al. [79] were used for the metal description.

The Lennard-Jones parameters for iodide ion are from Reif and Hunenberger [80]. They are compatible with ionic polarizability and are calibrated to reproduce single-ion hydration free energies derived from the experimental conventional hydration free energies along with a standard intrinsic hydration free energy of the proton.

2.6.1 *Deriving new parameters*

The forcefield, in particular parameters of $AuCl^{2-}$ (gold reactant) were derived using density functional theory (DFT) geometric optimization and Born Oppenheimer simulation (Bo-MD) were performed using the CP2K/QUICKSTEP package. The BLYP functional was used. The electron-ion interactions were described by GTH psedopotentials. SZV-MOLOPT-SR-GTH basis set is used for all atoms. A cutoff of 280 Ry is chosen for the charge

Table 2.1: Lennard-Jones parameters of Au, Ag^+, Cl^-, Br^- and I^-.

Name	C6 [kJ mol^{-1} nm^6]	C12 [10^{-5} kJ $mol^{-1}nm^{12}$]
Au [79]	0.029227046	0.9650000
Ag^+ [81]	0.00013	0.0005
Cl^- [76]	0.01380625	10.6915600
Br^- [78]	0.027655690	6.5480464
I^- [80]	0.044452000	18.8618000

density. Partial charges of 0.14e and -0.57e on the Au and Cl atoms respectively and Au-Cl equilibrium bond length of 0.237 were obtained using DFT geometric optimization. In particular, the charges were calculated using the density derived atomic point charges (DDAPC) approach [82], The bond stretching constant was set to 2392845 kJ mol^{-1} nm^{-2}. For the calculation of bond stretching force constant, velocity auto-correlation function (equation 2.31) was calculated using the trajectory from DFT-MD.

$$C(t) =< v(t).v(0) > \tag{2.31}$$

Fourier transform of the velocity auto-correlation was taken using equation 2.32 in order to calculate the frequency of vibration, ω.

$$F(\omega) = \int_{-\infty}^{+\infty} e^{(i\omega t)} C(t) dt \tag{2.32}$$

The bond stretching force constant k_{ij}^b, was calculated from the frequency of vibration, ω using the relation $k_{ij}^b = m\omega^2$

2.7 ANALYSIS

A fundamental problem in the field of MD simulation is how to efficiently explore the vast configuration space which is spanned by all possible molec-

ular conformations for the global low (free) energy regions which will be populated by a molecular system in thermal equilibrium. For this purpose, "ergodic hypothesis" is used in MD simulation, which states that all the accessible states in the phase space are equiprobable. Therefore, If a simulation is run for a sufficiently long time the system should eventually pass through all the possible states and should generate enough number of representative configurations such that time average of a quantity of interest is equal to the ensemble average. Therefore, average behavior of a many-particle system was studied using MD simulation by computing the natural time evolution of the system numerically and averaging the quantity of interest over a sufficiently long time.

3

STRUCTURE OF THE SURFACTANT LAYER ON THE GOLD SURFACES

3.1 INTRODUCTION

In this chapter, we aim to investigate the structure of the gold/electrolyte interface in the absence of silver ions. Therefore, we have developed microscopic models of the gold nanorod surfaces in contact with the electrolyte solution containing CTAB. We address the adsorption mechanism of CTAB surfactant on different facets of gold, namely Au(110), Au(100) and Au(111). In particular, we calculate properties like, number densities (ion densities) of species and electrostatic potential across the gold-CTAB and CTAB-water interfaces in order to differentiate the adsorption of CTAB on the different gold facets. We furthermore compare the thickness of the CTAB layer on the gold facets with the experimental results to gain predictive capabilities for a real system. Anticipating our results, we are able to differentiate the structural and electrostatic properties of the different facets. In particular, we find that CTAB has higher packing density (surface density) on the Au(110) and Au(100) surface forming there a more compact layer with respect to that on the Au(111) surfaces. We have also investigated the diffusion of a gold reactant, namely $AuCl_2^-$ towards the gold facets, identifying water-ion channels between the cylindrical micelles which are adsorbed on the gold facets.

3.2 COMPUTATIONAL METHODS

3.2.1 *Models and simulations details*

Our models for the gold nanorods surfaces consist of a gold slab in contact with a CTAB bilayer and electrolyte solution. The initial arrangement for the surfactants has been chosen according to the experimental suggestion that the CTAB is adsorbed on gold nanorods in the form of bilayer [45]. In Figure 3.1 we have reported the initial configuration for the Au(111) surface which consists of a cetyltrimethylammonium bromide cation (CTA^+) bilayer adsorbed on both side of the gold slab and bromide ions (yellow color) in water. The preassembled system consisting of CTA^+ surfactants on both side of gold surface was solvated with SPC water in a simulation box. The bromide ions (Br^-) were added to the system by randomly replacing water molecules. The packing density (surface density) for CTAB on the gold surfaces in the bilayer was initially chosen as 2.70 number/nm^2 which is slightly larger than the maximum packing density (2.44 number/nm^2) which has been calculated based on the cross section area of the head group of CTAB 0.32 nm^2 [83]. This slightly higher packing density was taken in order to allow the formation of a closely packed layer on the gold surface, as suggested by the experimental observation. Similar initial configurations were also prepared for the Au(110) and Au(100) surfaces. Further details of the simulation models for all three surfaces, including box sizes and number of atoms, are reported in Table 3.1. All MD simulations were performed using the GROMACS package (version 4.5.5) [84]–[87]. Periodic boundary conditions were applied in all three directions. Energy minimization was performed after the addition of water and ions to keep the maximum force on any atom below 1000 kJ $mol^{-1}nm^{-1}$. A constant temperature of 300 K and a constant pressure of 1 bar were maintained by the Berendsen and Parrinello-Rahman coupling scheme. A time step of 2 fs was employed and trajectories were stored every 2 ps. The systems were first equilibrated in the NVT ensemble (constant Number of particles, Volume, and Tempera-

ture) for 100 ps, subsequently NPT ensemble simulations were performed. MD production runs were performed for 200 ns for each surface model and trajectories from the last 50 ns are used for analysis. In addition to the three models for the different gold surfaces, we have also prepared a simulation setup where $AuCl_2^-$ was added to the gold/electrolyte interface in order to describe the ion diffusion at the interface. 2 $AuCl_2^-$ molecules were added to the interface model for all the three surfaces Au(111), Au(110), Au(100). 2 Na+ ions were also added to neutralize the system. Production runs of 500 ns were considered for each of the three different interfaces.

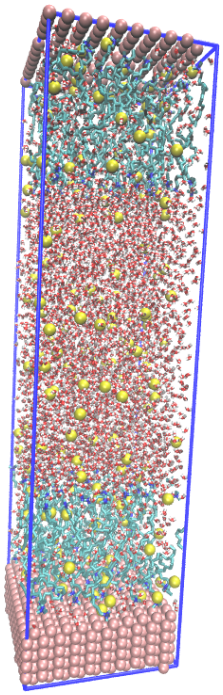

Figure 3.1: Snapshot of our simulation model at t=0, which consists of a CTAB bilayer on both side of the gold slab solvated in water. Br^- ions are shown in yellow. Here the model system for the Au(111) surface (see more details in Table 3.1) is shown. Similar models were also built for the other surface directions, namely Au(110) and Au(100).

3.2.2 *Forcefield parameters*

GROMOS96 53a6 forcefield [76] was employed for all our MD simulations. In particular the CTAB model proposed and validated by Wang and Larson

Table 3.1: Model details for the three interfaces on the Au(111), Au(110) and Au(100) surfaces.

Name of surface	No. of gold atoms	No. of CTAB molecules	No. of water molecules	Thickness of gold surface [nm]	Box dimensions X [nm], Y [nm] Z [nm]
Au(111)	1344	180	4982	1.26	4.07, 4.07, 15.47
Au(110)	1400	180	4936	1.45	4.08, 4.08, 15.90
Au(100)	1600	180	4884	1.43	4.1, 4.1, 15.61

[77] has been used in combination with the SPC water model. We have also validated the CTAB molel for CTAB micelle formation in water by comparing the micelle parameters with that obtained by Cata and co-workers [88] (see Figure A.1 in A). The charge assignment for CTA^+ is such that the three methyl groups in the head group and the methylene group adjacent to the nitrogen carry a partial positive point charge of + 0.25e each and the central nitrogen atom is set to be neutral (Figure 3.2) [77]. We also used the Lennard Jones parameters for gold as from Heinz *et al.* [79] which have been shown to provide a very good description of gold surface in contact with liquids and have demonstrated to be very accurate in reproducing adsorption energies[89], [90]. Partial charges on atoms of $AuCl_2^-$, equilibrium bond length and force constants were calculated using DFT calculations. Partial charges of 0.14e and -0.57e were assigned to the Au and Cl atoms, respectively. The Au-Cl bond length was set to the equilibrium value of 0.237 nm and the bond stretching constant to 2392845 kJ mol^{-1} nm^{-2}.

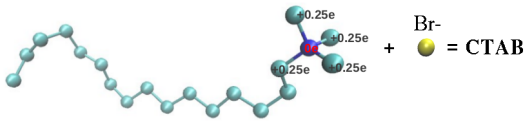

Figure 3.2: Model of the CTAB surfactant. Non zero point charges are reported on the corresponding atoms.

3.3 RESULTS AND DISCUSSION

3.3.1 *Adsorption of the single CTAB molecule on gold surfaces*

We have calculated the adsorption energy of a single CTAB molecule on different Au surfaces in a box containing 3215 water molecules (Table 3.2). The energies were calculated for all three surfaces using the method-1 described by H. Heinz [91]. At the time t=0, an initial configuration was chosen such as the CTAB head group is in contact with the surface and the tail sticks out in the water. However, an equilibrium configuration is quickly established where the CTAB adsorb flat on the surface. The adsorption energies for all three surfaces are quite similar. In particular the adsorption energy of CTAB on Au(111) surface is very close to the adsorption energy calculated by Feng *et al.* [89] (108.8 kJ/mole). There, the CHARMM-METAL force field was used, while here the GROMOS parameters from Ref.[77] were used.

Table 3.2: Adsorption energies of CTAB molecule.

Name of surface	Adsorption energy [kJ/mole]
Au(111)	-106 ± 13
Au(110)	-102 ± 17
Au(100)	-114 ± 21

3.3.2 *Structure of the CTAB layer on gold surfaces and ions distribution*

Our first goal here is to elucidate the CTAB layer structure at the gold/-electrolyte interface. Figure 3.3a shows a snapshot of simulation box containing the Au(111) surface, the CTAB layer and water layer after 200 ns, which shows the gold/CTAB and the CTAB/water interfaces. The CTAB head groups favorably attach to the gold surface and form a distorted cylindrical micelle structure on the gold surface. In the cylindrical micelle, the

CTAB head groups arrange in the outer layer of the micelle while the CTAB tails arrange in the core of the micelle. The Bromide ions (yellow colour) are preferentially found close to the CTAB nitrogen layer of the micelle. A similar conformation is also observed for the surfactant layer on the Au(110) surface (Figure 3.3b) and Au(100) surface (Figure 3.3c).

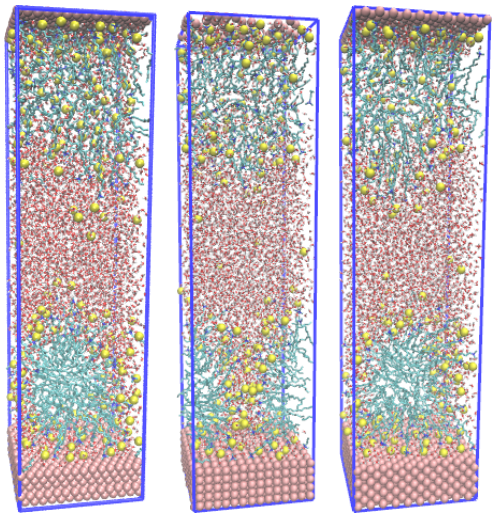

(a) (b) (c)

Figure 3.3: Snapshots from simulations of (a) Au(111), (b) Au(110) and (c) Au(100) surfaces with CTAB in water (see more details in Table 3.3 and Table 3.4).

In Figure 3.4 the number densities (ion densities) of CTA^+, water and bromide ion are reported as a function of distance from the Au(111) surface. The number densities of CTA^+ and Br^- show sharp peaks close to the gold surface which clearly indicates a strong adsorption of CTAB and Br^- ions on the gold surface (111). Also, a sharp peak in the water density near the surface implies that the head group of CTAB and Br^- ions are well solvated by the water near the surface. Similar trends of the densities of CTA^+, water and Br^- were observed for Au(110) and Au(100) surfaces.

Figure 3.5 presents a closer look at the number densities of N and Br^- as a function of distance from the gold (111) surface in the range [0:1.4 nm]. Number density peaks in this Figure show that the first Br^- layer is adsorbed on the gold surface as well as the first layer of the CTAB head groups which can be identified by the N peak. The distance between the

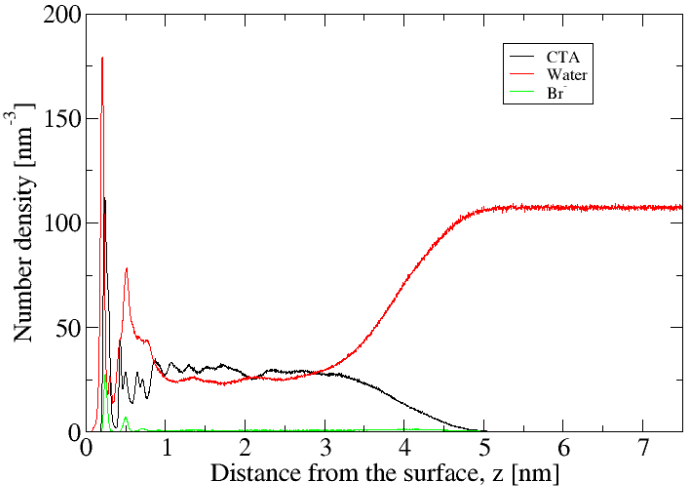

Figure 3.4: Number densities (ion densities) of CTA^+, water and bromide ions as a function of the distance from the Au(111) surface.

gold surface and Br^- layer is 0.24 nm whereas between N and Br^- layer is 0.05 nm. Some of the bromide ions are not strongly absorbed and they are distributed in the diffuse layer (for a pictorial view see Figure 3.3, where yellow dots represent bromide ions). In Table 3.5 the percentage of bromide ions in the diffuse layer is presented for different gold surfaces. Around 8% of bromide ions for Au(111) and around 3% of bromide ions for Au(110) and Au(100) are found in diffuse layer. The higher CTA^+ density on the Au(110) and Au(100) surfaces correlates with higher percentage of Br^- adsorption, leaving a lower Br^- ions density in the diffuse layer.

The thickness of the CTAB layer on the gold surface was calculated by measuring the distance from gold surface to the position of the maximum number density of nitrogen near the CTAB/water interface (see Figure A.2 in Appendix A). The average values for the CTAB layer thickness are 3.86, 3.74 and 3.85 nm for the Au(111), Au(110) and Au(100) surfaces, respectively. The three values are very close to each other and our conclusion is that there are no major differences between the surfactant layer thicknesses for the different surfaces. These values are within the experimentally estimated

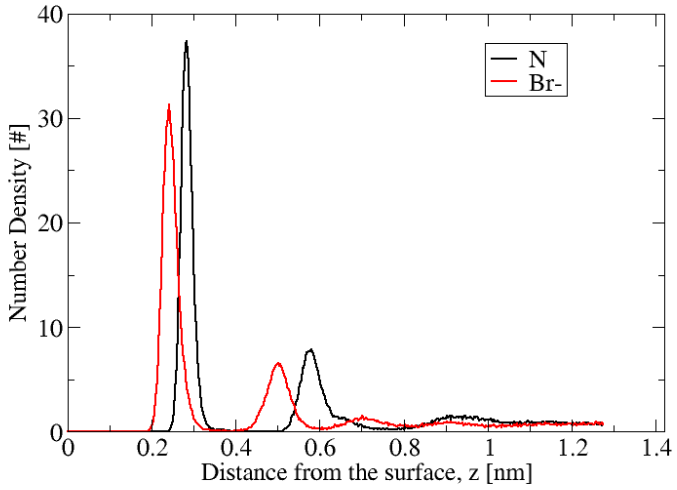

Figure 3.5: Number densities (ion densities) of nitrogen and bromide ions as a function of the distance from the Au(111) surface.

range 3.2-3.9 nm (Table 3.3) [92]–[95], although the current experimental data do not distinguish between the different surfaces.

Table 3.3: Thickness of the layer compared with experimental results.

Name of surface	Thickness from our simulation [nm]	Thickness from experiments [nm] [92]–[95]
Au(111)	3.86	3.2-3.9
Au(110)	3.74	3.2-3.9
Au(100)	3.85	3.2-3.9

We have also estimated the CTAB packing density on the different gold surfaces (Table 3.4). In particular the number of CTAB head groups in the first adsorbed layer is 21.72, 24.78 and 24.61 on Au(111), Au(110) and Au(100) respectively (see Figure A.3 in Appendix A). This would correspond to a packing area per CTAB of 0.76, 0.67 and 0.68 nm^2 on the Au(111), Au(110) and Au(100) respectively. We find that the packing density of CTAB is higher on the Au(110) and the Au(100) surfaces rather than on the Au(111) (Table 3.4). Our finding is then compatible with the proposal that the lower pack-

ing on the (111) facet would provide more accessible area to e.g. $AuCl_2^-$ favoring the growth of the gold nanorod along the (111) direction. The packing density from our simulations is slightly lower than the packing density in the experiments, which is based on the assumption that a perfect bilayer is formed on the gold surface.

We have shown how the CTAB surfactants arrange on the gold surface in the shape of distorted cylindrical micelles. This special arrangement allows the formation of water-ion channels between two contiguous micelles. A pictorial view of such arrangement can be seen in Figure 3.6a and 3.6b which presents a snapshot of the interface on the Au(111) surface. The surfactant layer is not a compact structure and a water-ion channel is formed between two cylindrical micelles providing possible space for the diffusion of $AuCl_2^-$ towards the gold surface which causes the growth of nanorods. Similar channels were also observed at the Au(110) and Au(100)/ electrolyte interfaces (see Figure A.4 in Appendix A). Figure 3.6c also shows that surface of the cylindrical micelle is not homogeneous in axial direction.

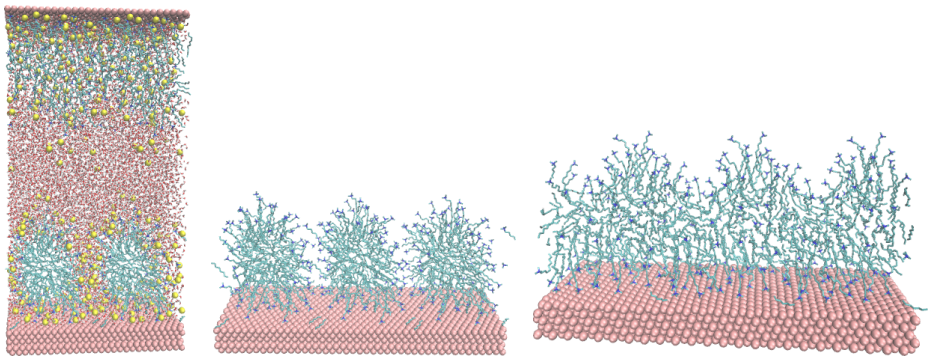

(a) (b) (c)

Figure 3.6: Snapshots from simulations of (a) Au(111) surfaces with CTAB in water, periodic in horizontal x- direction and shows water-ion channel, (b) adsorbed CTAB in the form of cylindrical micelle on Au(111) surface (cross section view of three micelles) (c) and adsorbed CTAB in the form of cylindrical micelle on Au(111) surface (axial view of a micelle).

The cross section area of water ion channel on all the surface was calculated (Table 3.4). The average width of the water ion channel was calculated

using nitrogen number density profile as shown in the Figure 3.7. The density of nitrogen has higher peak at the channel boundary. In the other direction, the length of the channel is the length of the box or length of the cylindrical micelle (Table 3.1). The cross section area of water ion channel which is available for the diffusion of $AuCl_2^-$ was found to be larger on Au(111) surface than on Au(110) and Au(100). Again this would point to larger accessible area for the (111) surface, and subsequently faster growth along the (111) direction.

Table 3.4: Packing densities (surface densities) of CTAB and cross section area of water-ion channel on the different gold surfaces.

Name of surface	Au(111)	Au(110)	Au(100)
Packing area per CTAB [nm^2]	0.76	0.67	0.68
Packing density of CTAB from our simulation [number/nm^2]	1.31	1.49	1.46
Packing density of CTAB from experiments [number/nm^2] [96]	1.68	1.68	1.68
Width of water-ion channel [nm]	0.94	0.71	0.73
Percentage area of water-ion channel on gold surface	23.10	17.40	17.80

Table 3.5: Percentage of bromide ions in diffuse layer for different gold surfaces.

Name of surface	Percentage of bromide ions
Au(111)	7.9
Au(110)	2.7
Au(100)	3.2

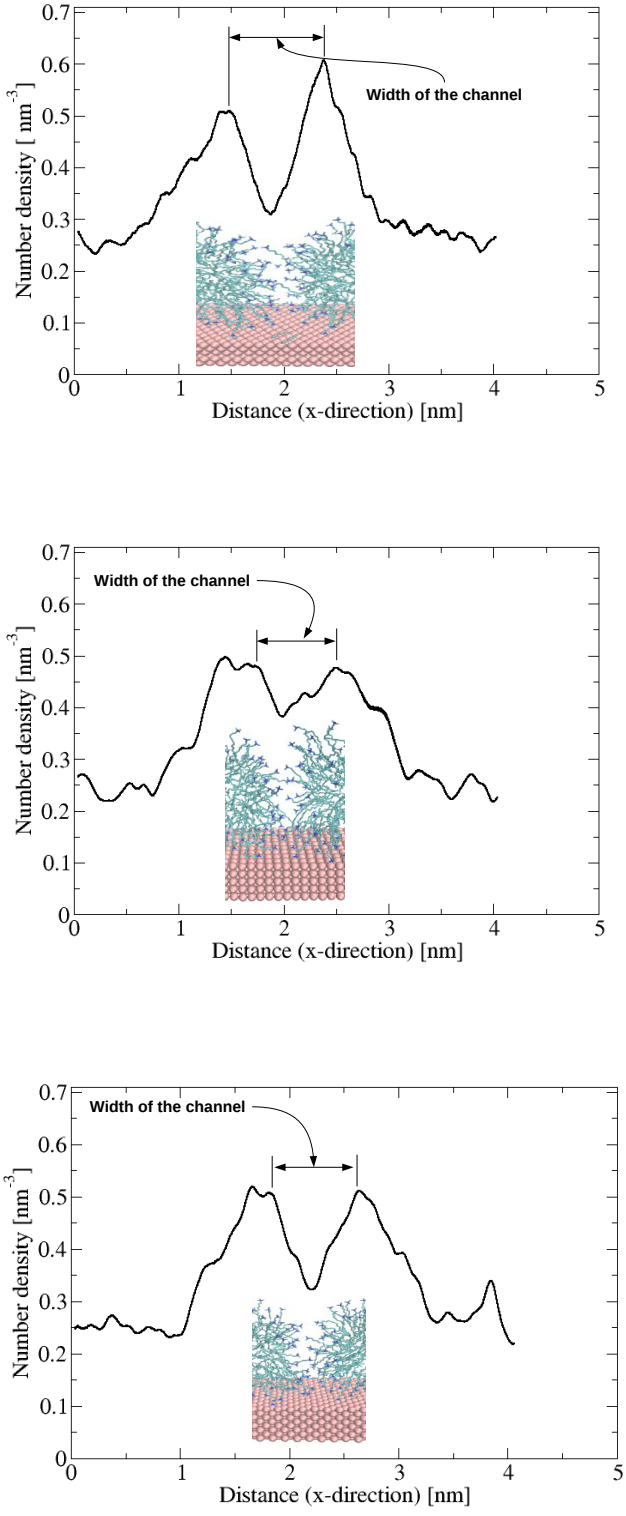

Figure 3.7: Number density of N for (a) Au(111), (b) Au(110) and (c) Au(100) surface as function of the distance in horizontal x- direction.

3.3.3 *Electrostatic potential across gold-CTAB-water interface*

The electrostatic potential across the interface is calculated by integrating the Poisson equation according to the following expression:

$$V(z) = -\frac{1}{\epsilon_o}\int_0^z dz' \int_0^{z'} \rho(z'')dz'', \tag{3.1}$$

where ρ is charge density [97]. Both the potential V(z) and the charge density $\rho(z)$ are functions of position along the z -axis, which is perpendicular to the gold surface and the surfactant layer. Eq.3.1 has already been averaged over x and y coordinates. The simulation box is divided in thin slices (0.003 nm thickness) along the z-axis and the charge density of each slice is determined as the sum of the partial charges of all atoms within the slice over the slice volume. The electrostatic potential is set to zero at the beginning of the box (z=0). In Figure 3.8, the electrostatic potential as a function of distance from the gold surface is reported for the different interfaces. The potential difference between the gold and the bulk electrolyte solution is calculated, and is found to be 0.80 V, 0.70 V and 0.68 V for the gold (111), (110) and (100) interfaces, respectively. The (111) interface exhibits the largest potential difference. The higher potential difference could be associated to easier diffusion of the negative $AuCl_2^-$ ions toward the gold surface. This finding would again point to the (111) direction as the most favorable for the growth in solution.

3.3.4 *Diffusion of gold ions from bulk solution to the gold surface*

We have shown that CTAB adsorbed in the form of distorted cylindrical micelles and a water-ion channel is formed between contiguous cylindrical micelles that can provide a possible path for the diffusion of $AuCl_2^-$ towards the gold surface which causes the growth of nanorods. In order to support this idea and to investigate the possible diffusion mechanism, we have performed additional MD simulations where two molecules of $AuCl_2^-$ have been added to the electrolyte solution. In particular we have prepared

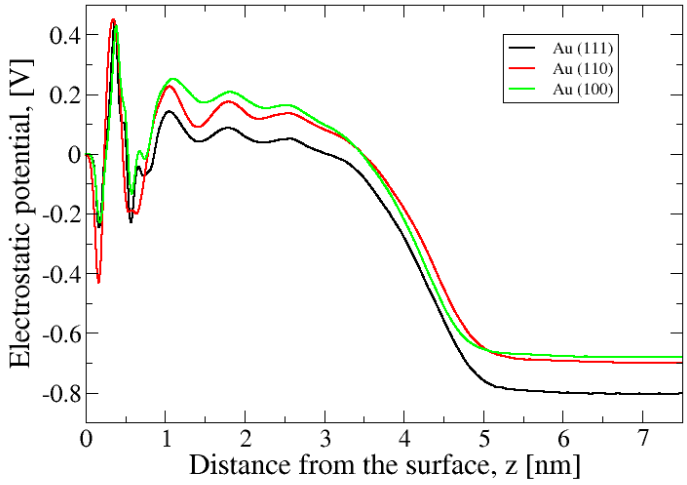

Figure 3.8: Electrostatic potentials as a function of the distance from the gold surfaces.

our initial configurations with the $AuCl_2^-$ above the CTAB layer at 5.4 nm from the gold surface (see Figure 3.9a). 2 Na+ ions were also added in order to neutralize the system. Our trajectories show that molecules of $AuCl_2^-$ can diffuse through the water-ion channel towards the gold surface (Figure 3.9b) and can get adsorbed on the gold surface (Figure 3.9c).

In Figure 3.10 we report the distance of $AuCl_2^-$ from the gold surface as a function of time. $AuCl_2^-$ can diffuse towards the surface over the explored timescale, at least for the Au(111) and Au(110) surfaces. In the case of the (111) interface one of the $AuCl_2^-$ molecule reaches the surface after 300 ns and remains on the surface (Figure 3.10a). A similar behaviour is also observed for the (110) interface (Figure 3.10b, black line). On the other hand at the (100) interface $AuCl_2^-$ approaches the surface up to a minimum distance of about 1 nm, but it doesn't get adsorbed on the surface within the 600 ns time frame (Figure 3.10c black and red lines). Our simulations show that the $AuCl_2^-$ molecule can diffuse through the water-ion channel between the micelles. However from the simple trajectories reported here it is not yet possible to directly quantify the diffusion rates. Moreover we have to stress here that within the current approach (classical force field-

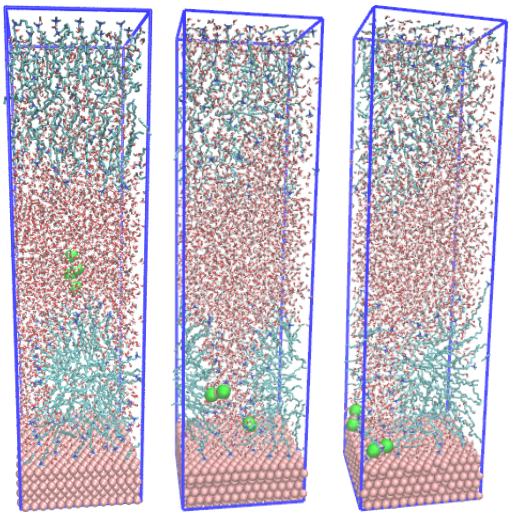

(a) (b) (c)

Figure 3.9: Snapshots from simulations of Au(111) surface with CTAB in water (a) molecules of $AuCl_2^-$ (green in colour) placed in the bulk water at time t = 0; (b) molecules of $AuCl_2^-$ diffuse through the water-ion channel towards the surface and (c) molecules of $AuCl_2^-$ adsorbed on the gold surface.

based simulations) it is not possible to describe the reduction of $AuCl_2^-$ on the gold surface and our analysis can only be limited to the diffusion of a "non-reactive" $AuCl_2^-$ specie. In the experiments $AuCl_2^-$ gets reduced to elemental gold after reaching the surface.

3.3.5 *Conclusions*

We have performed molecular dynamics simulations of different gold facets in contact with the electrolyte solution containing CTAB surfactants in order to understand the microscopic/molecular origin of the anisotropic growth. The different facets, namely Au(111), Au(110) and Au(100), forming the gold nanorods have been investigated. We observe that, on all the surfaces, the CTAB form distorted cylindrical micelles spaced by water channels containing bromide ions which provide a path for the diffusion of the gold reactants towards the gold surface. The observed structure is somehow in con-

trast with the common idea that CTAB on gold form a regular bilayer. The thickness of the (micellar) CTAB layer on gold is found in good agreement with the experiments. A higher packing density of CTAB characterizes the Au(110) and Au(100) surfaces with respect to the Au(111) surface, which could results into an higher growth of the nanorod in the (111) direction. Also, the electrostatic potential difference between the gold surface and the bulk solution was found to be higher for the Au(111) interface rather than for the Au(110) and Au(100) ones. Again this could point to a higher, easier diffusion of the reactant toward the Au(111) facets and could result into a preferential growth of gold nanorod in the (111) direction. From our analysis both proposed mechanisms supporting the anisotropic growth seems to be in place, pointing to the (111) facet as the less packed with surfactants and the one where a higher potential difference builds up between the surface and the electrolytic solution. The analysis of this chapter is limited to idealized planar (infinite) surfaces and further investigations are therefore required in order to address the role of the edges between different facets. This will be addressed in chapter 4.

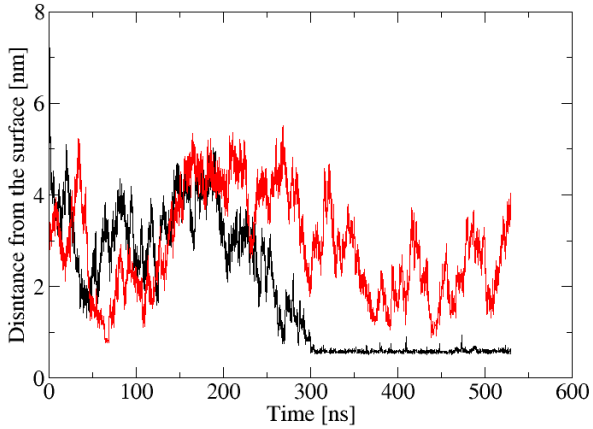

(a)

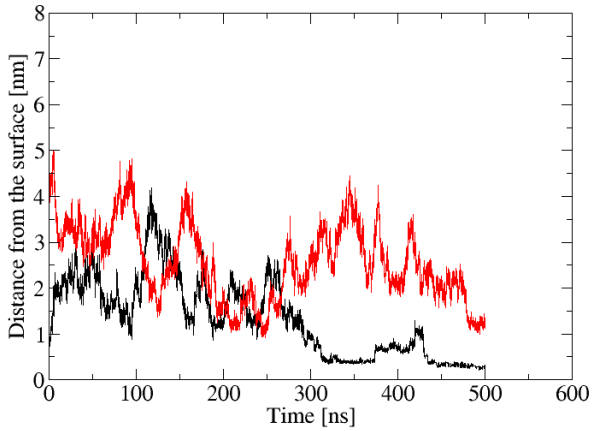

(b)

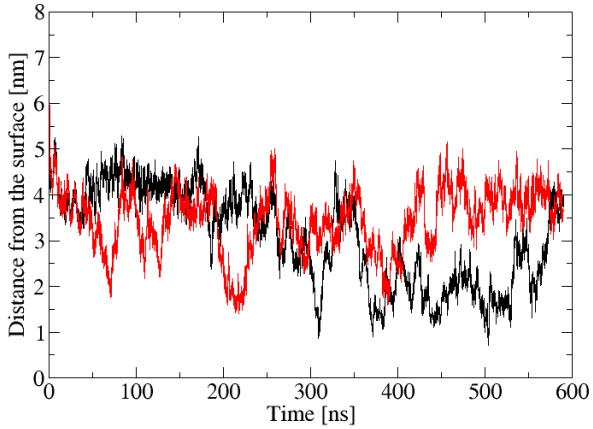

(c)

Figure 3.10: Distance of $AuCl_2^-$ molecules from the gold surfaces as a function of time for (a) Au(111), (b) Au(110) and (c) Au(100) surfaces

4

HIGHER INDEX FACETS AND NANOSEED MODELS

4.1 INTRODUCTION

In this chapter, we aim to investigate more realistic models for the gold nanoparticels. The main question we would like to address is how the conclusions from chapter 3 would be affected when instead of infinite low index planes, more complex 3D geometries for the nanocrystals are considered. Determination of crystal morphology of gold nanorods has been so far a major challenge due to their small size.

High resolution transmission electron microscopy (HRTEM) studies have shown that nanorods prepared in the absence of Ag^+ have an idealized 3D prism morphology (penta-twinned decahedral) with five Au(111) surface at the two ends and five Au(100) or Au(110) side facets [46]. The rods show a preferential growth along the common [100] axis. A schematic picture of such a geometry is reported in Figure 4.1a.

The addition of silver nitrate to the growing solution can increase the yield of short gold nanorods (aspect ratio circa 6) nearly of the 100% [14]. Indeed most of gold nanorods are currently prepared in the presence of silver. It has been recently shown that the cross section of nanorods prepared by silver-assisted seeded growth is bound by alternating Au(100) and Au(110) planes [52], [98] in agreement with the initial proposal [46], [99]. The assignment of the facets using the electron tomography and thickness profile measurements or high angle annular dark field scanning transmission electron microscopy (HAADF-STEM) measurements is however not so straightforward. Indeed the recorded images could also be interpreted assigning to the nanorod a geometry with eight identical high-index lateral Au(250) facets [52]. A schematic picture of such geometry is reported in

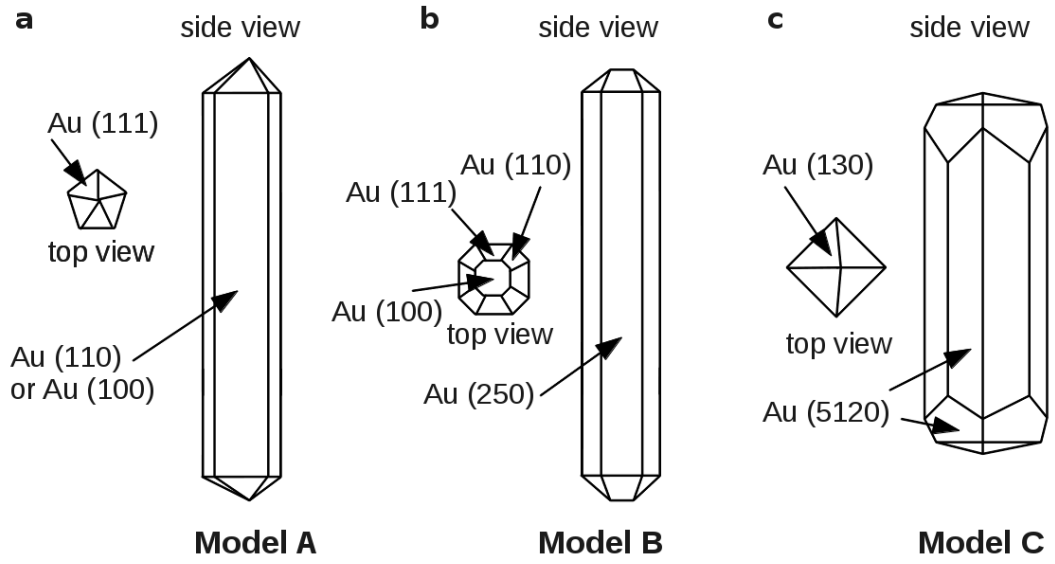

Figure 4.1: Schematic model for (a) penta-twinned bipyramid nanorod obtained in the absence of Ag^+. Au(110) or Au(100) facets characterize the lateral side [46]. (b) Truncated hexagonal bipyramid nanorod obtained in the presence of Ag^+ that has Au(250) facets on the lateral side [52], [98]. (c) This nanorod consists of octagonal side facets Au(5120), the rod ends terminate in a pyramid with Au(130) facets, and each pyramid is connected to sides by four small Au(5120) "bridging" facets [54].

Figure 4.1b. Again, for the silver-assisted growth, a different proposal was also formulated of nanorods which consist of octagonal side facets Au(5120), terminating at the two ends in a pyramid with Au(130) facets, and each pyramid is connected to sides by four small Au(5120) "bridging" facets [54]. A schematic picture of such a model is reported in Figure 4.1c. Atomic-level geometry of gold nanorod has been determined recently using quantitative scanning transmission electron microscopy and has been revealed the coexistence of high and low index facets with comparable stability and dimensions [100]. Au(110) and Au($1+\sqrt{2}$ 1 0) alternative facets were observed on the side of the nanorod and Au(111), Au(110) and Au(100) facets were observed on the rounded tip of the nanorod [100]. Higher index facets such as Au(1 -1 3), Au(-4 4 10), Au(-7 7 3), Au(-9 9 -1) and Au(0 0 -4) were also determined on unusual nanostructure such as trisoctahedra using streaked Bragg reflections in coherent electron diffraction patterns [101]. These recent

studies point to the fact that the interaction with surfactants and ions can lead to a reduction in the relative energy of a high index facet. This suggests that growth can occurs on relatively open facets beyond the standard view that the most probable facets are the most thermodynamically stable.

To understand the observed geometries for the gold nanorods, a key step is the microscopic understanding of the facet stabilization and the mechanism which induces the symmetry breaking from the initial isotropic seeds. In chapter 3, we have shown that the adsorption on Au facets with different indices can have different properties. In particular, concentrating on the low index facets which appear in the penta-twinned decahedral, we addressed the difference between the tip facet Au(111) and the lateral Au(100) and Au(110) facets. Our atomistic simulations, showed that on all surfaces CTAB forms distorted cylindrical micelles spaced by water/ions channels which can provide a path for the diffusion of the gold reactants toward the gold surface[102]. The observed structure is challenging the common idea that CTAB on gold forms a regular bilayer. Moreover we have shown that CTAB adsorbs on the Au(100) or Au(110) forming a more dense protective layer with respect to the Au(111) surface, thus explaining why the Au(100) or Au(110) facets could grow slower, eventually resulting into an anisotropic growth.

Our analysis was limited so far to three low index planes only, namely Au(111), Au(100) and Au(110). The first obvious question is: how would CTAB adsorption change on the higher index facets? In particular how would the presence of higher index challenge our explanation of the microscopic origin of the anisotropic growth just based on the difference between Au(111) and Au(100) or Au(110)? In order to answer this question, we have investigated the adsorption of CTAB on Au(250), Au(130) and Au(5120) surfaces in a growing electrolyte solution.

The second question would instead address the role played by the facet size. Namely our previous analysis assumed infinite surfaces, which is certainly appropriate to describe a growth stage of nanorods of size larger than the micellar size, namely beyond 4-5 nm (linear dimension). How would

such a picture change, or may be not, when we would instead consider small size particles whose facets can be of same size as the micelle, or even smaller? This question is certainly crucial to understand the initial growth stage, where starting from a spherical seed, the symmetry is eventually broken leading to more elongated geometries.

Recently a detailed atomistic scale observation of the initial, embryonic stages of gold nanorod growth has permitted to evidentiate that the seed particles initially grow isotropically until reaching a critical particle diameter of 4-6 nm in the Ag^+ assisted growth solution [103]. This is exactly the size we aim to investigate to see what is the effect of the edges on the facet dependent CTAB adsorption and to address the atomistic origin of the symmetry breaking.

4.2 METHODS

4.2.1 *Models and simulations details*

In Table 4.1, details of the model systems for the gold/electrolyte interface containing different types of higher index surfaces are described. In particular box sizes and number of atoms for the three surfaces Au(250), Au(130) and Au(5120) are reported.

In Table 4.2, details of the model of the nanoseeds and the nanorod in water containing CTAB are reported.

All MD simulations have been performed using the GROMACS package (version 5.0.5) [84]–[87]. Periodic boundary conditions were applied in all three directions. Energy minimization was performed after the addition of water and ions to keep the maximum force on any atom below 1000 kJ $mol^{-1}nm^{-1}$. A constant temperature of 300 K and a constant pressure of 1 bar were maintained by the Berendsen and Parrinello-Rahman coupling scheme. A time step of 2 fs was employed and trajectories were stored every 2 ps. The system was first equilibrated in the NVT ensemble for 100 ps, subsequently NPT ensemble simulations were performed. MD production

runs were performed for at least 400 ns for each interface model listed in Table 4.1. Trajectories from the last 50 ns were used for analysis.

In the case of the nanoseeds and the nanorod systems (models in Table 4.2), MD production runs of few µs were performed in order to achieve equilibrium configurations. The forcefield parameters used for the calculation of this chapter are the same as those used in chapter 3.

Table 4.1: Model details for Au(250), Au(130) and Au(5120) surfaces in contact with the electrolyte solution containing CTAB and water.

Name of surface	No. of CTAB molecules	No. of water molecules	Thickness of gold surface [nm]	Box dimensions X [nm], Y [nm] Z [nm]
Au(250)	180	4936	1.59	4.02, 4.09, 16.44
Au(130)	180	4936	1.30	4.05, 3.96, 16.12
Au(5120)	180	4936	1.43	4.05, 4.05, 16.28

Table 4.2: Model details for the nanoseeds and the nanorod in the electrolyte solution containing CTAB and water.

Name of structure	No. of CTAB molecules	No. of water molecules	Tip to tip length [nm]	Box dimensions X [nm], Y [nm] Z [nm]
Nanoseed (cuboctahedral)	1600	51911	-	13.62, 13.62, 13.62
Nanoseed (penta-twinned)	1600	43411	5.54	13.13, 13.13, 13.13
Nanorod	2400	119398	9.60	16.24, 16.24, 19.29

4.3 RESULTS AND DISCUSSION

4.3.1 *CTAB adsorption on higher index facets*

In Figure 4.2 we compare the adsorbed CTAB layer on different facets. In all the cases a snapshot after 400 ns of molecular dynamics simulation is

reported. On the higher index facets the adsorbed micelle has a structure which is similar to that on the lower index facets, although the overall surfactant layer appears to be more flat and compact as compared to the lower index facets. To discuss the possible differences between facets, the ion density profile as well as the integral number of CTA^+ and Br^- are calculated as function of the distance from the gold surface (Figure 4.2e-h).

If we look at the Br^- density (solid orange line) we can see that Br^- ions can adsorb in the gap available on the more open surfaces resulting a broader peak (Figure 4.2f-h), which is closer to the higher index facets than to the Au(111) (Figure 4.2e). The CTA^+ density (solid blue line) follows the Br^- density profile, also resulting in broad peaks for the higher index facets. In order to have a quantitative information on the Br^- surface passivation, we have calculated the number of adsorbed Br^- and CTA^+ per unit area, which we define as the surface density. The ion densities for all the investigated interfaces are summarized in Figure 4.3.

The surface density (packing density) was calculated as the number of ions present on the surface per unit area up to a 0.55 nm distance from the surface for CTA^+ (dotted line in Figure 4.3a) and up to a 0.43 nm distance from the surface for Br^- (dotted line in Figure 4.3b). This is the same criteria as used in chapter 3 [102]. Such a cut-off distance was chosen on the base of the density profile for the Au(111) interface in order to include only the first adsorbed layer. In the case of Au(111), the first and second layer (of CTA^+ and Br^-) are well separated from each other and there is no accumulation of ions between these layers. On the higher index surfaces, the separation between first and second layer is not so sharp and ions accumulate also in the region between the two maxima. The broader ion distribution is the result of the rougher surface, which is characterized by terraces and steps.

Table 4.3 shows the surface density of CTA^+ and Br^- (based on the cut-off 0.55 nm for CTA^+ and 0.43 nm for Br^-) and the width of the water-ion channels on the lower and higher index facets. The surface density of Br^- is higher on higher index facets than on the lower index facets, which suggests an higher passivation by Br^- ions on the higher index facets. The surface

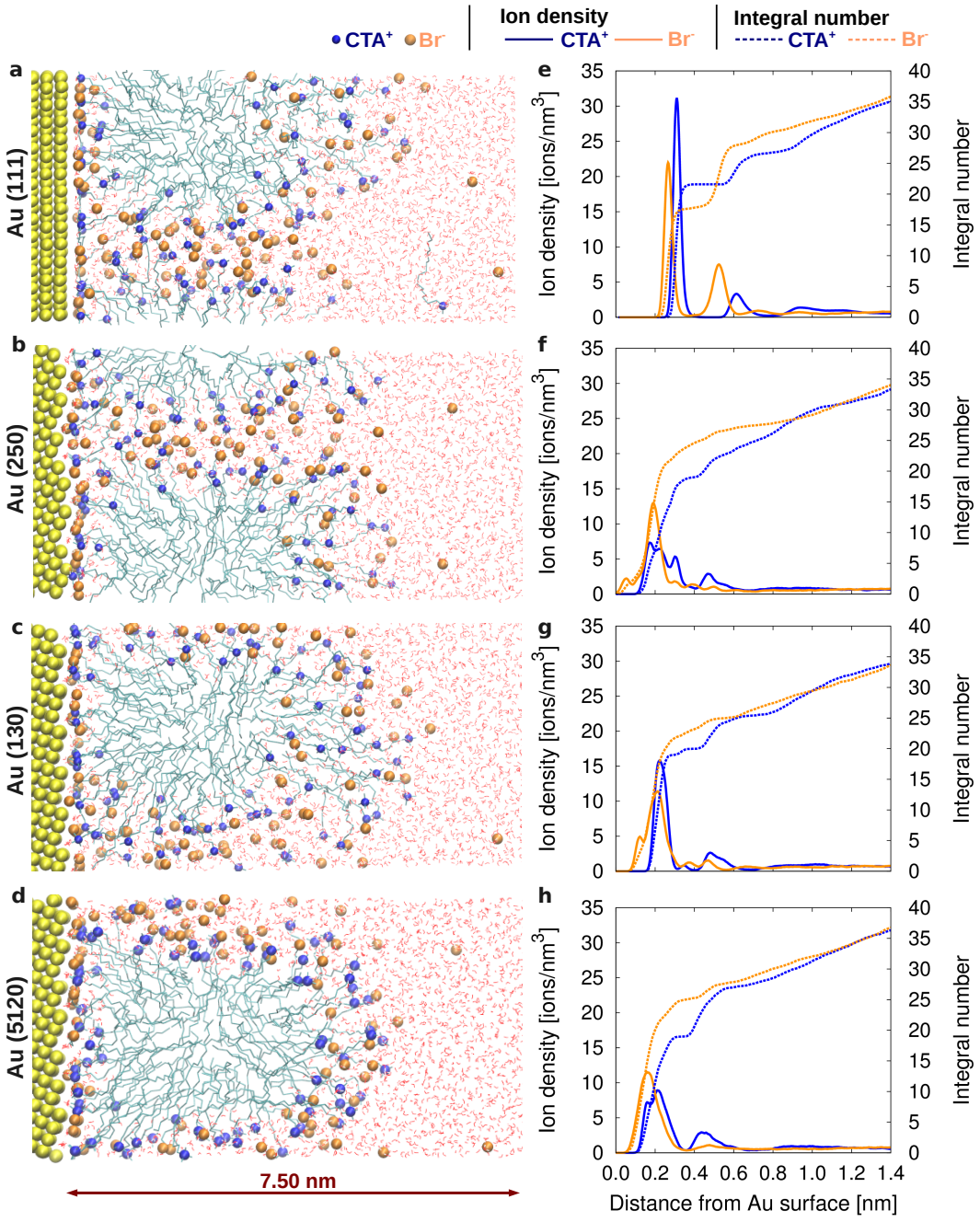

Figure 4.2: Snapshots from the simulation for (a) Au(111), (b) Au(250), (c) Au(130) and (d) Au(5120). Ion densities and integral numbers as a function of the distance from the Au surface for (e) Au(111), (f) Au(250), (g) Au(130) and (h) Au(5120) are reported.

density of CTA^+ is also higher on higher index facets except for Au(250). The denser coverage of ions on the higher index surfaces could, in turn, be responsible for a lower diffusion flux towards such surfaces.

Table 4.3: Surface densities (packing densities) of CTA^+ and Br^-, width of the water-ion channel and potential difference between bulk water and the CTAB layer on different gold surfaces.

Name of surface	Au(111)	Au(110)	Au(100)	Au(250)	Au(130)	Au(5120)
surface density of CTA^+ (ions/nm^2)	1.31	1.49	1.49	1.38	1.50	1.62
surface density of Br^- (ions/nm^2)	1.09	1.41	1.40	1.53	1.46	1.55
width of water-ion channel (nm)	0.94	0.71	0.73	0.56	0.65	0.60
potential difference ΔV [V]	0.86	0.83	0.82	0.83	0.81	0.80

We find that for Au(110), Au(100), Au(250), Au(130) and Au(5120), the Br^- density is around 1.4 -1.5 ions/nm^2, which is higher than the 1.1 ions/nm^2 obtained for Au(111). This would suggest that in all the considered rod models (a,b,c) in Figure 4.1 the lateral facets would be more protected by the surfactants than the tips allowing for the anisotropic growth. The CTA^+ surface density shows a similar trend with density between 1.4-1.6 ions/nm^2 for Au(110), Au(100), Au(250), Au(130) and Au(5120) and a lower density of 1.3 ions/nm^2 for Au(111).

Finally, the average width of the water-ion channels between the micelles can also be compared for the different facets. Such channels are narrower on the higher index facets than on the lower index facets (Figure 4.4, Table 4.3). This would eventually permits faster diffusion to the Au(111) surface than to the higher index facets.

As already done in chapter 3 for the low index planes, we have compared the electrostatic potential which arises at the interface between the electrolyte solution and the surfactant layer. The potential difference between the bulk solution and the CTAB layer is lower accross the higher index interface than across the Au(111) interface (Table 4.3, Figure 4.5). This would also point to a stronger driving force for the negative $AuCl_2^-$ diffusing towards the gold surface, resulting in turn into a faster diffusion towards Au(111) surface and, therefore, higher growth along Au(111) surface.

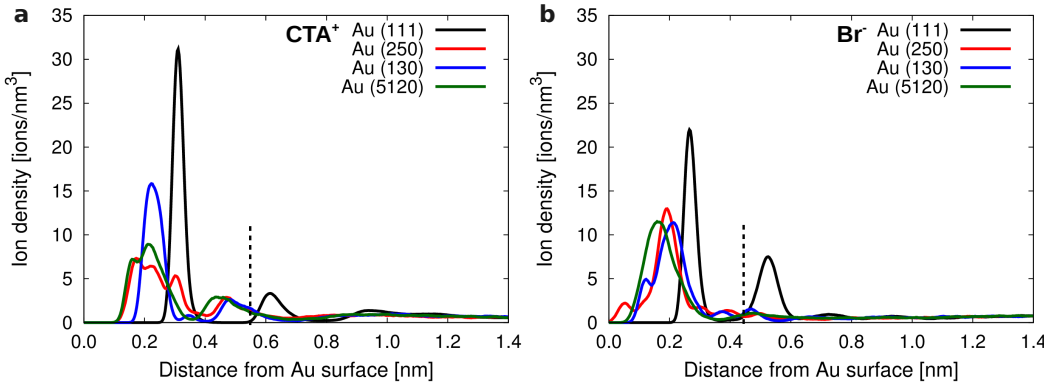

Figure 4.3: Number densities of (a) CTA^+ and (b) Br^- for Au(111), Au(250), Au(130) and Au(5120) interfaces.

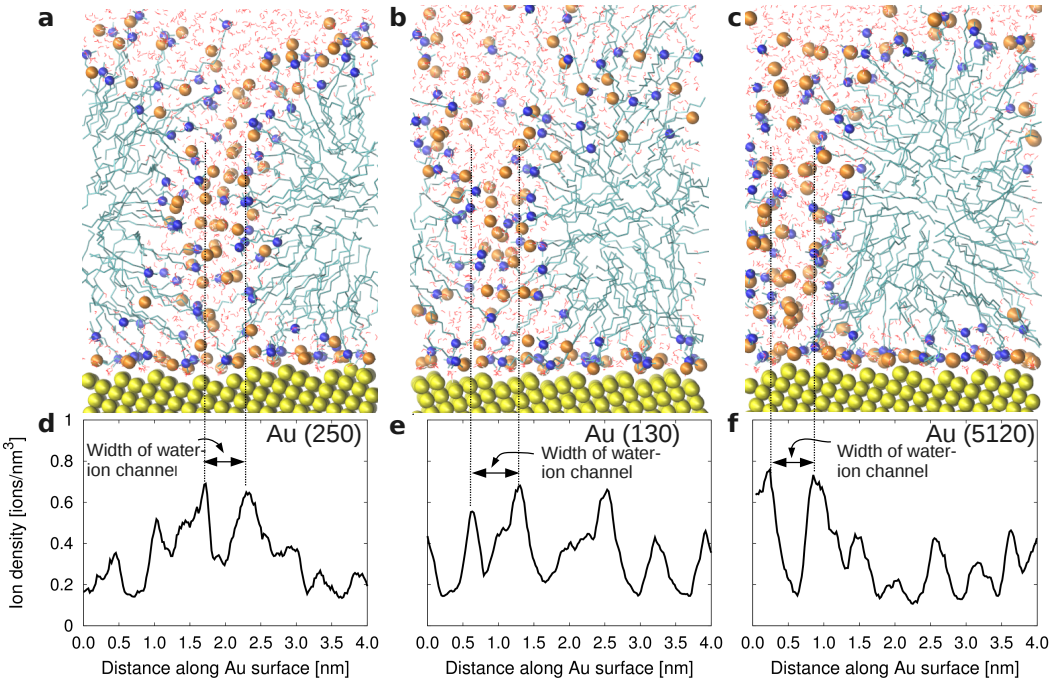

Figure 4.4: Water-ion channels between two adjacent micelles on Au(250), Au(130) and Au(5120).

4.3.2 *CTAB adsorption on nanoseeds and nanorod*

So far we have only examined infinite planes. The next question which we would like to address is how the picture that we have provided on the selective adsorption of the micellar layer is modified when instead a nanoparticle, whose size is comparable to that of a single micelle, is considered. For this purpose, we have built three different models of gold nanocrys-

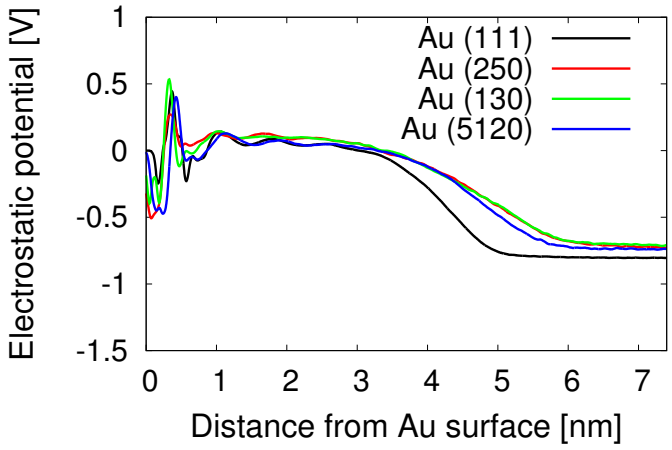

Figure 4.5: Electrostatic potentials as a function of distance from the gold surface for Au(111), Au(250), Au(130) and Au(5120).

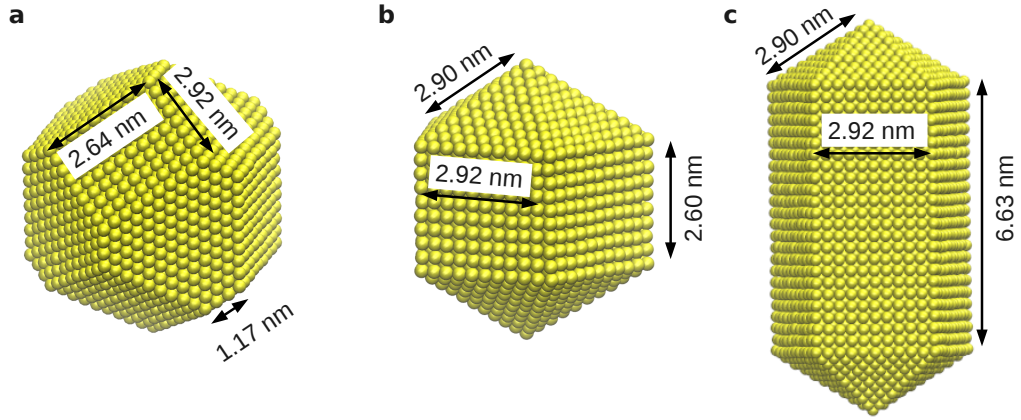

Figure 4.6: Snapshots of (a) cuboctahedral nanoseed (b) penta-twinned nanoseed and (c) penta-twinned nanorod.

tals (Table 4.2). As first model, we have chosen a cuboctahedral geometry bounded by Au(111) and Au(100) facets, which is the initial geometry of the seed nanoparticle before any truncation [103] (Figure 4.6a). As a second model, have considered a penta-twinned decahedral geometry (Figure 4.6b) where the lateral facets are Au(100) facets, while the tips are formed by 5 twinned Au(111) facets. Finally, as a third model, a penta-twinned decahedral nanorod of aspect ratio 2:1 is considered (Figure 4.6c).

We started our simulations considering a uniform CTAB density on all the facets, which exceeds the critical micellar concentration. We then let the system equilibrate for a rather extended time in the order of a few μs. We have

Table 4.4: Surface densities (packing densities) of CTA^+ and Br^- on the lateral facets of the cuboctahedral nanoseed, penta-twinned nanoseed and nanorod. The maximum standard error in the surface densities is 0.05 ions/nm^2.

Name of structure	CTA^+ (ions/nm^2)	Br^- (ions/nm^2)
cuboctahedral nanoseed, Au(100)	1.49	1.53
cuboctahedral nanoseed, Au(111)	0.18	0.19
penta-twinned nanoseed, Au(100)	1.62	1.62
penta-twinned nanoseed, Au(111)	0.19	0.30
penta-twinned nanorod, Au(100)	1.53	1.48
penta-twinned nanorod, Au(111)	0.30	0.16

quantified the Br^- and CTA^+ surface densities on the different facets of the nanocrystals as function of the simulation time (Details on the calculation of surface densities are reported in Appendix B).

In Figure 4.7, Figure 4.8b and Figure 4.9b, the surface densities are reported as function of time, which show that after an initial phase the numbers are converged suggesting no major rearrangement of the surfactant layer. We found that there is almost no micelle adsorption on the Au(111) facets of the cuboctahedral seed, while micelle adsorption was observed on the Au(100) facets with a structure similar to that observed on the infinite plane surfaces. A snapshot of the cuboctahedral seed in the CTAB solution is shown in Figure 4.7a. The surface density of the CTA^+ and Br^- are 1.47 ions/nm^2 and 1.55 ions/nm^2 respectively on the Au(100) facets of the cuboctahedron (4.4, Figure 4.7), which is very close to the packing density on infinite planes (4.3, while very low surface densities of CTA^+ and Br^- characterized on Au(111) facets of cuboctahedron.

A snapshot of both the shorter and longer nanocrystal immersed in the electrolyte solution is reported in Figure 4.8a and Figure 4.9a, respectively. While on the lateral Au(100) facets of the penta-twinned nanocrystals, the

micelles clearly adsorb with a structure similar to that observed on the infinite planes, the situation on the tip is dramatically different. Indeed, no clear micellar adoption is found on the inter-twinned Au(111) surfaces.

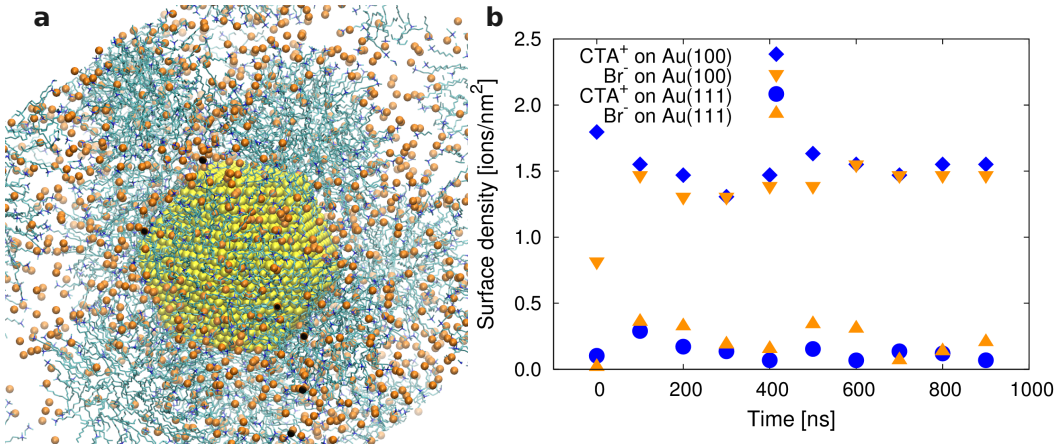

Figure 4.7: (a) Snapshot of the cuboctahedral nanoseed in CTAB solution after 900 ns (water molecules are not shown for the clarity). (b) Surface densities on the Au(111) and Au(100) facets of the cuboctahedral nanoseed as a function of time.

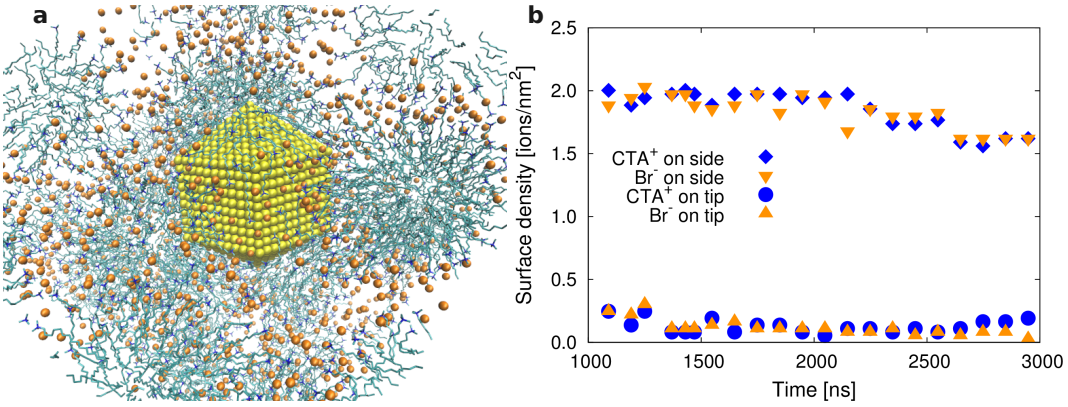

Figure 4.8: (a) Snapshot of the penta-twinned nanoseed in CTAB solution after 2950 ns (water molecules are not shown for the clarity). (b) Surface densities on lateral sides and on the tips of the nanoseed as a function of time.

4.4 CONCLUSION

Our results show that the higher surface densities of CTA^+ and Br^-, narrower water-ion channels and lower potential differences between the bulk water

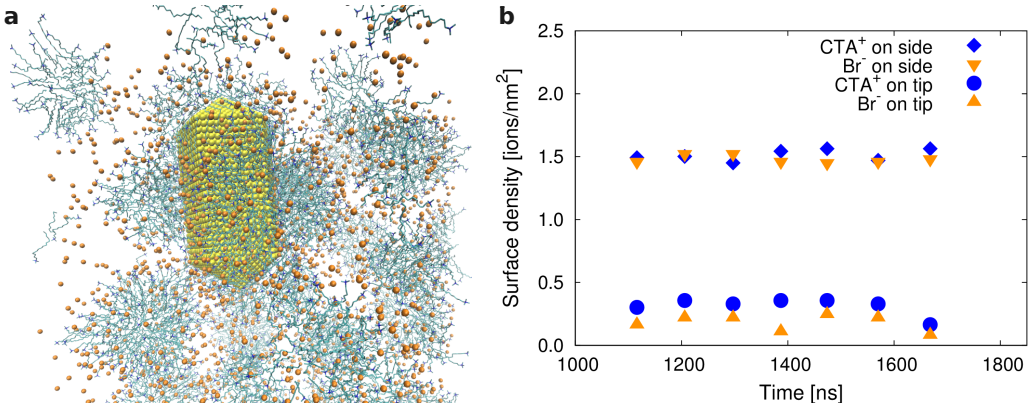

Figure 4.9: (a) Snapshot of the nanorod in CTAB solution after 1668 ns. (b) Surface densities on lateral sides and on the tips of the nanorod as a function of time.

and CTAB layer characterize the higher index facets as compared to Au(111), eventually resulting into a faster growth of the nanorod tips. In the initial stage of the growth where the seed has cuboctahedral geometry, the surface density of CTA^+ and Br^- is lower on Au(111) facets than on the Au(100) facets. Our results suggest that, in an early growth stage, when the seed is only a few nm large a dramatic symmetry breaking can occur, in which the CTAB protection of the Au(100) over the Au(111) facets of the cuboctahedral seed would promote an anisotropic growth of the nanocrystal. In the case of penta-twinned nanocrystals, the micelles adsorb on the lateral Au(100) facets with a structure similar to that observed on the infinite plane, however, no micellar adsorption is found on the tips. Such anisotropic surfactant layer would in turns promote an anisotropic growth where the less protected tips would grow faster.

5

ROLE OF HALIDE IONS IN THE GROWTH OF GOLD NANOPARTICLES

5.1 INTRODUCTION

In most of the synthesis recipes for gold nanoparticles, halide ions (chloride, bromide, or iodide) are present in water in addition to the stabilizing surfactants or polymers [16], [18]–[31]. In fact, halide anions significantly influence the morphology of gold nanoparticles [32], [33], thanks to their strong tendency to adsorb on metallic surfaces.

In particular while Br^- is able to promote anisotropic growth in seed mediated synthesis, Cl^- is known to induce a faster isotropic growth. The growth of the nanoparticles takes place in a rather complex mixture of salts and surfactant in water [104], and a microscopic, atomistic understanding of the growing solution would help to understand the mechanism and to rationally control the synthesis. Some recent theoretical studies have tried to rationalize the role of halides. In particular, DFT - based calculations have been used to show that surfactant, bromide, and silver preferentially adsorb on some facets of the seeds [105]. This is certainly an interesting first step in the direction of microscopically understanding the role of interfacial interactions in shaping the growth, however the cost of DFT calculations is still preventing us from going beyond system sizes which only includes a few molecules. To consider larger systems at the nanometric scale, also including the electrolytic solution and therefore accounting for temperature effects as well as the role of dynamics on the nano to microsecond timescale, force field-based molecular dynamics simulations have proven to be an effective tool.

In chapter 3, we have performed molecular dynamics simulations of different gold facets in contact with an electrolyte solution containing CTAB surfactants in order to understand the microscopic/molecular origin of anisotropic growth. Our simulations showed for the first time that on all the surfaces CTAB forms distorted cylindrical micelles spaced by water channels containing bromide ions and which can provide a path for the diffusion of the gold reactants toward the gold surface [102].

In this chapter, we investigate the influence of the halides on the growth mechanism using a combination of simulations and experiments. We aim to understand how the gold/surfactant/electrolyte interface changes when Cl^- replaces Br^- at different concentrations. The key question we want to address is how halides affect the interface structure and properties for the different facets. For this purpose, we simulate the microscopic mechanism of adsorption of CTAB/CTAC surfactant mixtures in different ratios on three gold surfaces namely, Au(111), Au(110) and Au(100). In particular, we analyze the surface passivation by halide ions, the packing density of CTA^+, the compactness of the surfactant layer and the potential difference between the bulk and the surfactant layer. Our model systems include pure CTAB, pure CTAC, mixture of 50% CTAB and 50% CTAC and mixture of 25% CTAB and 75% of CTAC in the growth solution. The simulations are then compared to experiments to validate our findings.

We find that the degree of binding of different halides to the gold surfaces has a direct influence on the surfactant layer at the interface. Replacing Br^- with Cl^- causes important structural rearrangement of the surfactant layer which becomes less compact. Also, the difference between facets based on the surface density of surfactant and ions specificity becomes less pronounced as the CTAB/CTAC ratio decreases. Finally when all Br^- is replaced by Cl^- only a few disordered CTA^+ molecules can bind to the gold surface, confirming that CTAC cannot exert a protecting action on the gold surface and is not able to inhibit the growth of any gold surface. The combined approach of atomistic molecular dynamics simulations and corresponding experiments provides a general framework to investigate the complex pro-

cesses occurring during nanocrystals formation linking properties at the solid/liquid interface to the morphology of the growing solid.

5.2 METHODS

5.2.1 *Computational section*

5.2.1.1 *Models and simulations details*

We first studied the adsorption of halides on gold/water interface. Details of the simulation models for the Au(111) surface/water interface in the presence of different halides are reported in Table 5.1, including box sizes and number of atoms. We have considered three different halides, namely Cl^-, Br^- and I^- in combination with the same number of Na^+ counterions in order to understand the adsorption of halide ions on Au(111) surface. The preassembled gold slab in a simulation box solvated with SPC water in order to prepare simulation models of Au(111) surface/water interface with different sodium halides. The ions were added to the system by randomly replacing them with water molecules.

In Table 5.2, details of the model systems for the gold/ electrolyte interface containing different types of surfactants are described. In particular box sizes and number of atoms for the 100% CTAB, 50% CTAB 50%CTAC, 25% CTAB 75% CTAC and 100% CTAC for the three surfaces Au(111), Au(110) and Au(100) are reported. The 100% CTAB model is the same we already used in chapter 3. A similar procedure as 100% CTAB was followed to build simulation models for other CTAB/CTAC systems.

All MD simulations have been performed using the GROMACS package (version 4.5.5) [84]–[87]. Periodic boundary conditions were applied in all three directions. Energy minimization was performed after the addition of water and ions to keep the maximum force on any atom below 1000 kJ $mol^{-1}nm^{-1}$. A constant temperature of 300 K and a constant pressure of 1 bar were maintained by the Berendsen and Parrinello-Rahman coupling

Table 5.1: Model details for halides on gold (111) surface (1.81 M, 3.87 and 7.78 M sodium halide).

Name of surface	No. of ions	No. of water molecules	Thickness of gold surface [nm]	Box dimensions X [nm], Y [nm] Z [nm]
1.81 M				
Au(111)	90 Na^+/90 Cl^-	2761	1.26	4.02, 4.02, 7.04
Au(111)	90 Na^+/90 Br^-	2761	1.26	4.02, 4.02, 7.03
Au(111)	90 Na^+/90 I^-	2761	1.26	4.02, 4.02, 7.04
3.87 M				
Au(111)	180 Na^+/180 Br^-	2581	1.26	4.01, 4.01, 7.03
Au(111)	180 Na^+/180 I^-	2581	1.26	4.01, 4.01, 7.02
7.78 M				
Au(111)	360 Na^+/360 Cl^-	2221	1.26	4.02, 4.02, 7.03
Au(111)	360 Na^+/360 Br^-	2221	1.26	4.02, 4.02, 7.03
Au(111)	360 Na^+/360 I^-	2221	1.26	4.01, 4.01, 7.02

scheme. A time step of 2 fs was employed and trajectories were stored at every 2 ps. The system was first equilibrated in the NVT ensemble (constant Number of particles, Volume, and Temperature) for 100 ps, subsequently NPT ensemble simulations were performed. MD production runs were performed for at least 200 ns for 100% CTAB Systems and runs up to 1000 ns were performed for CTAB/CTAC mixture and 100% CTAC systems (Table 5.2) in order to achieve equilibrium configurations. The system equilibration time was checked by the convergence of surface density of CTA^+ and Br^- as a function of time (Figure 5.1). Trajectories from the last 50 ns were used for analysis. In the case of the metal/electrolyte interfaces without surfactants (models in Table 5.1) shorter simulation time can already provide good statistical sampling. In this case, MD production runs of 50 ns were performed and trajectories from the last 10 ns were used for the analysis.

Table 5.2: Model details for different concentrations of CTAB/CTAC surfactant in water on the Au(111), Au(110) and Au(100) surfaces.

Name of surface	No. of CTAB/CTAC molecules	No. of water molecules	Thickness of gold surface [nm]	Box dimensions X [nm], Y [nm] Z [nm]
100% CTAB				
Au(111)	180/ 0	4982	1.26	4.07, 4.07, 15.47
Au(110)	180/0	4936	1.45	4.08, 4.08, 15.90
Au(100)	180/0	4884	1.43	4.1, 4.1, 15.61
50% CTAB	50%CTAC			
Au(111)	90/90	4802	1.26	4.06, 4.06, 15.44
Au(110)	90/90	4802	1.45	4.08, 4.08, 15.54
Au(100)	90/90	4802	1.43	4.1, 4.1, 15.61
25% CTAB	75% CTAC			
Au(111)	45/135	4982	1.26	4.07, 4.07, 15.49
Au(110)	45/135	4936	1.45	4.08, 4.08, 15.92
Au(100)	45/135	4884	1.43	4.11, 4.11, 15.64
100% CTAC				
Au(111)	0/180	4982	1.26	4.07, 4.07, 15.47
Au(110)	0/180	5651	1.45	4.14, 4.14, 15.75
Au(100)	0/180	4884	1.43	4.11, 4.11, 15.65

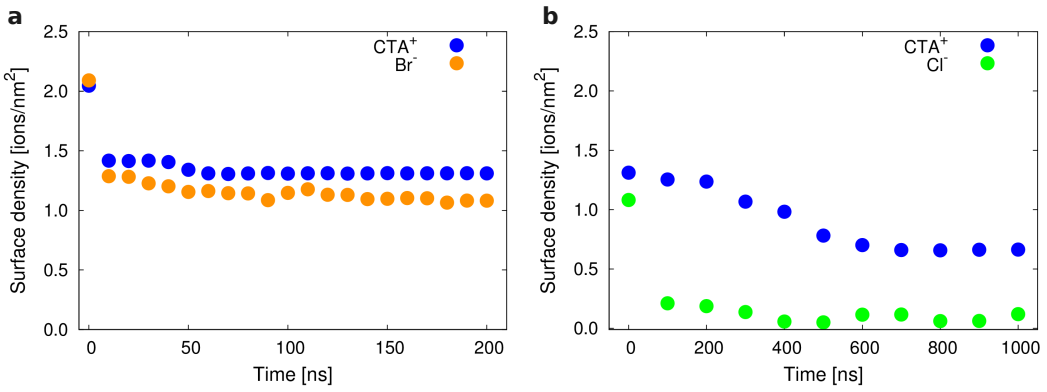

Figure 5.1: (a) Surface densities of CTA^+ and Br^- as a function of time for 100% CTAB on Au(111). (b) Surface densities of CTA^+ and Cl^- as a function of time for 100% CTAC on Au(111) surface.

5.2.1.2 *Forcefield parameters*

GROMOS96 53a6 forcefield [76] was employed for all our MD simulations. In particular the cetyltrimethylammonium cation (CTA^+) model proposed and validated by Wang and Larson [77] had been used in combination with the SPC water model. The charge assignment for CTA^+ is such that the three methyl groups in the headgroup and a methylene group adjacent to the nitrogen carry a partial positive point charge of + 0.25e each and the central nitrogen atom is set to be neutral [77]. The Lennard-Jones parameters of gold and halide ions are reported in Table 5.3. The Lennard-Jones parameters for bromide ion are from Van-Gunsteren [78]. The Lennard-Jones parameters for gold from Heinz *et al.* [79] were used for the metal description. These Lennard-Jones parameters quantitatively reproduce the density, surface tension, interface tension with water, as well as noncovalent adsorption of organic and biomolecules [106]. These parameters also accurately reproduce surface and interface energies and have been applied to study the adsorption mechanism of single CTAB surfactant molecule, hexadecylammonium chloride (HDAC), amino acids on Au(111) [89] and peptide [106] on Au(111) and Au(100) in aqueous solution. These forcefield parameters were already used in our previous work [102] providing an accurate description of the gold/CTAB electrolyte interface. The Lennard-Jones parameters for iodide ion are from Reif and Hunenberger [80]. They are compatible with ionic polarizability and are calibrated to reproduce single-ion hydration free energies derived from the experimental conventional hydration free energies along with a standard intrinsic hydration free energy of the proton.

5.2.2 *Experimental section*

5.2.2.1 *Materials*

In this section, the details about the experiments have been reported, which have been performed in the group of Prof. C. Sönnichsen and have been used to validate the predictions from the simulations. Deionized water from

Table 5.3: Lennard-Jones parameters of Au, Br^- and I^-.

Name	C6 [kJ mol^{-1} nm^6]	C12 [10^{-5} kJ $mol^{-1}nm^{12}$]
Au [79]	0.029227046	0.9650000
Cl^- [76]	0.01380625	10.6915600
Br^- [78]	0.027655690	6.5480464
I^- [80]	0.044452000	18.8618000

a Millipore system (> 18 MΩ, Milli Q) was used in all experiments. All chemicals were purchased from Sigma - Alldrich and used without any further purification.

5.2.2.2 *Synthesis of gold nanorods*

Gold nanorods were prepared in a two-step process according to literature [13]. First, seeds were prepared as follows: 50µL of 0.1 M tetrachloroauric acid ($HAuCl_4$) are added to 5.0 mL Milli Q water and mixed with 5.0 mL of 0.2 M cetyltrimethylammoniumbromide (CTAB) solution. During vigorous shaking, 0.60 mL of ice-cold 0.020 M sodiumborohydride ($NaBH_4$) was added resulting in the formation of a brownish-yellow or yellow suspension of seeds. The seed suspension was kept at 30 °C and used within one day. In a second step, seeds were grown to nanorods in the following way: 10mL of growth solution containing $5.0 \cdot 10^{-4}$ M $HAuCl_4$, (0.10-X) M CTAB, X M CTAC, $8.0 \cdot 10^{-5}$ M silver nitrate ($AgNO_3$) and $5.5 \cdot 10^{-4}$M ascorbic acid (AA) was prepared. X was varied between 0 and 0.1. AA changes the growth solution from dark yellow to colorless. After the addition of 12 µL of seeds, the solution changes color to blue or grayish-red within 10-20 min.

5.2.2.3 *Growth Kinetic*

Growth solutions with the same concentrations as for the synthesis of gold nanorods and a reduced total volume of 3 mL were prepared in a cuvette.

After addition of 7.2 µL seed solution and rapid mixing, UV/VIS transmission spectra were recorded every 3 seconds.

5.2.2.4 *TEM*

TEM images were recorded on a Philips EM420 using an operating voltage of 120 kV. TEM samples were prepared from about 1 ml of nanoparticle solution, centrifuged twice for 10 minutes at 9870 g (10000 rpm). The supernatant solution was first replaced by 1 ml and the second time by 300 µL of fresh water. A drop (5µL) of this concentrated solution was deposited on a 200 mesh formvar-coated copper grid and dried in air at room temperature. The particle sizes were measured on the TEM image manually and - when possible - with an automatic sizing tool using the Image Processing Toolbox of MATLAB. We cross-checked the reliability of the automatic count manually for every image series.

5.2.2.5 *Single nanoparticle spectroscopy (NanoSPR)*

We determined the change in resonance wavelengths $\Delta\lambda_{res}$ of gold nanorods induced by the coverage of CTAB or CTAC to verify the theoretical prediction of a thicker surfactant layer in the presence of bromide ions. This experiment was performed on a homebuilt dark-field microscope system that allows the automatic determination of many single nanoparticle spectra of gold nanorods immobilized at the bottom of a microfluidic flow cell [107]. The flow cell allows exposing the nanoparticles to different solutions. Before immobilizing gold nanorods in the flow cell by addition of a 1 M sodium chloride solution, we cleaned the cell by rinsing with 300 µL Hellmanex II, a commercial cleaning concentrate followed by 3 mL ultrapure water. The plasmon resonance wavelength λ_{res} (see Figure 5.2a) of about 40 individual nanoparticle within the field of view were automatically recorded before and after rinsing with different solutions. Generally, the plasmon resonance wavelength changes to larger wavelength if the particle environment's refractive index increases (due to adsorption of molecules, c.f. Figure 5.2b).

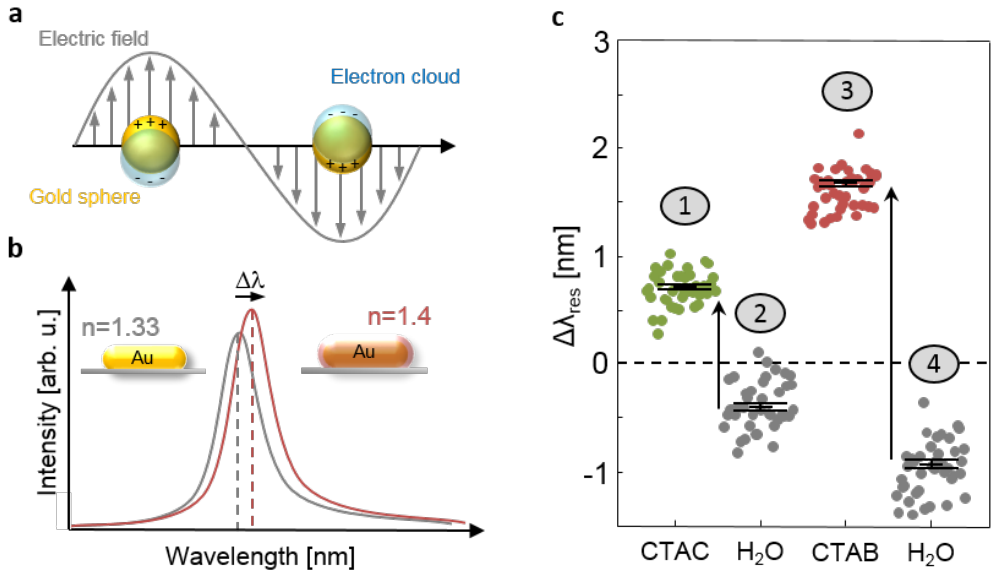

Figure 5.2: (a) A characteristic of noble metal nanoparticles is the appearance of particle plasmons upon excitation with light: The conduction electrons follow the electromagnetic field of the incoming wave. The resulting surface charges generate a restoring force which causes an oscillation. If excited at the eigenfrequency of this oscillation, the oscillation amplitude becomes very large and causes strong light absorption and/or scattering [108]. (b) Sketch of the light scattering spectra of a gold nanorod embedded in water (n=1.33) and with an additional surfactant layer on the surface (n=1.4, inset). The surfactant layer causes a resonance wavelength shift $\Delta\lambda_{res}$. (c) Original data (uncorrected) for the measurement shown in Figure 5.6 (see text for details). Each dot represents the spectral shift of the plasmon resonance of an individual nanoparticle.

To confirm the different adsorption properties of CTAB and CTAC predicted by the simulation, we performed the following sequence of experiments: The initial resonance position of the nanoparticles was recorded after extensive washing with pure water. These resonance positions serve as baseline for the following steps and we display only the shift with respect to this initial position in Figure 5.2b and Figure 5.2c. In a first step, we flushed in 300 µL of 0.01 M CTAC and recorded the resonance positions again (see Figure 5.2b, step 1). On average, the resonance positions shifted towards larger wavelength by about 0.7 nm. In a second step, we washed

again with 3 mL of pure water and recorded the resonance positions (Figure 5.2b, step2). The spectral positions shifted towards lower wavelength, as expected for the removal of bound CTAC molecules. However, to our surprise, the resonance position was slightly blue shifted by about 0.4 nm compared to the initial baseline. This blue shift is most likely caused by a charging effect induced by halide ion adsorption. The steps three and four repeat the same procedure as for step one and two - only replacing CTAC with CTAB. Both the redshift and the following blueshift are considerably more pronounced (Figure 5.2b). Because our primary interest is to compare the surface coverage of CTAC and CTAB, we corrected the shift caused by the charging effect by using the mean of step 2 as baseline for step 1 and the mean of step 4 as baseline for step 3. The resulting corrected plasmon shifts are shown in Figure 5.6c and used for the analysis of surface coverage and layer thickness.

5.3 RESULTS AND DISCUSSION

5.3.1 *Halides adsorption at the gold/water interface*

Before describing the more complex electrolyte solution containing the surfactants, we investigated the adsorption of the halide 'alone' at the interface. For this purpose, we have simulated the Au(111) surface in contact with a 1.81 M solution containing NaCl, NaBr or NaI, respectively. Snapshots from the simulation trajectories are reported in Figure 5.3 (a,b,c for NaCl, NaBr, and NaI solutions, respectively).

The simulations reproduced the expected difference in propensity for the gold surface[109], [110], with comparable strong binding for Br^- and I^-. Looking in more detail, we found that Br^- ions form two layers next to the gold surface with a higher number of ions in the first layer. (Ion density profiles are reported in Figure 5.3d-f). The likelihood to find the halides on the gold surface can also be expressed in terms of surface concentration, calculated as the number of ions in the first layer divided by surface area.

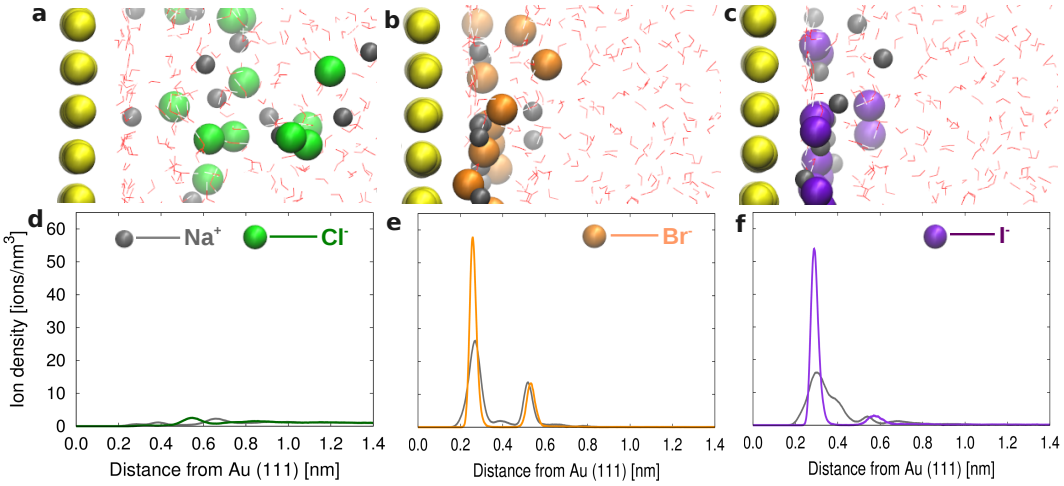

Figure 5.3: Snapshot from simulations for (a) NaCl, (b) NaBr, and (c) NaI in water on Au(111) surface. Ion densities as a function the distance from Au(111) surface for (d) NaCl, (e) NaBr and (f) NaI.

The number of ions in the first layer are calculated from the integral number (I.N.) in the first layer (see dotted lines in Figure C.1a-c in Appendix C)

The surface concentration of Cl^- ions (0.26 ions/nm^2) is negligible as compared to that of Br^- and I^- (2.06 and 2.07 ions/nm^2), showing that Cl^- ions prefer to remain in the solution, in contrast to Br^- and I^- ions which strongly adsorb on the gold surface. These propensities at the gold/water interface follows a similar trend to that observed at the air-water interface in the simulations by Jungwirth and Tobias [111] and at the hydrophobic solid surfaces in the simulations by Horinek and Netz [112].

The adsorption of ions on the surface also influences the interfacial electrostatic potential (details on the potential calculations can be found in the Appendix C). The potential difference between the Au(111) surface and bulk water is negative and it is not very much affected by the addition of NaCl. In contrast, the addition of NaBr and NaI to water leads to the formation of a screening layer at the metal /water interface and to a reduced electrostatic potential difference across the interface (see Figure C.1, C.2, C.3, more details in Appendix C on halide ions on Au(111) surface in water).

5.3.2 *Halides adsorption at the gold/water interface in the presence of surfactants*

To understand how the different surface affinity of Cl^- and Br^- affects the surfactant layer, we simulate electrolyte solutions containing 100% CTAB (2M solution), a mixture of 50% CTAB and 50% CTAC (1M CTAB, 1M CTAC), a mixture of 25% CTAB and 75% of CTAC (0.5 M CTAB, 1.5 M CTAC) and finally a 100% CTAC (2M solution). Figure 5.4a shows a snapshot of a simulation box containing the Au(111) surface, the CTAB layer, and the water layer after 200 ns. The CTAB headgroups favorably attach to the gold surface and form a distorted cylindrical micelle, where the CTAB headgroups arrange in the outer layer of the micelle and the CTAB tails arrange in the core of the micelle. A similar behaviour is observed on Au(110) and Au(100) as well, although with some differences in the ion densities.

The surface density of Br^- and CTA^+ is calculated as the number of ions in the first layer divided by surface area. The number of ions in the first layer are calculated from the integral number (I.N.) in the first layer (see dotted lines in Figure C.4a-c in Appendix C). The surface density of Br^- is higher on Au(110) and Au(100) than on Au(111) resulting in the passivation of a larger surface area (Table 5.4, Appendix C Figure C.4a-c). The lower surface passivation on Au(111) could translate into a higher reduction rate of gold species (such as $AuCl_2^-$) on Au(111). The anisotropic ion density also influences the surfactant surface (packing) density, which is higher on Au(110) and Au(100) (1.49 molecules/nm^2) which respect to that on Au(111) (1.31 molecules/nm^2) (Table 5.4).

The less compact surfactant layer on Au(111) could provide easier access to gold species in solution promoting a more efficient growth on such surfaces. Additional insight into the interfacial properties can be provided by the interfacial electrostatic potential. The potential difference between the bulk solution and the CTAB layer is higher along Au(111) than along Au(110) and Au(100) (see Appendix C Table C.3, C.4e), which could be another factor promoting a faster growth of gold nanorod along Au(111) surface.

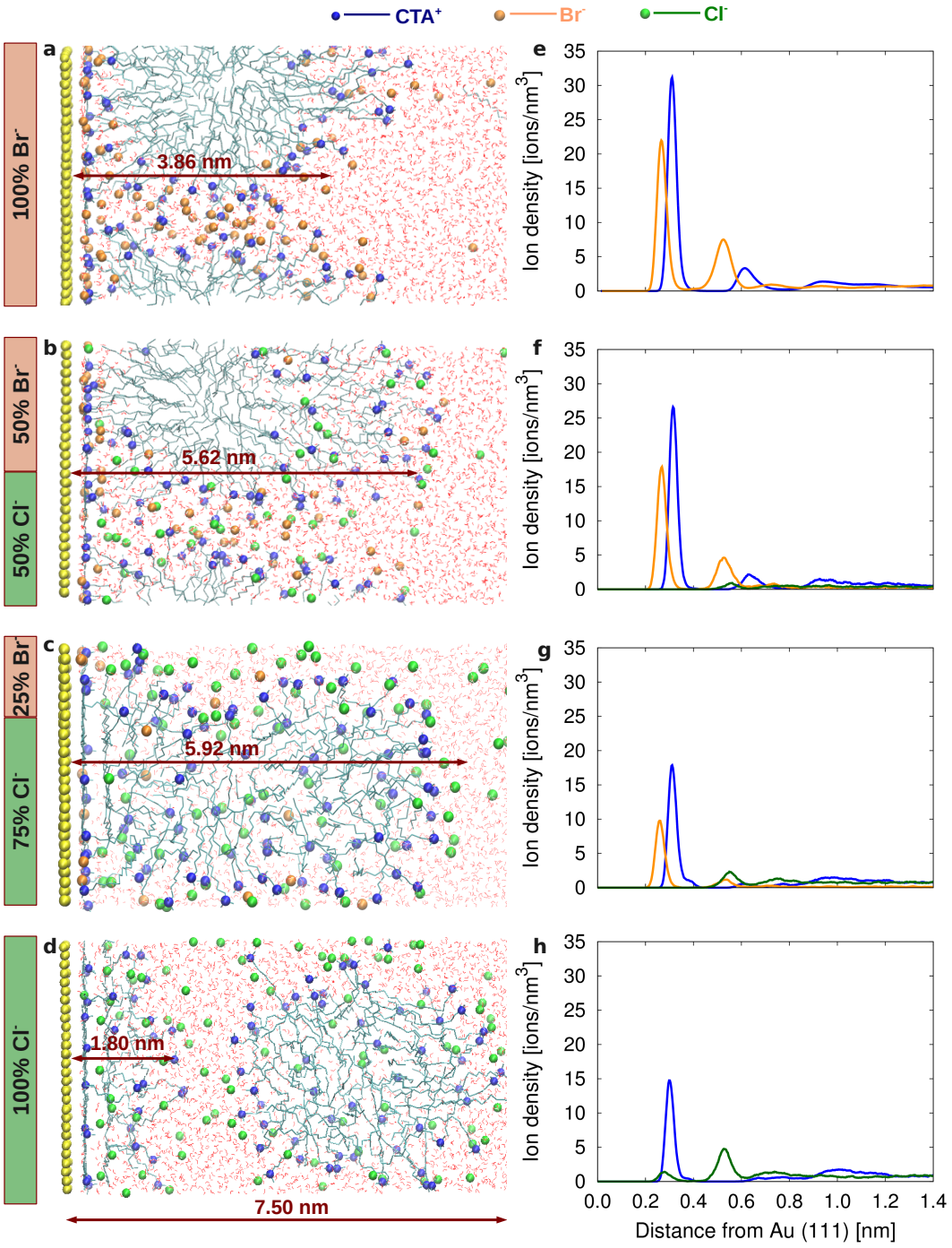

Figure 5.4: Snapshots from simulations for (a) 100% CTAB, (b) 50% CTAB 50% CTAC, (c) 75% CTAB 25% CTAC and (d) 100% CTAC. Ion densities as a function the distance from Au(111) surface for (e) 100% CTAB, (f) 50% CTAB 50% CTAC, (g) 75% CTAB 25% CTAC and (h) 100% CTAC (see Appendix C Figure C.4, C.5, C.6 and C.7 for Au(110) and Au(100)).

In order to study the effect of Cl^- on the surface properties, we repeated the simulations replacing 50% of Br^- by Cl^-. The surface density of Br^- on

Table 5.4: Surface densities of CTA^+, Br^- and Cl^- with different concentrations of CTAB/CTAC on different gold surfaces. Maximum standard error in the surface densities in 0.006 ions/nm^2

Name of surface	Au(111)	Au(110)	Au(100) [ions/nm^2]
CTA^+ 100% CTAB	1.31	1.49	1.49
CTA^+ 50% CTAB 50% CTAC	1.08	0.90	0.85
CTA^+ 25% CTAB 75% CTAC	0.97	1.18	0.78
CTA^+ 100% CTAC	0.66	0.67	0.65
Br^- 100% CTAB	1.09	1.41	1.40
Br^- 50% CTAB 50% CTAC	0.76	0.74	0.77
Br^- 25% CTAB 75% CTAC	0.56	0.84	0.82
Cl^- 50% CTAB 50% CTAC	0.06	0.03	0.01
Cl^- 25% CTAB 75% CTAC	0.17	0.15	0.12
Cl^- 100% CTAC	0.12	0.07	0.01

all the three surfaces is lower than in the 100% CTAB case (Table 5.4, Appendix C Figure C.5a-c), resulting into a reduced surface passivation and possibly an increased reduction rate. Interestingly, the lower Br^- density at the gold/water interface has a remarkable effect on the structure of the surfactant layer, which appears more stretched (and less compact) as compared to 100% CTAB case (Figure 5.4b). The CTA^+ packing density is reduced and the difference between facets becomes less pronounced (1.08, 0.90 and 0.85 molecules/nm^2 for Au(111), Au(110) and Au(100), respectively. This finding would support the idea that, in the mixture of CTAB/CTAC, the surfactant layer is not capable to significantly block the growth along any particular direction, resulting in a more isotropic growth. The interface potential between the surfactant layer and the bulk solution (see Appendix C Figure C.5 and

Table C.3) is also pointing to an isotropic behaviour along the three considered directions. As the CTAB fraction is further reduced to 25%, the CTA^+ packing density decreases and the surfactant layer becomes even less compact (Appendix C Figure C.6), and its structure even more stretched along the z direction (Figure 5.4c, see Figure C.8 and Table C.4 in Appendix C). The most striking results are certainly obtained for the 100% CTAC solution (Figure 5.4d,h, see Figure C.7 in Appendix C). The CTAC micelle adsorbed on the gold surface (Figure 5.5a) becomes more and more stretched in the z direction (orthogonal to the surface) as the simulation proceed (t= 300 ns in Figure 5.5b) and finally detaches from the gold surface moving into the bulk after 600 ns (Figure 5.4d or Figure 5.5c). Such a behaviour is certainly driven by the low propensity of Cl^- for the surface. A few surfactant molecules left on the gold surface tend to lay flat so to maximize the interaction between their hydrophobic tail with gold, while their headgroup orients towards the bulk solution. The thickness of the surfactant (disordered) layer is about 1.8 nm on Au(111) and Au(100) and 2.4 nm on Au(110) gold surface (see Table C.4 in Appendix C). In such a scenario, the thin surfactant layer will be unable to inhibit the growth of gold nanoparticle in any direction, explaining an isotropic, faster growth rate.

5.3.3 *Comparison of simulation results with the experiments*

The simulations predict several properties that can be tested experimentally: an increasing amount of chloride ions should lead to faster and more isotropic nanoparticle growth and CTAC should form a considerably thinner layer on gold than CTAB. We tested the first aspect by a series of nanoparticle synthesis where we varied the ratio of CTAC and CTAB in the growth solution. Transmission electron microscopy (TEM) images of the resulting particles are displayed in Figure 5.6a. The TEM images show the expected trend towards more isotropic particles with decreasing bromide concentration. A quantitative analysis of many TEM images, where we determined the fraction of rods versus spheres (see Figure C.9 in Appendix

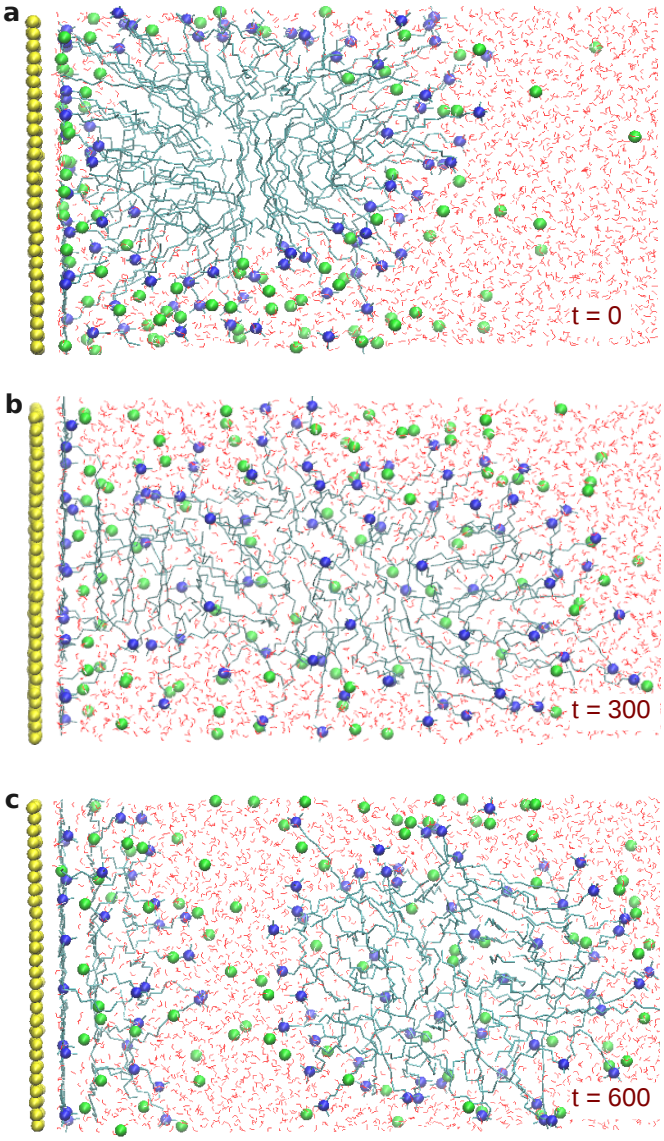

Figure 5.5: Snapshots from simulations containing CTAC layer on Au(111) in water at (a) t = 0, (b) t= 300 ns and (c) t = 600 ns.

C), confirm the trend as well (Figure 5.6b). In addition, we monitored the speed of the nanoparticle growth by following the optical absorption in the interband region at 450 nm (see Figure C.10 in Appendix C) which is a measure of nanoparticle volume. We extract an apparent rate constant from these volume growth curves using a Boltzmann-function (for resource limited growth). The reaction speed decreases when the amount of CTAB is increased (blue dots in Figure 5.6b) which confirms again the trend expected from the simulation.

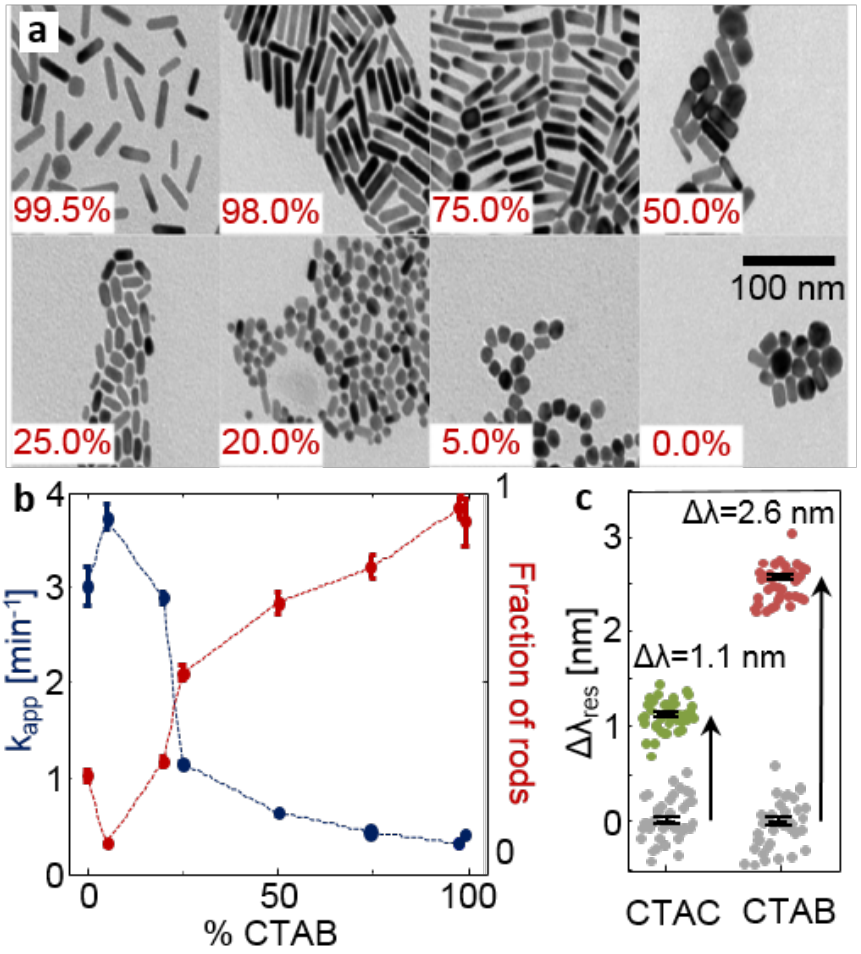

Figure 5.6: Experimental data: (a) representative transmission electron microscopy (TEM) images of gold nanorods synthesized with different percentages of CTAB in the growths solution, keeping the total CTAB+CTAC concentration constant. (b) Quantitative results of the percentage of rods over spheres extracted from TEM images as function of the CTAB percentage (red dots) and the corresponding apparent reaction rates determined by optical absorption (blue dots). (c) Plasmon resonance wavelengths shifts $\Delta\lambda_{res}$ of many individual gold nanoparticles immobilized in a water filled glass capillary, after exposure to 0.01 M CTAC (green dots) and CTAB (red dots). The gray points show the same particles after exposure to water. In the latter case, the observed shifts are an indication of the measurement accuracy. The black symbols show the mean values their standard error bars (statistics over about 40 particles)

To test the second prediction from the simulation, the thicker surfactant layer on the gold surface in the presence of bromide ions, we exploit the sensitivity of the plasmon resonance frequency of gold nanoparticles to the adsorbed layer of material [108]. Using a homebuilt dark-field microscope in combination with a scanning stage and a spectrometer [107], we determine the plasmon resonance position λ_{res} of about 40 gold nanoparticles before and after exposure to a solution containing either 0.01 M CTAB or CTAC. The exposure to CTAB/CTAC leads to a small but clearly measurable shift $\Delta\lambda$ in the plasmon resonance (Figure 5.6c, see Figure 5.2). As expected, the shift for CTAB is much larger than that measured after CTAC exposure (2.6 nm versus 1.1 nm). Since the plasmon resonance shift $\Delta\lambda$ is a function of layer thickness t and its refractive index, we have converted the measured values to a layer thickness. For this conversion, we use published values for the refractive index of CTAB about ($n = 1.4$) [113], [114] and simulation results for the plasmon resonance of gold nanoparticles in different media we obtained using the boundary element method [115](see Figure C.11 in Appendix C). This calculation resulted in a layer thickness of $t = 1.6$ nm and $t = 4.2$ nm for CTAC and CTAB, respectively. Interestingly, these values agree almost exactly with the results from the simulation: 1.80 nm and 3.86 nm (Figure 5.4 d and a, respectively).

5.4 CONCLUSIONS

We have presented here a detailed atomistic investigation of the gold/surfactant/electrolyte solution interface in order to address the role of halides on the protecting layer on the surface of gold nanoparticles. Our simulations show that CTAB is able to form a compact micellar layer on the gold surface which is actually denser on Au(100) and Au(110) with respect to Au(111). The key element in the micelle adhesion to the surface is the Br^- propensity for the gold surface. When Br^- is partially (eventually fully) replaced by Cl^-, the micelle prefer to diffuse into the electrlyte solution leaving the gold surface unprotected. Indeed for the CTAC system only a few sur-

factant molecules are sticking to the gold surface, leaving the surface itself more easily accessible to further gold reduction. Two sets of experiments, particle synthesis and plasmon shift measurements, confirm the trends expected from the simulations and agree quantitatively with the predicted values for the surfactant layer thickness. These experimental confirmations let us strongly believe that the atomistic simulations provide an accurate description of the underlying processes. The role of certain halide ions (bromide) to mediate, in a strongly crystal facet dependent way, the adhesion of cationic surfactant molecules, provides a better understanding in the way, additives direct nanocrystals growth towards specific shapes. Moreover, the combined computational and experimental approach provides a template for understanding nanocrystal growth dynamics in general which is a major step in the rational design to nanostructure formation from solution. In a next step, this approach should incorporate actual reaction steps to elucidate the intricate electrochemical and diffusive processes in this highly dynamical process.

6

ROLE OF THE SILVER IONS

6.1 INTRODUCTION

The role of silver ions in the silver-assisted seed-mediated growth has been a particularly challenging area of the mechanistic investigation of gold nanoparticles growth. To date, the exact mechanism of silver action in the anisotropic growth is still debated. The following mechanisms have been proposed:

- The underpotential deposition of silver ions occurs predominantly on lateral facets of gold nanorod which would lead to an anisotropic growth [34], [116].
- Silver ions form a complex with CTA^+ and Br^- and act as face-specific capping agent [35], [117].
- Silver ions alter the shape of CTAB micelle from spherical to cylindrical (soft template) [118].
- Murphy and co-workers observed that silver ions are not reduced to the metal during the nanoparticle growth [119]. Therefore, it has been also hypothesized that silver ions are adsorbed onto the gold nanoparticle surface in the form of AgBr restricting the growth in a facet dependent way.
- Silver ions play a role in symmetry breaking of nascent gold seed which leads to an anisotropic growth of gold nanoparticles [103].

Part of the challenge in establishing the role of silver in the anisotropic growth stems from the difficulty to experimentally characterize its oxidation state and its location on the gold nanoparticle. Michalitsch *et al.* found

that Ag adlayer deposited on Au(111) shifts from a (3×3) layer to the more open structure in the presence of chloride ions, so that AgCl monolayer deposit on the surface [120]. It may be possible that under weak reducing conditions, silver deposition to form an AgCl layer is favorable over the reduction of Au(I). Elemental analysis by energy dispersive analysis of X-rays (EDAX) does not reveal any silver metal in the final gold rods, but inductively coupled plasma - atomic emission spectroscopy (ICP-AES) analysis revealed the presence of Ag up to a total percentage of 4.5% [121]. It was observed that Ag(I) can be reduced to its elemental form in an aqueous solution by ascorbic acid only above pH=8. As in a typical synthesis pH is about 3, silver ions should not be reduced on the gold surface *via* UPD. Using advanced energy dispersive X-ray spectroscopy Jackson *et al.* showed that deposition of silver on the gold nanorod surface shows no preference for specific facets [118].

Recently, the adsorption of the CTAB-AgBr complex has been studied on different gold surfaces using DFT calculations [105]. It has been proposed that the CTAB-AgBr complex can be adsorbed on top of the gold surface releasing one of the Br^- atoms. This leaves an Ag^+ ion on the gold surface still with a Br^- coordinated to it and with a CTA^+ capping it. However, the cost of DFT calculations is limits the size of the investigated systems to a few hundreds atoms. To consider larger systems at the nanometric scale, also including the electrolyte solution, force field-based molecular dynamics simulations have proven to be an effective tool.

In this chapter, the adsorption of AgBr on the different gold surface in aqueous solution has been studied in order to understand the passivation of the different surfaces. Finally, the adsorption of silver ions has been investigated in the presence of the surfactant layer on different gold surfaces at different silver ions concentrations.

6.2 METHODS

6.2.1 *Models and simulations details*

We first studied the adsorption of AgBr at the gold/water interface in the absence of surfactant. Details of the simulation models for the Au(111) surface/water interface in the presence of AgBr are reported in Table 6.1, including box sizes and number of atoms. We have considered Ag^+ with the same number of Br^- counterions in order to neutralize the system. We have considered a 1.3-1.5 nm thick gold slab in contact with a 6.5 nm thick layer of the SPC water. Ag^+ and Br^- were added by randomly replacing water molecules.

In Table 6.2, details of the model systems for the gold/electrolyte interface containing surfactants without AgBr and with AgBr for the three surfaces Au(111), Au(110) and Au(100) are described. The model of gold/electrolyte containing CTAB in the absence of silver is the same as used in chapter 3.

Table 6.1: Model details for silver bromide on Au(111), Au(110) and Au(100) gold surfaces (6.25 M silver bromide solution).

Name of surface	No. of Ag^+/Br^- ions	No. of water molecules	Thickness of gold surface [nm]	Box dimensions X [nm], Y [nm] Z [nm]
Au(111)	270	2401	1.26	4.02, 4.02, 7.04
Au(110)	270	2401	1.45	4.06, 4.06, 7.07
Au(100)	270	2401	1.43	4.06, 4.06, 7.31

All MD simulations have been performed using the GROMACS package (version 5.0.5) [84]–[87]. Periodic boundary conditions were employed in all three directions. Energy minimization was performed after the addition of water and ions to keep the maximum force on any atom below 1000 kJ mol^{-1} nm^{-1}. A constant temperature of 300 K and a constant pressure of 1 bar were maintained by the Berendsen and Parrinello-Rahman coupling scheme. A time step of 2 fs was employed and trajectories were stored every

Table 6.2: Model details for different percentage of AgBr with CTAB in water on the Au(111), Au(110) and Au(100) surfaces.

Name of surface	No. of CTAB/AgBr	No. of water molecules	Thickness of gold surface [nm]	Box dimensions X [nm], Y [nm] Z [nm]
without Ag^+				
Au(111)	180/0	4982	1.26	4.07, 4.07, 15.47
Au(110)	180/0	4936	1.45	4.08, 4.08, 15.90
Au(100)	180/0	4884	1.43	4.1, 4.1, 15.61
20% Ag^+ on surface				
Au(111)	180/36	5466	1.26	4.10, 4.10, 15.59
Au(110)	180/36	5466	1.45	4.11, 4.11, 16.02
Au(100)	180/36	5466	1.43	4.15, 4.15, 15.77
50% Ag^+ on surface				
Au(111)	180/90	5466	1.26	4.09, 4.09, 15.85
Au(110)	180/90	5466	1.45	4.11, 4.11, 16.05
Au(100)	180/90	5466	1.43	4.14, 4.14, 16.00

2 ps. The system was first equilibrated in the NVT ensemble for 100 ps, subsequently NPT ensemble simulations were performed. MD production runs were performed for at least 500 ns in order to achieve equilibrium configurations. The relaxation was checked by the convergence of surface densities of CTA^+, Br^- and Ag^+ as a function of time. In the case of the metal/electrolyte interfaces without surfactant (models in Table 6.1) shorter simulation time can already provide a good statistical sampling. In this case, MD production runs of 100 ns were performed and trajectories from the last 10 ns were used for analysis.

6.2.2 *Forcefield parameters*

The forcefield parameters for CTAB and gold are same as used in chapter 3. The Lennard-Jones parameters for silver ions are from the Ref. [81] (Table 6.3).

Table 6.3: Lennard-Jones parameters of Au, Ag^+ and Br^-.

Name	C6 [kJ mol^{-1} nm^6]	C12 [10^{-5} kJ $mol^{-1}nm^{12}$]
Au [79]	0.029227046	0.9650000
Ag^+ [81]	0.00013	0.0005
Br^- [78]	0.027655690	6.5480464

6.3 RESULTS AND DISCUSSION

6.3.1 *Adsorption of AgBr on different gold surfaces (without surfactants)*

As first step, the adsorption of silver bromide has been investigated on Au(111), Au(110) and Au(100) in aqueous solution. For the moment no surfactant is added to the solution. A 6.25 M AgBr solution was considered. The Ag^+ and Br^- ions adsorb in the form of hexagonal structure on the all three surfaces (Figure 6.1). The structure contains 3 Ag^+ and 3 Br^- ions which are coordinated alternatively. In such a structure, a Br^- ion is coordinated to 3 Ag^+ ions and a Ag^+ is coordinated to 3 Br^- ions.

Figure 6.2 presents the radial distribution function (RDF) of Ag^+ with Br^- on Au(111), Au(110) and Au(100) surfaces. The first peak provides the distance between the Ag^+ and Br^- in the adsorbed AgBr layer on the gold surface, which is also the side length of the hexagonal lattice shown in Figure 6.3. The dimensions of the hexagonal lattice are reported in Figure 6.3. The side length of the hexagonal lattice is 0.23 nm on Au(111), Au(110) and Au(100). The length of the major or vertical axis is given by the second peak in Figure 6.2, which is 0.46 $\pm$ 0.013, 0.35 $\pm$ 0.004 nm and 0.46 $\pm$ 0.011 nm for Au(111), Au(110) and Au(100) respectively (Figure 6.2a, b, c). The dimensions of the hexagonal lattice are comparable for Au(111) and Au(100), whereas for Au(110), the hexagonal lattice is contracted along one of the axis.

Table 6.4: Surface densities of Ag^+ and Br^- on different gold surfaces. Maximum standard error in the surface densities is 0.006 ions/nm^2.

Name of surface	Au(111)	Au(110)	Au(100) [ions/nm^2]
Ag^+	7.68	7.80	4.12
Br^-	7.47	7.80	4.14

The Ag^+ and Br^- surface density is higher on Au(110) than on Au(111) (Table 6.4). Indeed, although the same amount of AgBr is considered in three simulations, Au(110) surface is not fully covered with AgBr, and there is an uncovered patch (Figure 6.1h). On Au(111), both Ag^+ and Br^- have a 3-fold coordination to the surface gold atoms (Figure 6.3a). On Au(110), in the hexagonal structure, Ag^+ and Br^- ion may have either coordination number 5 or 2 with the gold atoms depending on the adsorption site (Figure 6.3b). On Au(100), the coordination number of Ag^+ and Br^- ions with gold atoms may be either 4 or 2 depending again on the adsorption site (Figure 6.3c).

Overall, the adsorption of silver ions is stronger on Au(110) and Au(100) as compared to Au(111). This can be inferred from the diffusivity of silver ions on Au(110), which is much lower on Au(111) (Table 6.5). The diffusivity was calculated from the mean square displacement (MSD) of the ion using the Einstein relation [122].

Table 6.5: The diffusivity of Ag^+ on different gold surfaces.

Au(111)	Au(110)	Au(100) [cm^2/s]
7.86×10^{-8}	4.28×10^{-10}	4.31×10^{-9}

6.3.2 *Adsorption of AgBr with CTAB on different gold surfaces*

In the silver assisted seed-mediated growth, the presence of 5% of Ag^+ already raises the yield of gold nanorods to nearly 100%, although, higher concentration (comparable to CTAB concentration 0.1 M) of Ag^+ are also

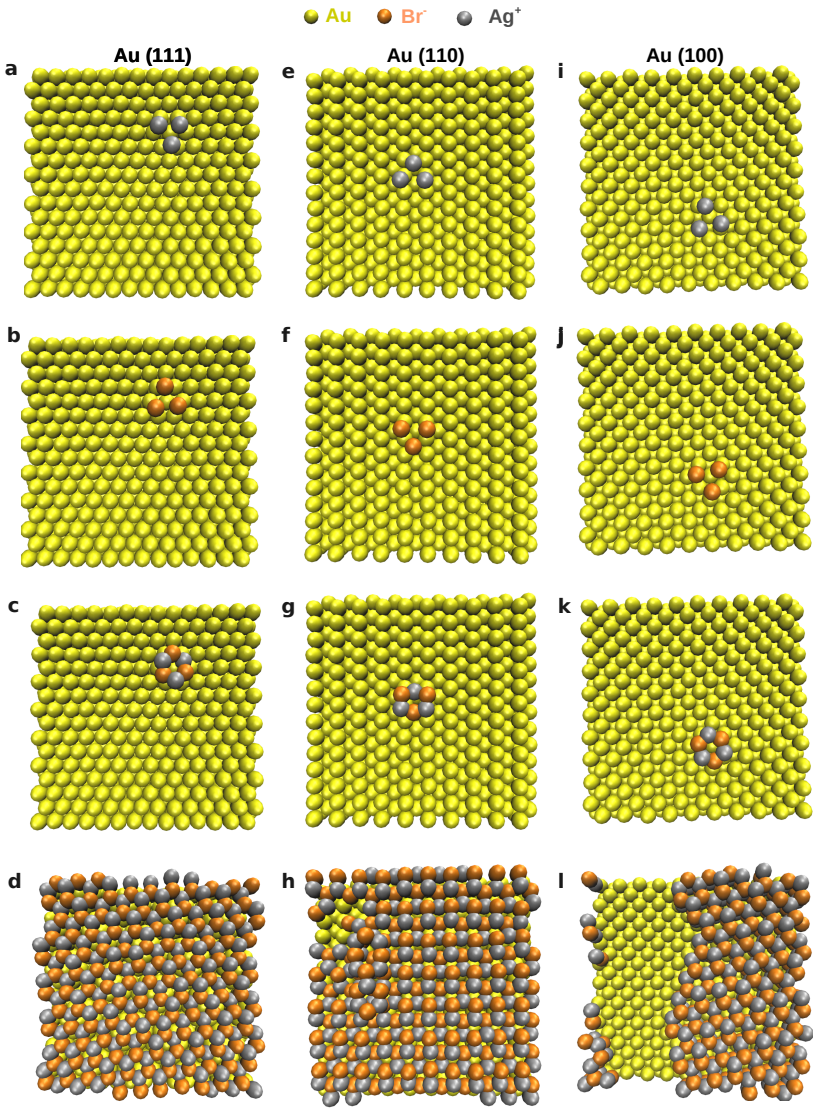

Figure 6.1: Adsorption of AgBr layer on Au(111) (a) three Ag^+ ions of the hexagonal structure, (b) three Br^- ions of the hexagonal structure (c) structure of hexagonal ring formed on Au(111) surface and (d) passivated monolayer of AgBr on Au(111). Adsorption of AgBr layer on Au(110) (e) three Ag^+ ions of the hexagonal structure, (f) three Br^- ions of the hexagonal structure, (g) structure of hexagonal ring formed on Au(110) surface and (h) passivated monolayer of AgBr on Au(110). Adsorption of AgBr layers on Au(100) (i) three Ag^+ ions of the hexagonal structure, (j) three Br^- ions of the hexagonal structure, (k) structure of hexagonal ring formed on Au(100) surface and (l) passivated bilayer of AgBr on Au(100).

used [14]. However from the experiments, it is not known what would be the actual concentration at the interface, namely the Ag^+ surface density. Given

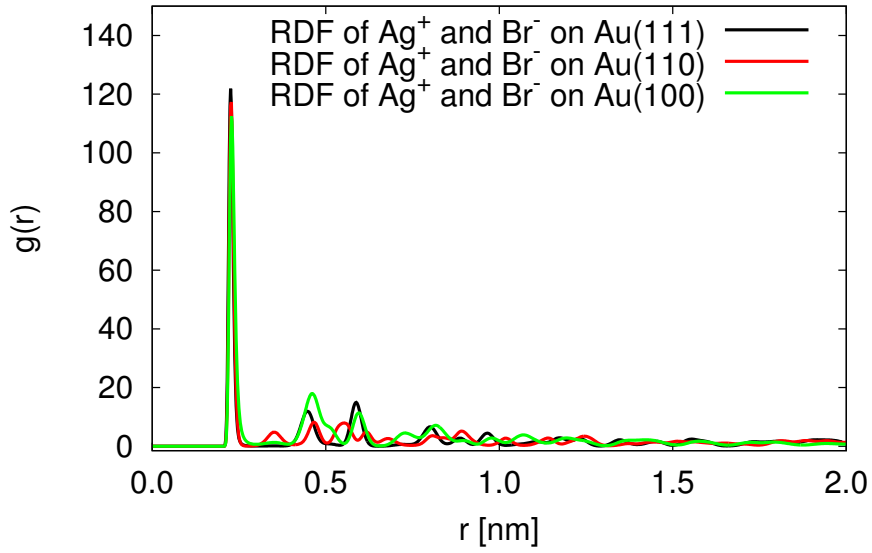

Figure 6.2: Radial distribution function of Ag^+ and Br^- on Au(111), Au(110) and Au(100).

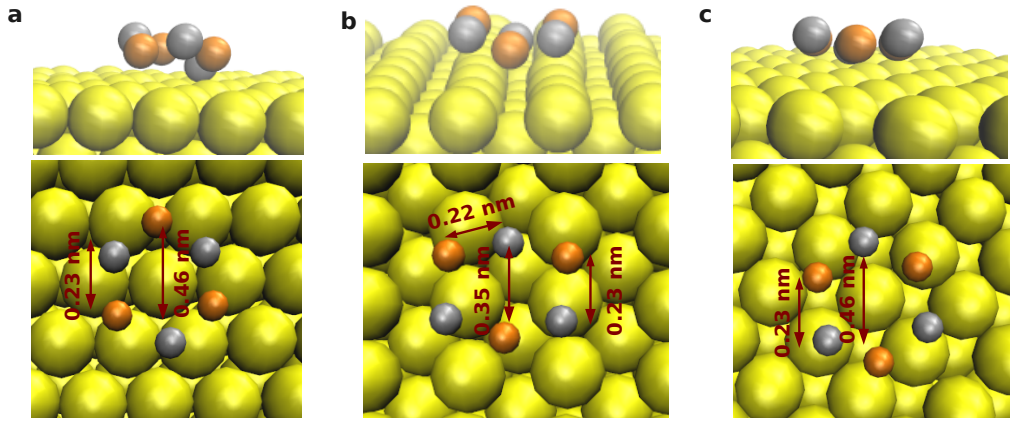

Figure 6.3: Hexagonal structure's dimensions (side and top view) on (a) Au(111), (b) Au(110) and (c) Au(100).

the high propensity of Ag^+ to adsorb on the gold surface, it is expected that, even in the presence of a relative low concentration of $AgNO_3$ in the electrolyte solution, the surface concentration of Ag^+ at the interface may be quite high. Therefore, we simulate two different electrolyte solutions containing a number of AgBr which corresponds to the 20% of CTAB molecules (20% AgBr) and to the 50% of CTAB molecules (50% AgBr), respectively. In both cases, we equilibrate the interfacial surfactant layer allowing the AgBr

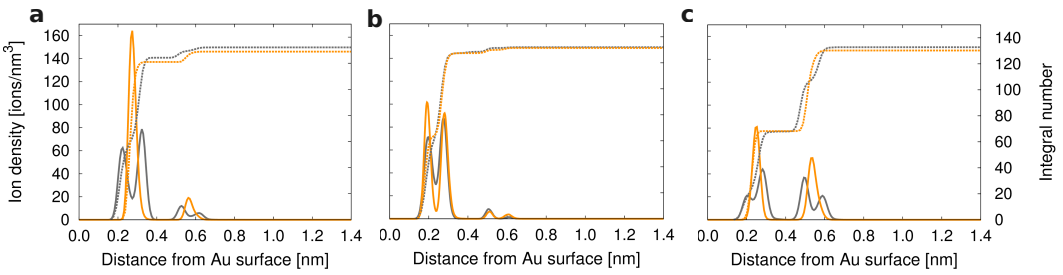

Figure 6.4: Ion densities and integral numbers of Ag^+ and Br^- on (a) Au(111), (b) Au(110) and (c) Au(100) as a function of the distance from Au surface.

to adsorb on the gold surface (in the presence of water) and then adding the CTAB bilayer.

Table 6.6: Surface densities of CTA^+, Br^- and Ag^+ with and with out Ag^+ on different gold surfaces. Maximum standard error in the surface densities is 0.01 ions/nm^2.

Name of surface	Au(111)	Au(110)	Au(100) [ions/nm^2]
CTA^+ without Ag^+	1.31	1.49	1.49
CTA^+ with 20% Ag^+ on surface	1.61	1.56	1.60
CTA^+ with 50% Ag^+ on surface	1.13	1.48	1.41
Br^- without Ag^+	1.09	1.41	1.40
Br^- with 20% Ag^+ on surface	2.14	2.65	2.09
Br^- with 50% Ag^+ on surface	3.58	3.71	3.75
Ag^+ with 20% Ag^+ on surface	1.06	1.05	1.04
Ag^+ with 50% Ag^+ on surface	2.63	2.64	2.55

6.3.2.1 *The 20% AgBr system*

Our first aim here is to understand how the structure and the stability of the surfactant layer are affected by the presence of AgBr. In the case of the 20% AgBr system, the surfactant layer is stable over a 500 ns trajectory. A snapshot of the surfactant layer for the different surfaces is reported in

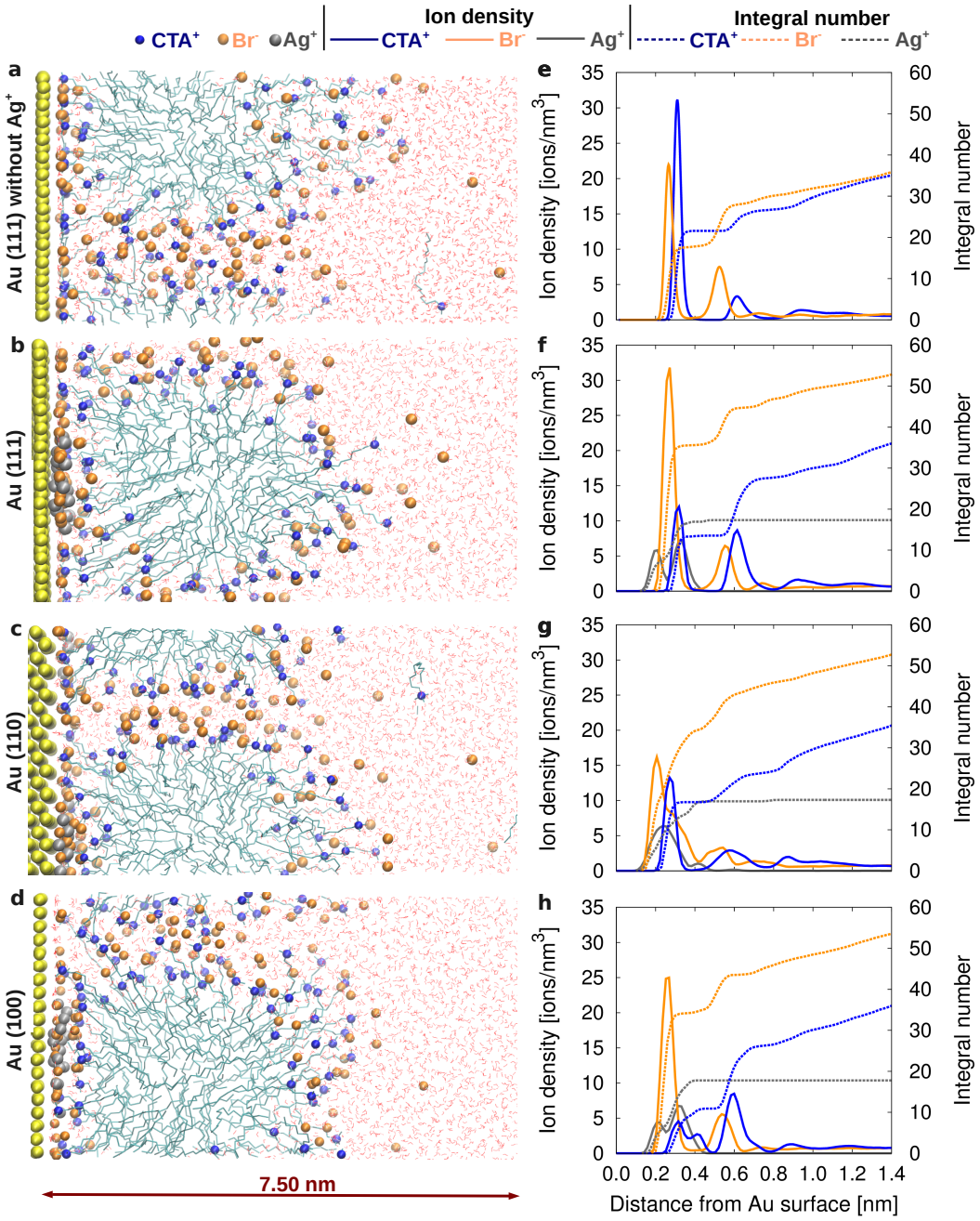

Figure 6.5: Snapshots from simulation for CTAB in water without Ag^+ on (a) Au(111), with 20% Ag^+ on (b) Au(111), (c) Au(110) and (d) Au(100). Ion densities as a function the distance from gold surface for CTAB in water without Ag^+ on (e) Au(111), with Ag^+ on (f) Au(111), (g) Au(110), (h) and Au(100).

Figure 6.5 b, c, d. Ag^+ is directly adsorbed on the gold surface and forms together with Br^-, the first adsorbed layer (Figure 6.5 f, g, h, gray line in the

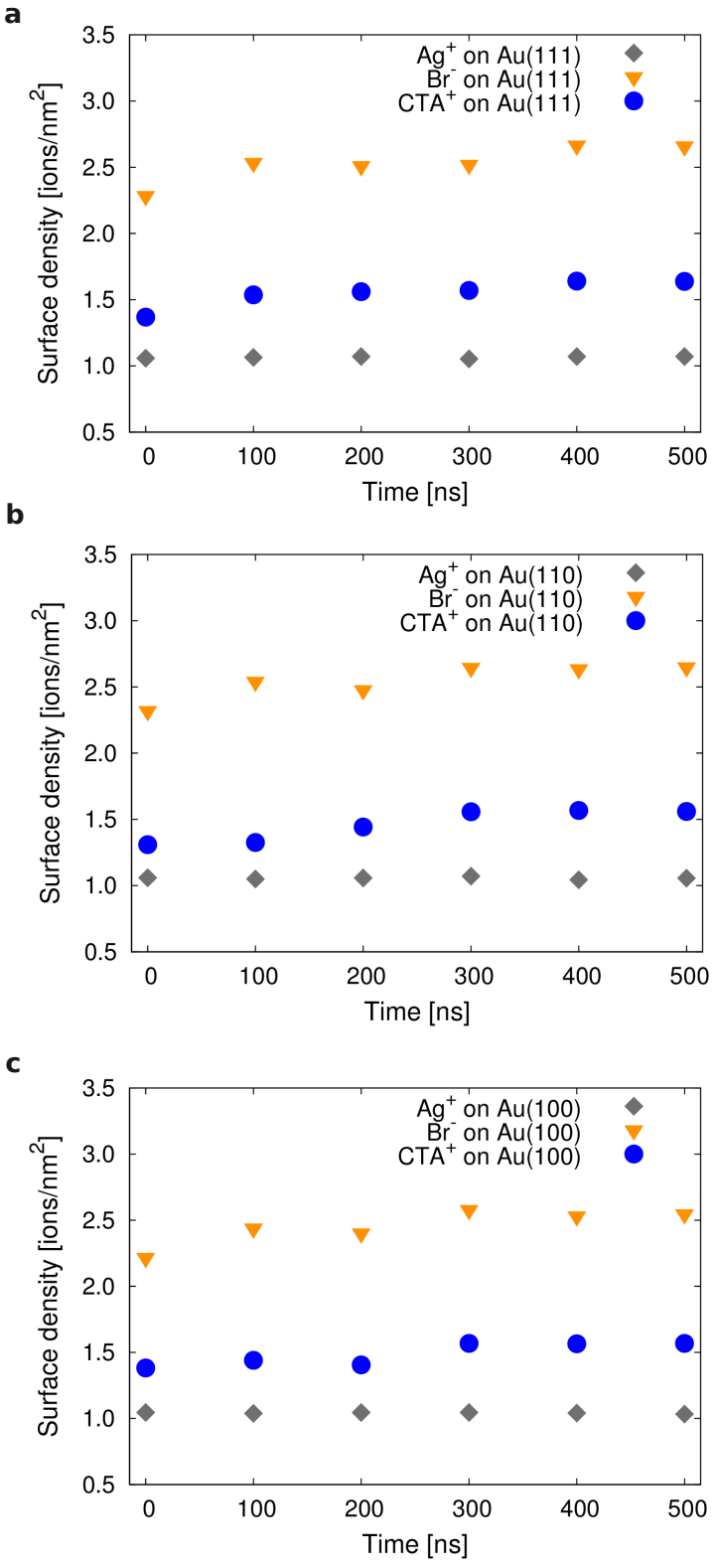

Figure 6.6: Surface densities of CTA^+, Br^- and Ag^+ as a function of time for 20% AgBr on (a) Au(111), (b) Au(110), (c) and Au(100).

Table 6.7: Thickness of CTAB layer with and with out Ag^+ on different gold surfaces. Maximum standard error in the thickness is 0.04 nm.

Name of surface	Au(111)	Au(110)	Au(100) [nm]
without Ag^+	3.86	3.74	3.85
with 20% Ag^+ on surface	4.07	4.20	4.14
with 50% Ag^+ on surface	4.35	3.97	4.25

Table 6.8: Potential difference between bulk solution and CTAB layer with and with out Ag^+ on different gold surfaces. Maximum standard error in the potential difference is 0.02 V.

Name of surface	Au(111)	Au(110)	Au(100) [V]
without Ag^+	0.86	0.83	0.82
with 20% Ag^+ on surface	0.87	0.83	0.84
with 50% Ag^+ on surface	0.97	0.83	0.77

density profile). It is worth mentioning that in our model Ag^+ and Br^- are adsorbed in the ionic form on the surface.

The Ag^+ adsorption drives a higher concentration of Br^- on the surface with respect to the case where no Ag^+ is present (e.g. the Br^- surface density raises from 1.09 ions/nm^2 in the absence of silver ions to 2.14 ions/nm^2 in the presence of silver ions on Au(111)). Overall, on all the three planes, passivation by the Br^- is increased. The first peak in the density profile of CTA^+ becomes broader as compared to the case without silver ions and the second density peak of CTA^+ increases as fewer CTA^+ now are adsorbed on the gold surface which is AgBr passivated (Figure 6.5 e, f, g, h). The surface densities of CTA^+, Br^- and Ag^+ are reported in Table 6.6. The convergence of surface densities has been investigated over a 500 ns trajectory. Figure 6.6 shows the surface densities of CTA^+, Br^- and Ag^+ on Au(111), Au(110) and Au(100) as a function of time.

The CTA^+ surface density on Au(111), Au(110) and Au(100) are almost similar in this case (blue dots in Figure 6.6). However, the surface density of Br^- is higher on Au(110) as compared to that on Au(111) (orange dots in Figure 6.6). Also, the electrostatic potential difference between bulk and the surfactant layer is higher along Au(111) direction.

6.3.2.2 *The 50% AgBr system*

To understand the effect of the silver concentration on the adsorption of the CTAB surfactant we have also considered additional systems, which include an amount of Ag^+ equal to the 50% of CTA^+ (Figure 6.11). These systems have also been investigated over a 500 ns trajectory (Figure 6.10).

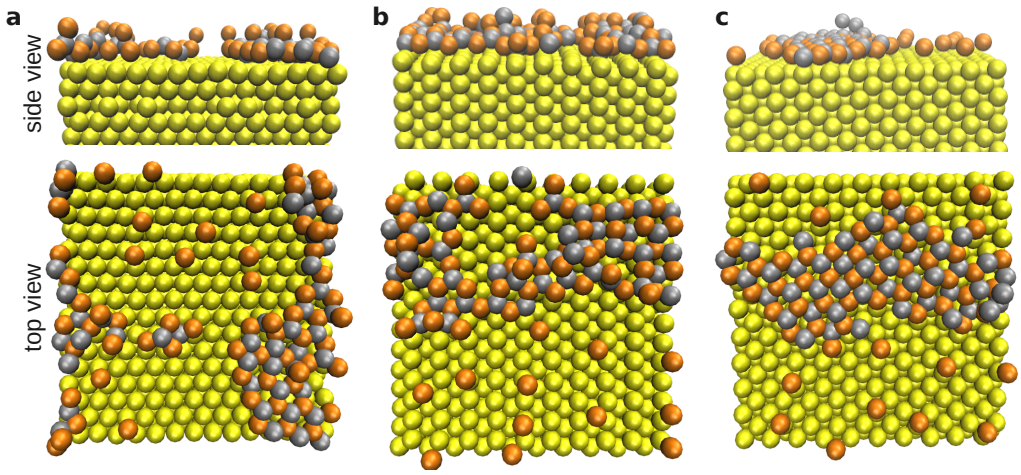

Figure 6.7: Snapshots from the simulations of the 50% AgBr System. Top and side view of AgBr layer on (a) Au(111), (b) Au(110) and (c) Au(100).

AgBr is adsorbed on the gold surfaces forming a hexagonal lattice similar to that observed in the system without CTAB (Figure 6.7). However, in particular on Au(100), the coexistence of hexagonal and square lattice arrangement is also observed (Figure 6.7c). Clearly, the pattern of the passivated AgBr monolayer in the presence of the surfactant changes as compared to that formed in the pure water solution on gold surfaces. Figure 6.8 presents the RDF of Ag^+ with Br^-. The first peak in the RDF shows that the average distance between Ag^+ and Br^- is 0.23 nm. Figure 6.9 shows the cumulative number of the RDF which shows that the coordination number of Ag^+ with Br^- is 3 on all three surfaces.

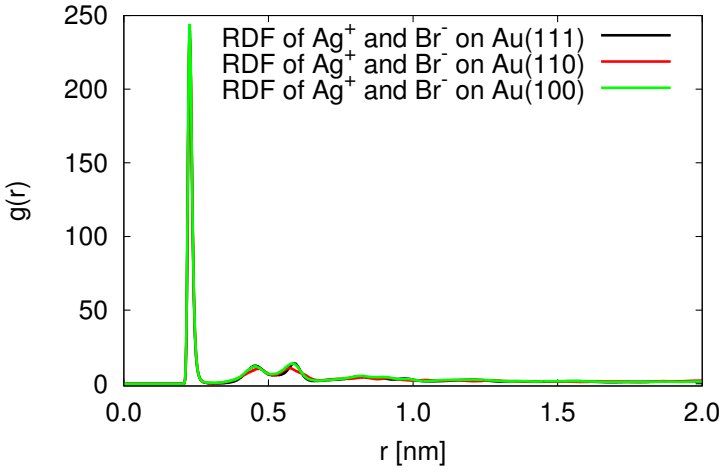

Figure 6.8: Radial distribution function of Ag^+ with Br^- in the case of 50% AgBr on (a) Au(111), (b) Au(110) and (c) Au(100).

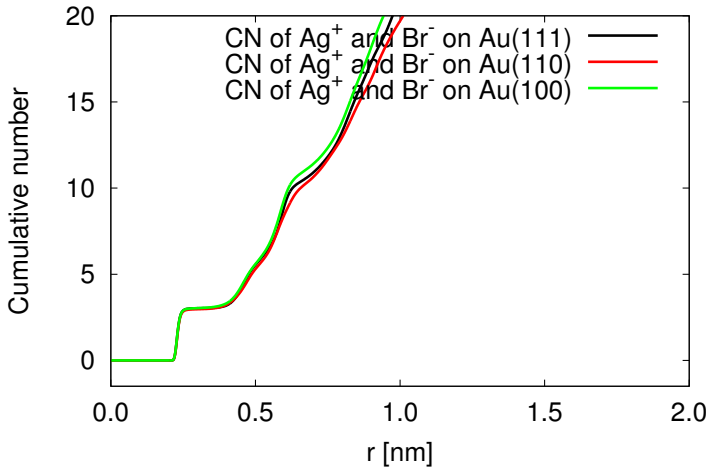

Figure 6.9: Cumulative number (CN) of Ag^+ with Br^- in the case of 50% AgBr on (a) Au(111), (b) Au(110) and (c) Au(100).

Table 6.9 shows the diffusivity of CTA^+ and Ag^+ on the gold surfaces in the case of 20% AgBr and 50% AgBr. Overall the diffusivity of CTA^+ decreases on all the surfaces as the surface coverage of AgBr increases. The Ag^+ ion density (silver colour solid line in Figure 6.11) on all three surfaces has two peaks very close to the gold surface which correspond to two different Ag^+ layers on the gold surfaces. In this case, the surface densities of CTA^+ and Br^- are higher on Au(110) and Au(100) than Au(111) (Table 6.6).

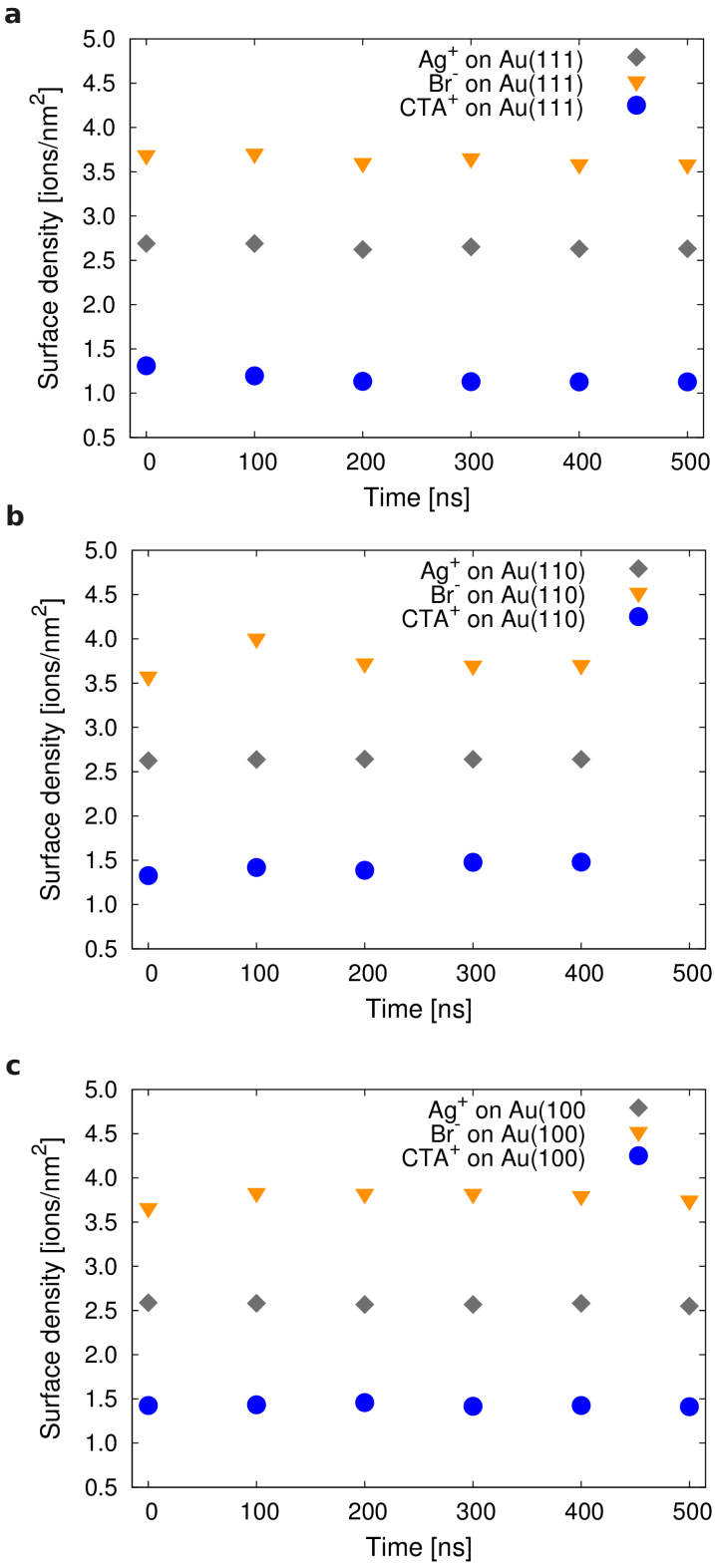

Figure 6.10: Surface densities of CTA^+, Br^- and Ag^+ as a function of time for 20% AgBr on (a) Au(111), (b) Au(110) and (c) Au(100).

Also, the potential difference between the bulk and the surfactant layer is higher for Au(111) than for Au(110) and Au(100) (Table 6.8, Figure 6.12).

Table 6.9: Lateral diffusivity of CTA^+ and Ag^+ on different gold surfaces.

Name of surface	Au(111)	Au(110)	Au(100) [cm^2/s]
CTA^+ with 20% AgBr	7.7×10^{-6}	8.6×10^{-6}	8.0×10^{-6}
CTA^+ with 50% AgBr	6.7×10^{-6}	8.2×10^{-6}	8.0×10^{-6}
Ag^+ with 20% AgBr	1.5×10^{-8}	6.0×10^{-8}	0.3×10^{-8}
Ag^+ with 50% AgBr	1.2×10^{-8}	8.6×10^{-8}	3.3×10^{-8}

Table 6.7 shows the thickens of the CTAB layer on Au(111), Au(110) and Au(100) in the case of with and without silver ions in the growth solution. The thickness of the CTAB layer is around 4 nm with silver ion which is slightly larger than without silver ion that is 3.80 nm which is due to the adsorption of AgBr layer on the gold surfaces.

6.4 CONCLUSION

MD simulations of adsorption of AgBr on gold in water reveals that AgBr adsorbs in the form of a hexagonal lattice. It is more strongly bounded to the Au(110) surface than the Au(111) in the presence of surfactant. The passivation by AgBr decreases the surface density of CTA^+ on Au(111) and increases the surface density on Au(110) and Au(100) as compared to the surface density in the absence of silver ions. The potential difference between the bulk water and the CTAB layer is also higher across Au(111) interface than across Au(110) and Au(100).

Thus, the gold/electrolyte interfaces in presence of the silver ions shows the same anisotropic behaviour in terms of surfactant coverage as observed in the absence of the silver ions. The shape of the surfactant micelle is also similar to that observed in the absence of silver ions. However, the layer thickness and overall Br^- passivation is increased on all the surfaces.

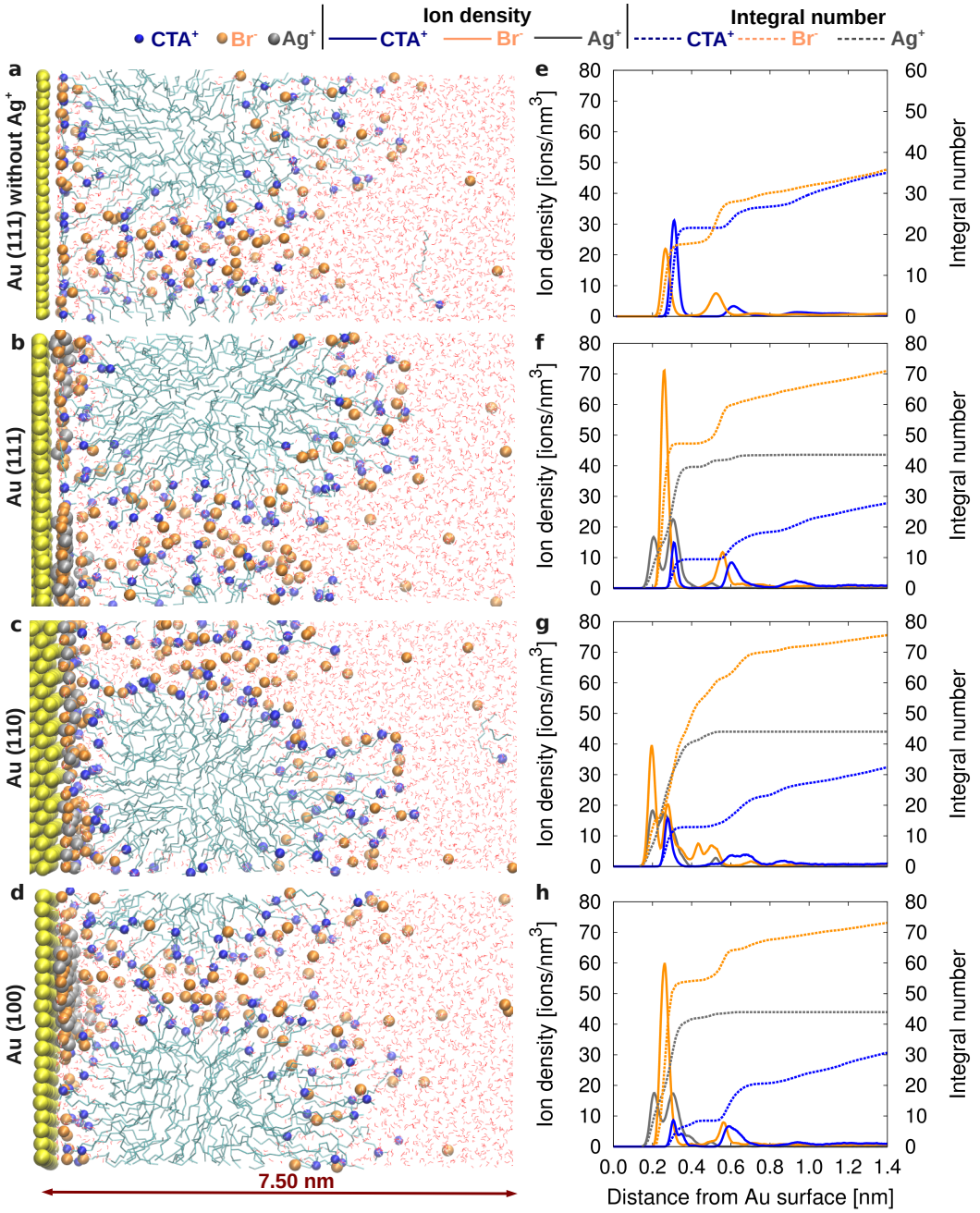

Figure 6.11: Snapshots from simulations for CTAB in water without Ag^+ on (a) Au(111), with 50% Ag^+ on (b) Au(111), (c) Au(110) and (d) Au(100). Ion densities and integral numbers as a function distance from gold surface for CTAB in water without Ag^+ on (e) Au(111), with Ag^+ on (f) Au(111), (g) Au(110) and (h) Au(100).

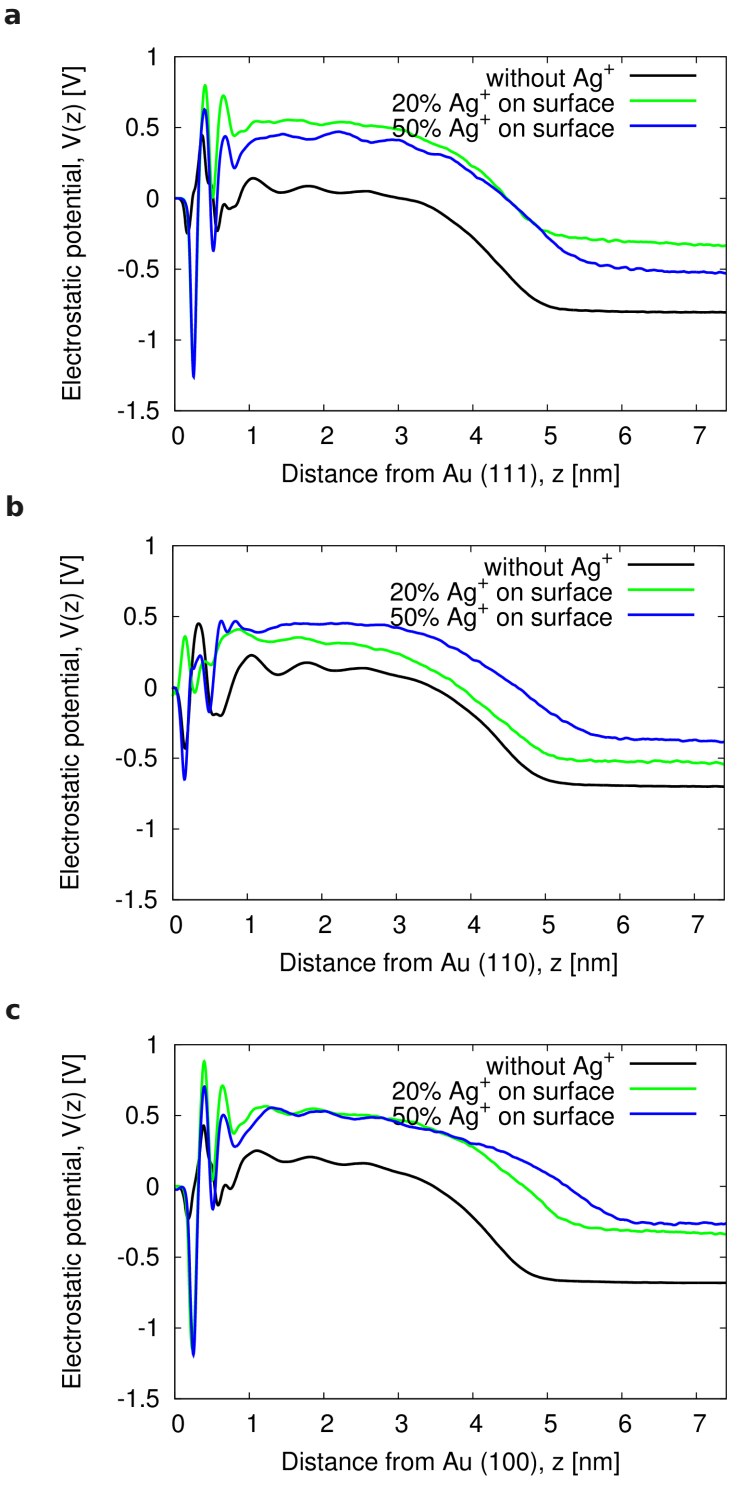

Figure 6.12: Electrostatic potentials as a function of the distance from the gold surface for without Ag^+, 20 % Ag^+ and 50% Ag^+ concentrations containing CTAB in water on (a) Au(111), (b) Au(110) and (c) Au(100).

7

CONCLUSIONS

In this work, we have used molecular dynamics simulations to investigate the microscopic origin of the anisotropic growth of gold nanoparticles in the electrolyte solution containing surfactants and ions. Force field based MD simulations have permitted to model different systems at nanoscale, where dynamics and temperature effects are included and microsecond time scale is explored.

The different factors influencing the growth have been selectively included in the models in order to unravel the role of different molecules of the growing solution. In particular, both infinite planes models, representing the mature stage of the growth, and nanoseed models in the size of a few nanometers have been used to understand how asymmetry between the different facets of the nanorods builds up.

Our simulations revealed the structure of the surfactant layer at the atomistic details: CTAB molecules adsorb in the form of distorted cylindrical micelles spaced by water channels containing bromide ions which provide a path for the diffusion of the gold reactants towards the gold surface. When the low index facets are examined, a lower surface density of CTAB is found on the Au(111) facets, with respect to the Au(100) and Au(110). In addition, a higher electrostatic potential difference is measured between the gold surface and the bulk solution at the Au(111) interface, which would provide a stronger driving force for the negatively charged $AuCl_2^-$ species which are reduced at the gold surface. The two factors together would result into higher diffusion flux of the gold reactant toward the Au(111) facets and could result into a preferential growth of gold nanorod in the Au(111) direction.

Interestingly, higher index facets, which have also been experimentally observed in the mature nanorods, behave similar to the low index Au(100) and Au(110). However, they exhibit a difference with respect to the Au(111). The observed difference among different infinite planes would support the mechanism of an isotropic growth when a nanoparticle of the size larger than the micellar size is considered.

In order to investigate if the difference in the facets is preserved on a small scale, we also investigated small nanoseeds, whose dimensions are comparable to those of the CTAB micelle. In particular, we considered both penta-twinned decahedral seeds of aspect ratio 1 and 2 and a cuboctahedron.

The striking result from the simulation is that the asymmetry, which characterized the infinite planes, shows up more dramatically on the nanoseeds. Indeed, while on the Au(100) and Au(110) facets of both the cuboctahedral and penta-twinned seeds the CTAB adsorbs in micellar layer with a structure similar to that observed on the infinite plane, basically no micellar adsorption is found on the small Au(111) facets, which form the tips of the penta-twinned nanoseeds. This huge difference in the early stage seeds would then promote a symmetry breaking in the penta-twinned seeds and, therefore, an anisotropic growth of nanocrystals.

As a further step, we have investigated the influence of the halides on the surfactant ability to promote the anisotropic growth. This was motivated by the established experimental evidence that CTAB (surfactant with the Br^-) is favoring elongated rod shapes, while CTAC (surfactant with the Cl^-) is responsible for isotropic growth. Our simulations show that CTAB is able to form a compact micellar layer on the gold surface which is actually denser on Au(100) and Au(110) with respect to Au(111). The key element in the micelle adhesion to the surface is Br^- propensity for the gold surface. When Br^- is partially (eventually fully) replaced by Cl^-, the micelles prefer to diffuse into the electrolyte solution leaving the gold surface unprotected. Indeed for the CTAC system, only a few surfactant molecules are sticking to the gold surface, leaving the surface itself more easily accessible to further gold

reduction. Two sets of experiments, namely particle synthesis and plasmon shift measurements, confirm the trends expected from the simulations and agree quantitatively with the predicted values for the surfactant layer thickness.

Finally, we have investigated how the picture that we have highlighted so far is changed by the addition of silver nitrate to the solution. Considering, in first approximation, that no substantial silver reduction takes place in the growth, we have investigated the adsorption of Ag^+ on the gold surface and its impact on the structural properties of the surfactant layer. We find that silver ions have a strong propensity for the gold surface where they can form AgBr islands with different specific geometry depending on the surface plane. Although the adsorption of the surfactant micellar structure is similar to that in the absence of silver, silver substantially increases the Br^- concentration at the interface, resulting into an increased surface passivation. As in the absence of silver a lower Br^- surface density characterize the Au(111) interface when compared to the Au(100) and Au(110). Overall the asymmetry between facets is maintained in the presence of silver ions.

We believe that our work shed new light in the understanding of the microscopic structure of the nanorods/electrolyte solution, dissecting the role of the different components of the solution into the anisotropic growth. Our work paves the way to the future steps, which will include e.g. addressing the actual reaction steps to elucidate the intricate electrochemical and diffusive processes in this highly dynamical process.

A

CTAB ADSORPTION ON GOLD SURFACES

A.1 VALIDATION: MICELLE STRUCTURE IN WATER

In this section, we present the results for a simulation of a single CTAB micelle in water, which has been used as a validation for the employed force field, and as a reference for the interface calculations. We considered a test system composed by 90 CTA molecules in a simulation box of size 5.85 nm x 5.85 nm x 5.85 nm and solvated with 4991 number of water molecules. After solvation, bromide ions were added in the solution. A MD production run was performed for 100 ns after NVT and NPT equilibration. The micelle radius can be compared with that obtained by Cata and co-workers [88]. In Figure A.1, number densities of N and Br^- are represented as a function of distance from the center of micelle. The micelle radius is calculated as the distance of the maximum of the N distribution from the center of the micelle. The radius calculated using the N layer is 2.41 nm and that using the Br^- layer is 2.5 nm. The radius obtained with the N layer represents the radius of the micelle, which is in agreement to the radius of micelle from the result of Cata *et al.* for a similar system.

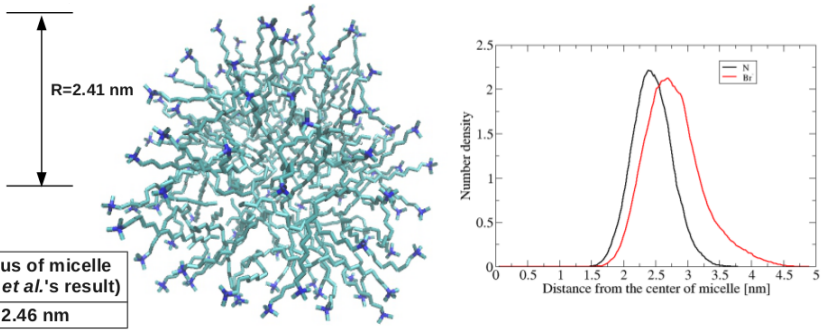

Radius of micelles (our result)	Radius of micelle (Cata *et al.*'s result)
2.41 nm	2.46 nm

Figure A.1: (a) Micelle of 1 M CTAB in water (b) Number densities of N and Br^- as a function of the distance from the center of micelle.

A.2 THICKNESS OF CTAB ON GOLD SURFACES

The density of N is reported in Figure A.2 as a function of distance from gold (111), (110) and (100) surface. The thickness of the CTAB layer is given by the distance between the gold surface and the position of the maximum number density of N close to the CTAB/water interface.

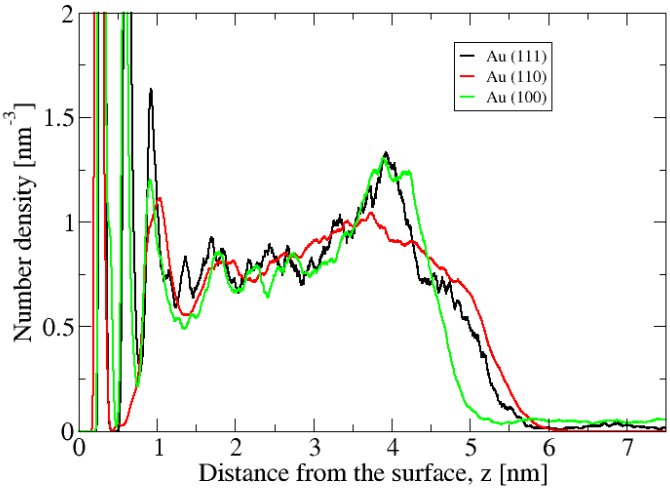

Figure A.2: Number density of N as a function of the distance from Au(111), Au(110) and Au(100) surface.

A.3 CTAB HEAD GROUPS ON GOLD SURFACES

Figure A.3 represents the integral number of CTAB head group as a function of the distance from the surface. The first plateau in each curve represents the number of head groups present in the first adsorbed layer on the gold surface. Therefore, it is clear from this figure that 21.72, 24.78 and 24.61 number of head groups of CTAB are adsorbed on the Au(111), Au(110) and Au(100) surface respectively.

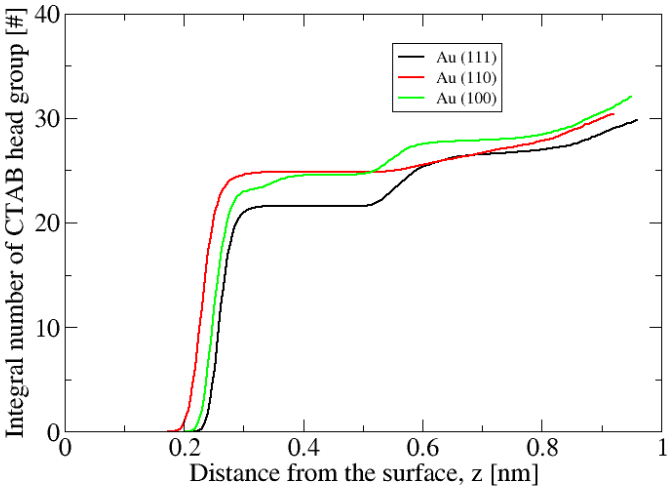

Figure A.3: Integral numbers of CTAB head groups as a function of the distance from the surface.s

A.4 WATER-ION CHANNEL ON AU(110) AND AU(100) SURFACES

Figure A.4 shows that a water-ion channel is formed between two contiguous micelles on Au(110) and Au(100) surfaces.

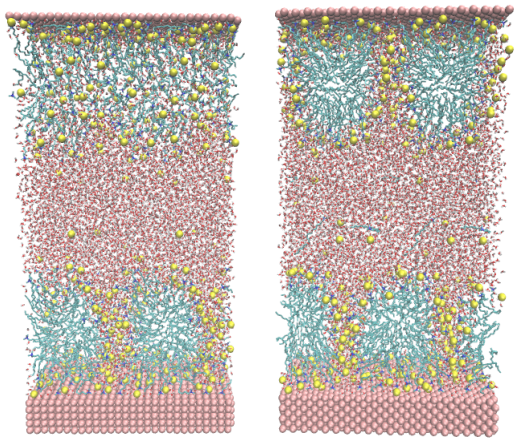

(a) (b)

Figure A.4: Snapshots from simulations of (a) Au(110) and (b) Au(100) surfaces with CTAB in water, periodic in horizontal x- direction and shows water-ion channel.

B

HIGHER INDEX FACETS AND NANOPARTICLES

B.1 SURFACE DENSITIES ON HIGHER INDEX FACETS

Table B.1 shows the surface densities of CTA^+ and Br^- calculated using different cut-offs and including either the first peak of the density profile or the first and second peak.

The surface density of CTA^+ calculated using the cut-off based on the first peak of density profile (0.41 nm, 0.32 nm and 0.35 nm for Au(250), Au(130) and Au(5120), respectively) is similar for Au(250), Au(130) and Au(5120). However, the surface density of Br^- is higher on Au(250) and Au(5120) than on Au(130).

The surface density based on the cut-off, which also includes the second layer (up the distance 0.65 nm, 0.64 nm and 0.66 for Au(250), Au(130) and Au(5120) respectively) is higher on Au(5120) than on Au(130). The surface density of Br^- based on the second cut-off definition is higher on Au(250) and Au(5120) than Au(130).

Table B.1: Surface density of CTA^+ and Br^- on different gold surfaces calculated using different cut-off based on the first density peak and including the first and seconddensity peaks.

Surface	Au(250)	Au(130)	Au(5120)	cut-off [nm]
CTA^+	1.16	1.18	1.16	0.41, 0.32, 0.35 (first density peak)
CTA^+	1.47	1.56	1.66	0.65, 0.64, 0.66 (up to second layer)
Br^-	1.44	1.36	1.52	0.34, 0.32, 0.37 (second density peak)
Br^-	1.63	1.55	1.74	0.56, 0.56, 0.69 (up to second layer)

B.2 CALCULATION OF THE SURFACE DENSITY ON NANOPARTICLES FACETS

The surface densities on the cuboctahedral seed, the penta-twinned seed and the nanorod were calculated as the number of ions present on the gold surface per unit area up to a 0.55 nm distance from the gold surface for CTA^+ and up to a 0.43 nm distance for Br^-. This is the same criteria as used for the planar surfaces. For the cuboctahedron, every facet of the cuboctahedron was cut out including the surfactant, ions and solvent molecules as shown in the Figure B.1 and the number of ions per unit area were calculated up to the cut-off distance.

On the lateral facets of penta-twinned seed particle, the surface density was evaluated by calculating the number of ions per unit area between the lateral surface and on outer pentagonal surface located at the cut-off distance (black line in Figure B.1b top view). The surface density on the tip was calculated using the number of ions between surface parallel to the tip at the cut-off distance (surface position is represented by the solid black line in Figure B.1b side view) and the surface of the tip.

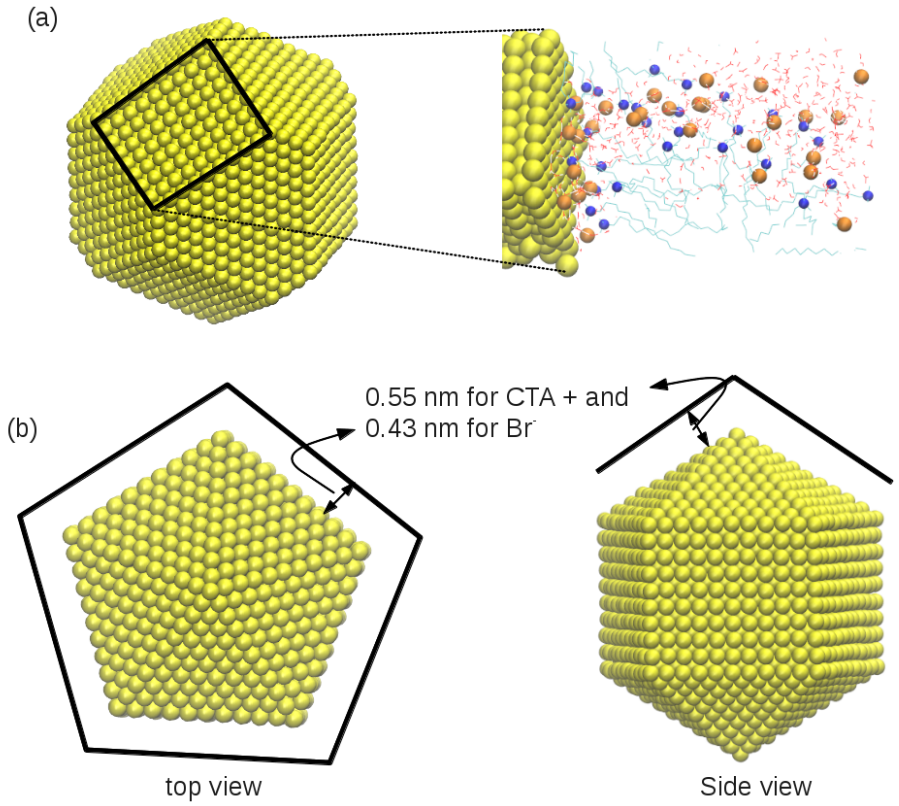

Figure B.1: Snapshots of (a) cuboctahedral nanoseed and one of it's facets is shown with the surfactant and solvent molecules. (b) Top and side view of penta-twinned nanoseed with a representation of the cut-off for the surface density calculations.

C

HALIDES ON GOLD SURFACES

C.1 HALIDE IONS AT THE AU(111)/WATER INTERFACE

We have investigated the adsorption of halides for the 1.81 M, 3.87 M and 7.78 M solutions on Au(111) (as per the models in Table 1 in the chapter 5).

Figure C.1 shows normalized ion density (number density) profiles for water and ions along with the integral number of ions as a function of the distance from the Au(111) surface for 1.81 M NaCl (Figure C.1a), NaBr (Figure C.1b) and NaI (Figure C.1c) systems. Let's first discuss the water behaviour at the gold/water interface. The red curve in Figure C.1 represents the water density profile close to the Au(111) surface, which shows that for all the three halides, water adsorbs as the first layer on the gold surface.

Table C.1: Surface densities (packing densities) of Br^- and I^- on Au(111) surface. The maximum standard error in the surface densities is 0.043 ions/nm^2.

Name of halide	[ions/nm^2] 1.81 M	[ions/nm^2] 3.87 M	[ions/nm^2] 7.78 M
Cl^-	0.26	-	0.25
Br^-	2.06	2.93	3.66
I^-	2.07	3.38	3.61

Figure C.1a shows that Cl^- ions do not adsorb on the Au(111) surface (or in the subsequent layer) and remain diffused in the solution. On the other hand Figure C.1b shows that Br^- ions adsorb on Au(111) surface and form two layers next to the water layer (two peaks near the Au(111) surface, although number density in the first layer is larger than the second layer). Iodide ions also adsorb in the form of two layers (Figure C.1c).

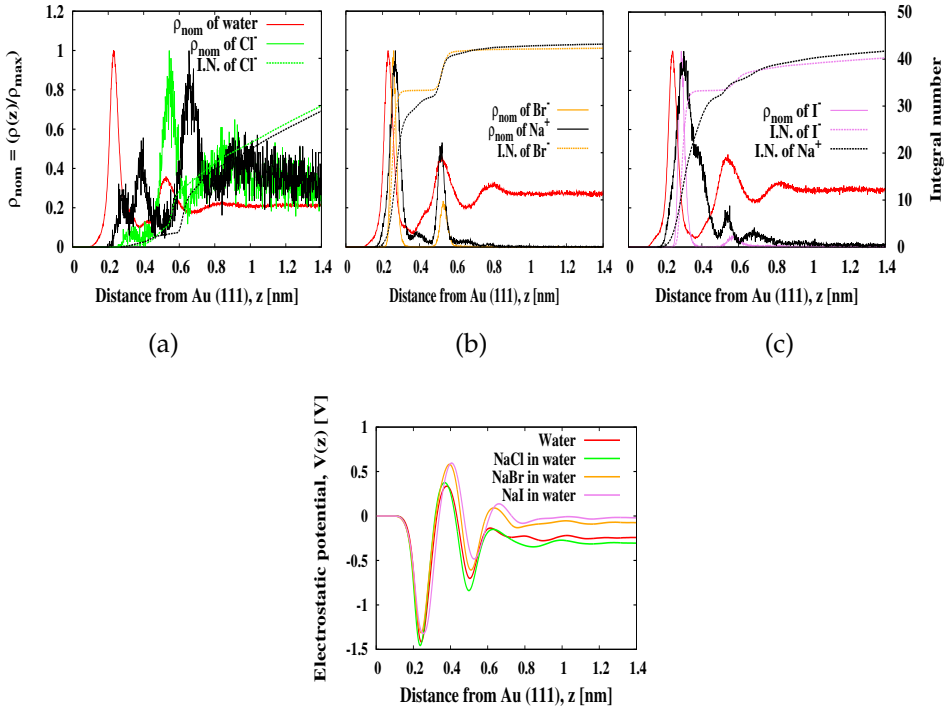

Figure C.1: Normalized ion densities (number densities) of water and ions and integral numbers of ions as a function of the distance from Au(111) surface for (a) Nacl (ρ_{max} for water = 420, Cl^- = 3.38, Na^+ = 3), (b) NaBr (ρ_{max} for water = 339.46, Br^- = 62.26, Na^+ = 29.60) and (c) NaI (ρ_{max} for water = 318.14, I^- = 58.56, Na^+ = 17.66) in water. (d) Electrostatic potentials as a function of the distance from Au(111) surface for pure water, 1.81 Nacl in water, 1.81 M NaBr and 1.81 NaI in water.

Table C.2: Electrostatic potential difference between Au(111) and the bulk water for halide ions. The maximum standard error in the potential difference is 0.012 V.

Name of system	1.81 M	3.87 M	7.78 M
Pure water	0.24	-	-
NaCl in water	0.31	-	0.27
NaBr in water	0.09	0.05	-0.11
NaI in water	0.02	-0.04	0.03

There are some interesting differences in the position of the adsorbed halide layers. In particular, the first water layer adsorbed on the Au(111) surface is at 0.23 nm, the first Na^+ layer is at 0.28 nm and the Cl^- ions layer is at 0.33 nm for NaCl solution (Figure C.1a). In the case of the NaBr solution, the first water layer adsorbed on the Au(111) surface is also at 0.23 nm, the first Br^- layer is at 0.26 nm and the Na^+ layer is at 0.27 nm (Figure C.1b). Finally for the NaI solution the first water layer adsorbed on the Au(111) surface is at 0.24 nm, the first I^- layer is at 0.29 nm and the Na^+ layer is at 0.30 nm.

The likelihood to find the halides on the gold surface can also be expressed in terms of packing density which is calculated as the integral number of ions in the first layer divided by surface area, and which represents the number of ions adsorbed per nm^2 on the gold surface (Table C.1). The number of ions in the first layer are calculated from the integral number in the first layer (see dotted lines in Figure C.1a, C.1b, C.1c) From our simulation, we can evince that Cl^- has a very low propensity for the gold surface, while both Br^- and I^- show a quite high propensity to adsorb on the gold surface (Table C.1). Figure C.1d shows the electrostatic potential for pure water, 1.81 M NaCl, 1.81 M NaBr and 1.81 M NaI. The potential difference between Au(111) surface and water is reported in Table C.2 for the same.

Figure C.2 and C.3 represent normalized number density profile of water and ions with integral number of ions as a function of distance from Au(111) surface for 3.87 M sodium halide (NaBr and NaI) and for 7.78 M sodium halide (NaCl, NaBr and NaI) in water. The packing densities for 3.87 M sodium halide and 7.78 M sodium halide are reported in Table C.1. The packing density of Cl^- remains the same whereas packing densities of Br^- and I^- increase with the concentration. Figure C.2c and C.3d represent the electrostatic potential as a function of distance from Au(111) surface for 3.87 M sodium halide in water and for 7.78 M sodium halide in water. The potential differences between Au(111) surface and water for 3.87 M sodium halide and for 7.78 M sodium halide aqueous solutions are also reported in Table C.2.

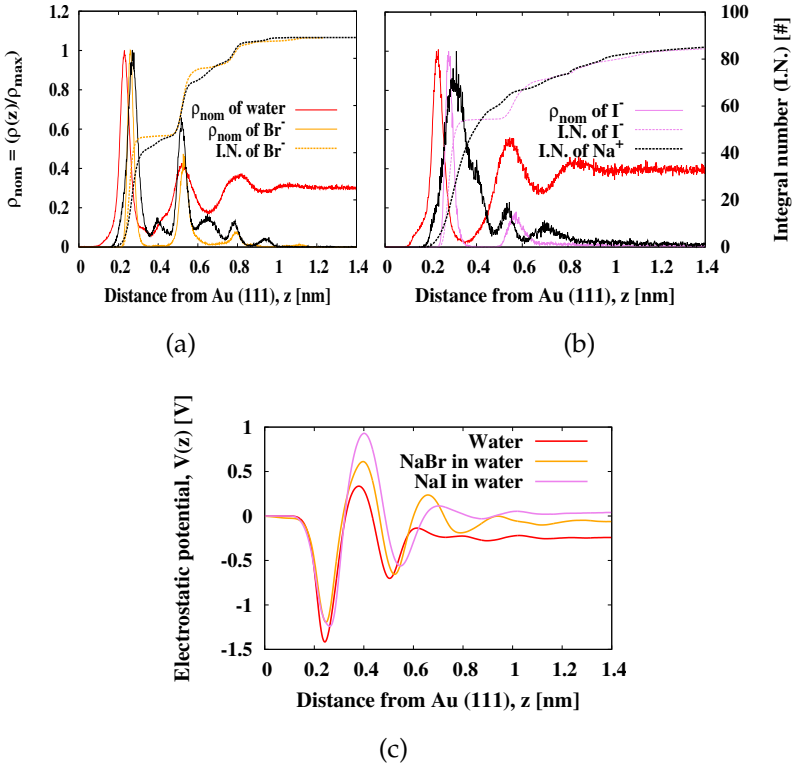

Figure C.2: Normalized ion densities (number densities) of water and ions and integral numbers of ions as a function of the distance from Au(111) surface for 3.87 M (a) NaBr (ρ_{max} for water = 296.28, Br^- = 76.16, Na^+ = 39.75) and (b) NaI (ρ_{max} for water = 231.15, I^- = 84.88, Na^+ = 32.40) in water. (c) Electrostatic potentials as a function of the distance from Au(111) surface for pure water, 3.87 M NaBr and 3.87 NaI in water.

C.2 PROPERTIES FOR DIFFERENT CTAB/CTAC SYSTEMS

The normalized number density profile of water, CTA^+ and Br^- along with the integral number of CTA^+ and Br^- near different gold surfaces (namely data for Au(111), Au(110) and Au(100)) are reported respectively in Figure C.4a, C.4b and C.4c for 100% CTAB in water.

Electrostatic potential as a function of the distance from different gold surfaces is also included and presented in Figure C.4e for 100% CTAB in water. At Au(110) a few water molecules can be adsorb in the void between gold atoms available on Au(110) surface. Also, the first peak in the density profile of Br^- ions is closer to the surface in the case of Au(110) than in the case of

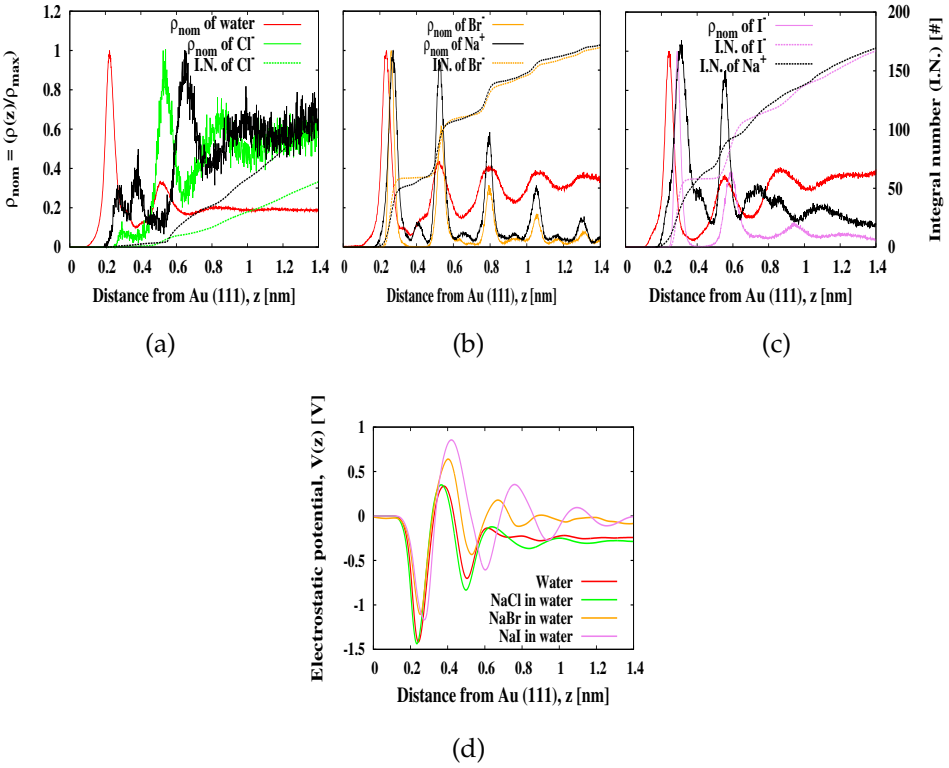

Figure C.3: Normalized ion densities (number densities) of water and ions and integral numbers of ions as a function of the distance from Au(111) surface for 7.78 M (a) NaCl (ρ_{max} for water = 136.49, Br^- = 4.64, Na^+ = 4.25), (b) NaBr (ρ_{max} for water = 249.13, Br^- = 97.63, Na^+ = 54.58) and (c) NaI (ρ_{max} for water = 198.12, I^- = 91.81, Na^+ = 34.13) in water. (d, e) Electrostatic potentials as a function of the distance from Au(111) surface for pure water, 7.78 M NaCl, 7.78 M NaBr and 7.78 M NaI in water.

Table C.3: Potential difference, ΔV, between bulk and adsorbed surfactant layer on gold surfaces.

Name of surface	Au(111)	Au(110)	Au(100)
ΔV with 100% CTAB [V]	0.86	0.83	0.82
ΔV with 50% CTAB 50% CTAC [V]	0.57	0.56	0.57
ΔV with 25% CTAB 75% CTAC [V]	0.50	0.58	0.49

Au(111) and Au(100) as Br^- can better fit on the less dense Au(110) surface. The Au(100) surface represents an intermediate situation, where some more space is available for the ion adsorption with respect to the Au(111) case but

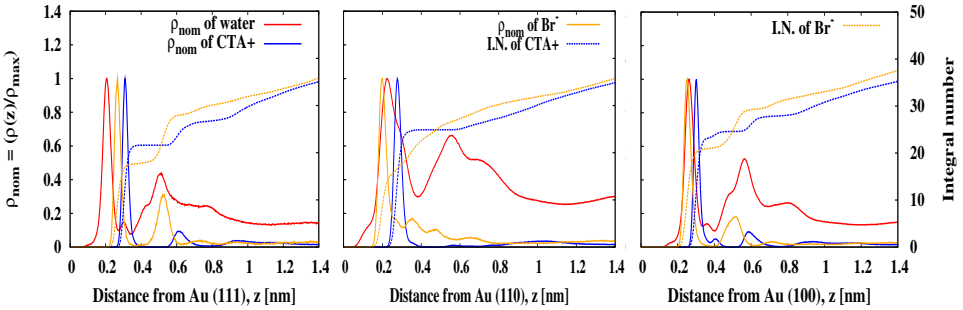

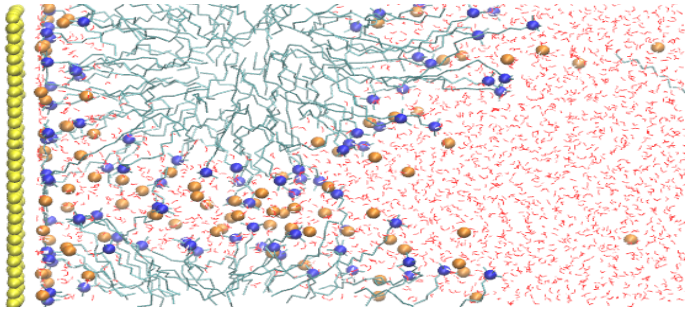

(d)

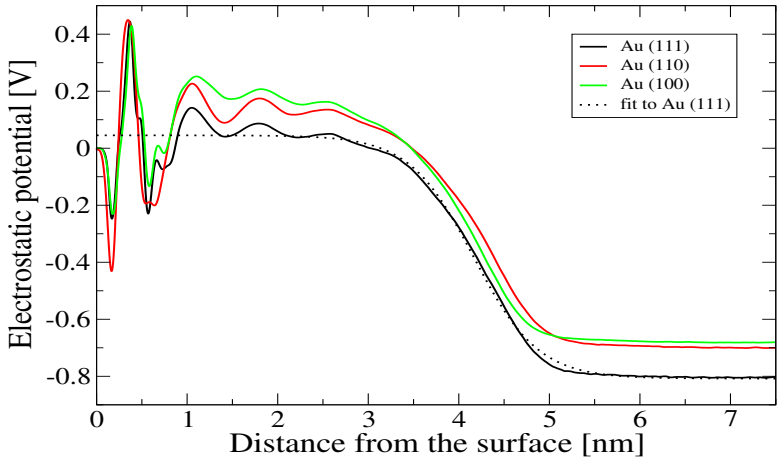

(e)

Figure C.4: Normalized ion densities (number densities) of water and ions and integral numbers of ions as a function of the distance from (a) Au(111) (ρ_{max} for water = 179.26, CTA^+ = 36.74 Br^- = 25.36), (b) Au(110) (ρ_{max} for water = 85.53, CTA^+ = 34.67, Br^- = 19.56) and (c) Au(100) (ρ_{max} for water = 170.25, CTA^+ = 37.63, Br^- = 27.76) in water. (d) Snapshot from simulations containing CTAB layer on Au(111) in water (e) Electrostatic potentials as a function of the distance from different gold surfaces for 100% CTAB in water.

less space is available with respect to the Au(110) case. Therefore, the first peak position in the Br^- density is an intermediate between that on Au(110) and that on Au(111). Finally the CTA^+ density profile (blue line in Figure C.4a, C.4b and C.4c) follows the Br^- profile and adsorb next to Br ions on the gold surfaces, although with differences.

In Figure C.5, we report the normalized density profile of water, CTA^+, Br^- and Cl^- along with integral number of CTA^+, Br^- and Cl^- close to gold surfaces (Figure C.5a, C.5b and C.5c) for 50% CTAB and 50% CTAC mixture. A snapshot from the simulation of the Au(111) interface is also reported. Finally, the electrostatic potential as a function of distance from different gold surfaces is also included. From Figure C.5a, C.5b and C.5c, we can see that the water density profile is similar to the 100% CTAB. Also, in this case, the water profile on Au(110) shows that some water molecules can be adsorbed in the void available between the gold atoms on the surface. Cl^- has very low propensity for adsorption on all the three surfaces. Indeed the first density peak of Cl^- is very small (see normalized value) or negligible as compared to the second peak. This is also clear from integral number of Cl^- which is negligible near all the gold surfaces.

As for the other cases, normalized ion density profile along with integral number of CTA^+, Br^- and Cl^- close to Au(111), Au(110) and Au(100) surfaces after 800 ns (Figure C.6a, C.6b and C.6c, respectively) are reported for a 25% CTAB 75% CTAC mixture. A snapshot from the simulation of the Au(111) interface and the electrostatic potential as function of the distance from different gold surfaces are reported in Figure C.6d and Figure C.6e respectively.

Figure C.7 shows the normalized ion density profile of water, CTA^+ and Cl^- along with the integral number of CTA^+ and Cl^- near gold surfaces, a snapshot from the simulation of CTAC layer in water on Au(111) surface and the electrostatic potential as a function of distance from the different gold surfaces for 100% CTAC in water. The integral number curves of CTA^+ for Au(111), Au(110) and Au(100) show that about 30 surfactant molecules are adsorbed on the Au(111) (namely 11 molecules in the first layer and 19

Table C.4: Average thickness of surfactant layer on different gold surfaces with different concentration of CTAB/CTAC. The maximum standard error in the layer thickness is 0.047 nm.

Name of surface	Au(111)	Au(110)	Au(100) [nm]
100% CTAB	3.86	3.74	3.85
50% CTAB 50% CTAC	5.87	6.10	5.98
25% CTAB 75% CTAC	5.97	6.03	6.05
100% CTAC	1.80	2.40	1.80

molecules in the second layer) about 40 surfactant molecules are adsorbed on Au(110) (11 molecules in the first layer and 29 molecules after first layer) and 24 surfactant molecules adsorb on the Au(100) (namely 11 molecules in the first layer and 13 molecules in the second layer). The detached micelles from Au(111), Au(110) and Au(100) consists of about 60, 50 and 66 surfactant molecules respectively.

Figure C.8 and Table C.4 show that the thickness of the surfactant layer increases with the concentration of CTAC surfactant. Therefore compactness of the surfactant layer on all the gold surfaces decreases with an increase in the concentration of CTAC surfactant in the solution.

C.3 CONVERSION OF PLASMON SHIFT TO LAYER THICKNESS

To interpret the experimental determined resonance shift $\Delta\lambda_{res}$, i.e. converting the plasmon shifts to a change in layer thickness, we use equations and parameters determined solving the Maxwell equations using published bulk dielectric functions for the materials. The Maxwell equations were solved numerically using the Boundary Element Method (BEM). To a good approximation, the plasmon shift for gold nanorods induced by an adsorption layer

with refractive index Δn higher than the surrounding medium and thickness t, is given by [123]:

$$\Delta\lambda = S\Delta n(1 - e^{\frac{-t}{d_{sens}}}). \tag{C.1}$$

In this equation, S is the sensitivity $S = \Delta\lambda_{res}/\Delta n$ and d_{sens} the sensing distance, i.e. the distance at which a layer causes $(1 - \frac{1}{e})$ of the maximum shift. The sensitivity S depends on the particles. For the particles we used here, the sensitivity was determined experimentally as S = 143.1 nm/RIU [107]. From a large set of simulations, we have found that the sensing distance d_{sens} is well approximated as:

$$d_{sens} = 0.37V^{(\frac{1}{3})}. \tag{C.2}$$

where V is the nanorod's volume [124]. Our particles had a length of a = (67.8±9.2) nm and a width b = (31.1±5.6) nm [107]. With these parameters, we calculated the plasmon shift $\Delta\lambda_{res}$ as a function of layer thickness t and its refractive index (Figure C.11). The data shown in Figure C.11 allows us to convert the measured shifts in plasmon resonance wavelength to a change in layer thickness using a refractive index of the surfactants CTAB of $n = 1.4$ [113], [114] and assuming the same refractive index for CTAC. These conversions result in a layer thickness of 1.6 nm for CTAC and 4.2 nm for CTAB, in good agreement with the results from the molecular dynamics simulations.

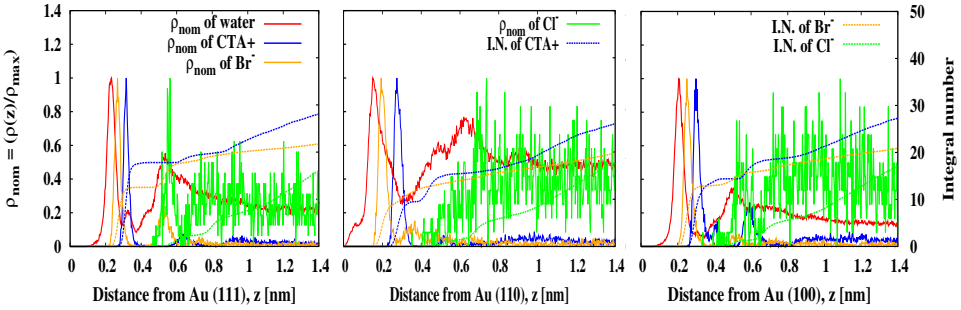

(a) (b) (c)

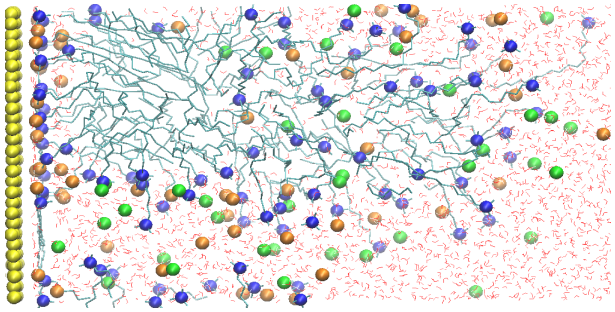

(d)

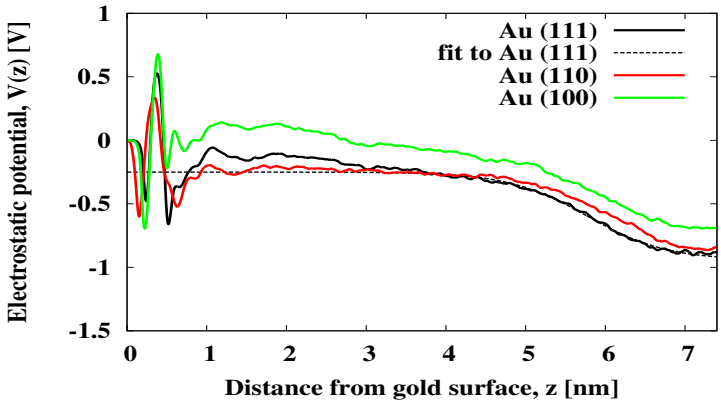

(e)

Figure C.5: Normalized number densities (ion density) of water and ions and integral number of ions as a function of the distance from (a) Au(111) (ρ_{max} for water = 183.61, CTA^+ = 35.19, Br^- = 22.32, Cl^- =1.57), (b) Au(110) (ρ_{max} for water = 103.73, CTA^+ = 22.00, Br^- = 15.83, Cl^- = 1.16) and (c) Au(100) (ρ_{max} for water = 297.46, CTA^+ = 19.24, Br^- = 22.20, Cl^- = 0.88) in water. (d) Snapshot from simulations containing 50% CTAB 50% CTAC layer on Au(111) in water. (e) Electrostatic potentials as a function of the distance from different gold surfaces for 50% CTAB and 50% CTAC mixture in water

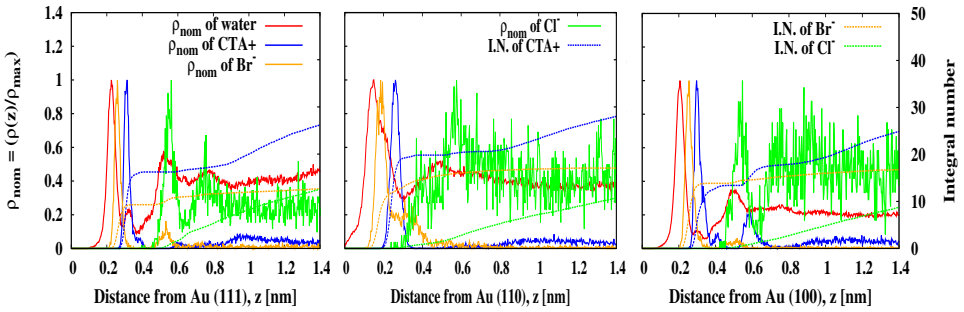

(a) (b) (c)

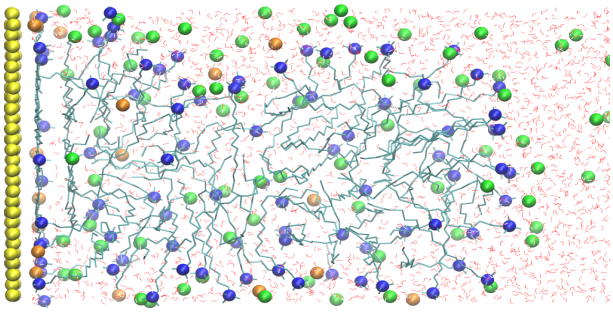

(d)

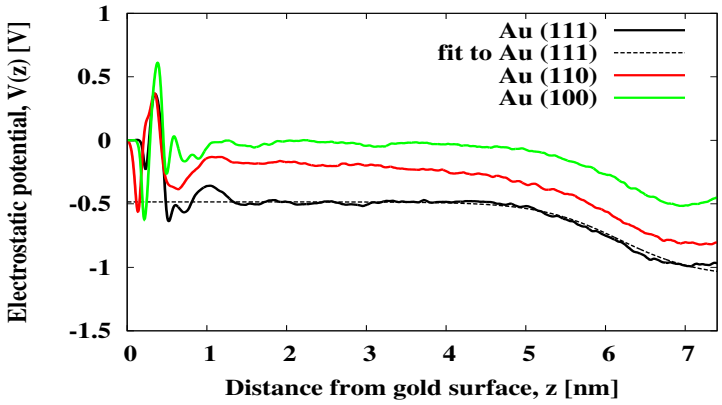

(e)

Figure C.6: Normalized ion density (number density) of water and ions and integral number of ions as a function of the distance from (a) Au(111), (ρ_{max} for water = 114.10, CTA^+ = 21.42, Br^- = 12.20, Cl^- = 3.03) (b) Au(110) (ρ_{max} for water = 123.82, CTA^+ = 20.00, Br^- = 10.00, Cl^- = 1.47) (c) Au(100) (ρ_{max} for water = 255.79, CTA^+ = 17.57, Br^- = 18.03, Cl^- = 1.36) in water. (d) Snapshot from simulations containing 25% CTAB 75% CTAC layer on Au(111) in water. (e) Electrostatic potentials as a function of the distance from different gold surface for 25% CTAB and 75% CTAC mixture in water.

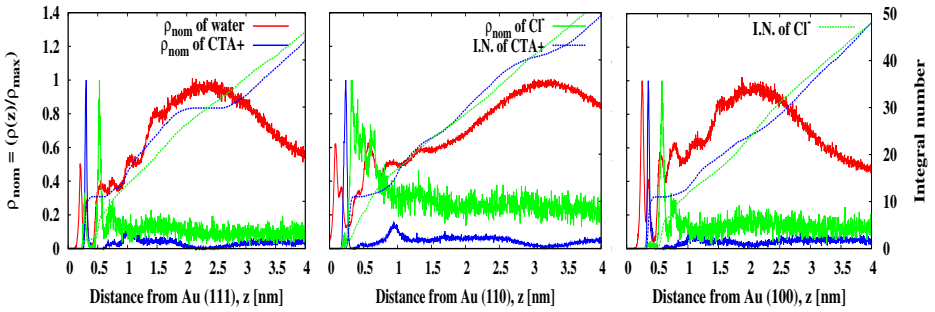

(a) (b) (c)

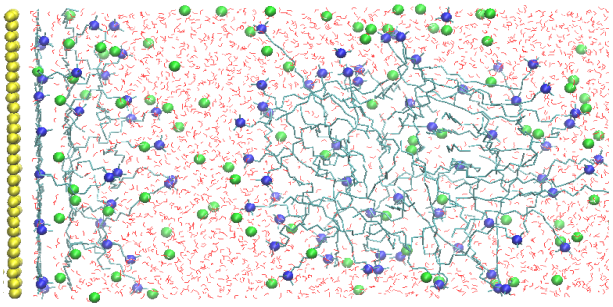

(d)

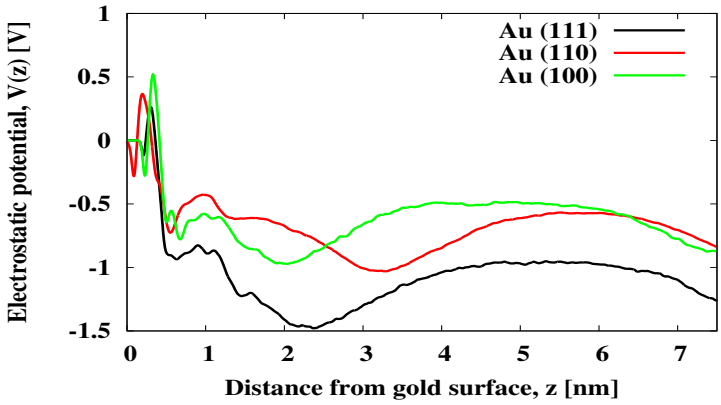

(e)

Figure C.7: Normalized ion densities (number densities) of water and ions and integral number of ions as a function of the distance from (a) Au(111) (ρ_{max} for water = 110.90, CTA^+ = 18.20 Cl^- = 6.36), (b) Au(110) (ρ_{max} for water = 110.9, CTA^+ = 12.13, Cl^- = 2.47) and (c) Au(100) (ρ_{max} for water = 102.96, CTA^+ = 15.24, Cl^- = 5.50) in water. (d) Snapshot from simulations containing CTAC layer on Au(111) in water (e) Electrostatic potentials as a function of the distance from different gold surfaces for 100% CTAC in water.

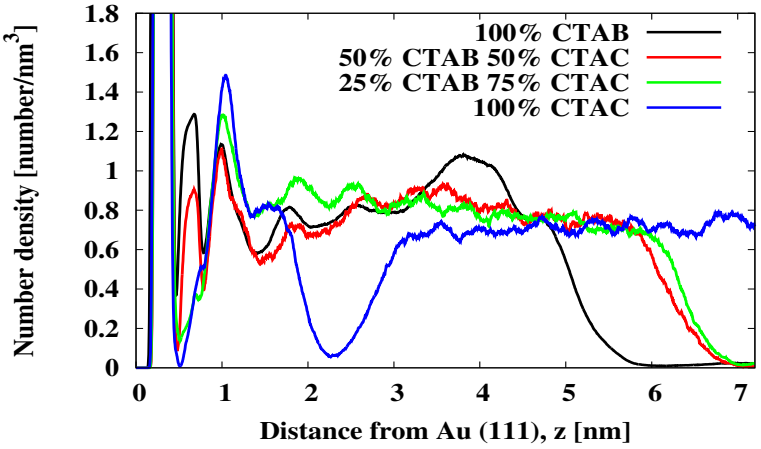

(a)

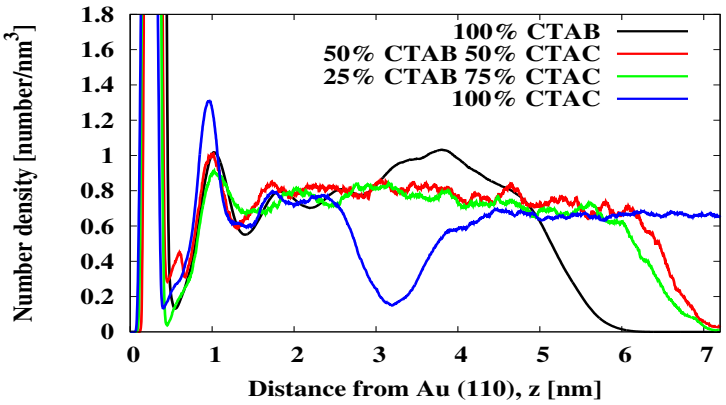

(b)

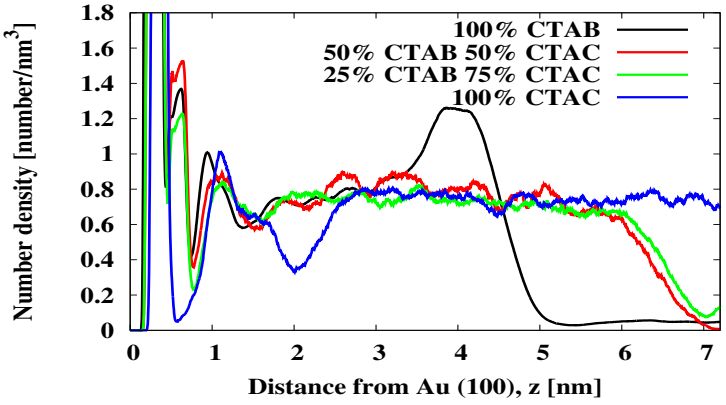

(c)

Figure C.8: Averaged ion density (number density) of CTA^+ as a function of the distance from (a) Au(111), (b) Au(110) and (c) Au(100) surfaces for 100% CTAB, 50% CTAB and 50% CTAC, 25% CTAB and 75% CTAC and 100% CTAC systems

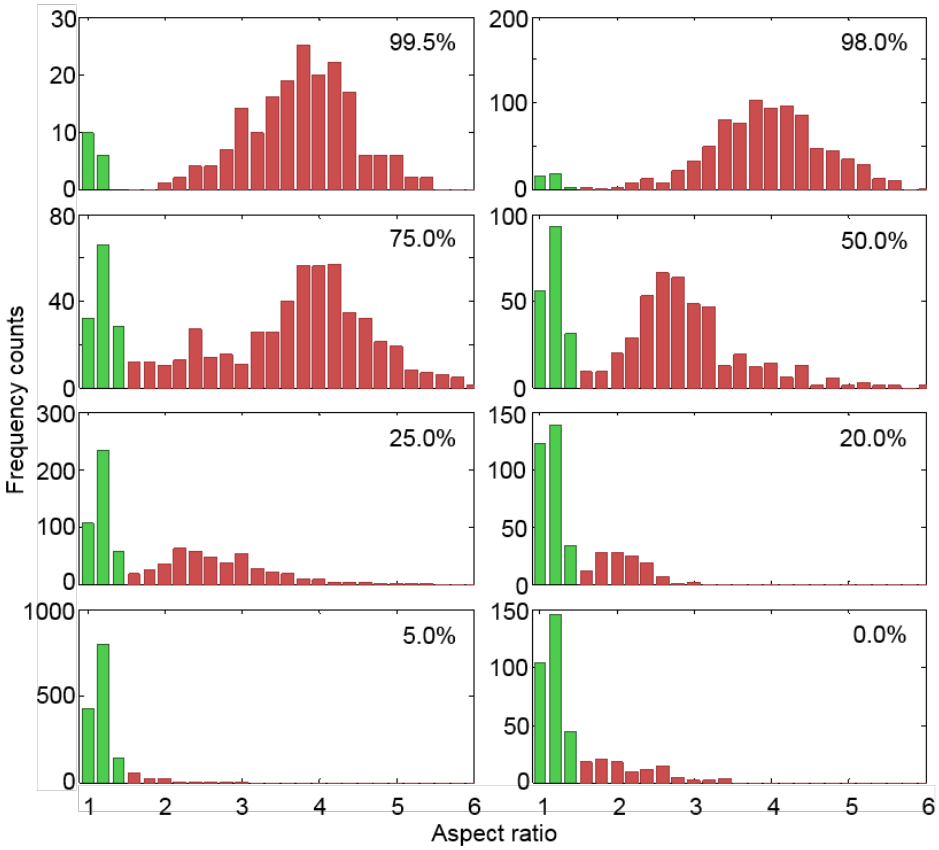

Figure C.9: Histogram of particle dimensions determined from TEM images of the nanoparticles produced with different ratios of CTAB and CTAC, given in percentage of CTAB (upper right corner). To distinguish spherical (green) and rodshaped particles (red), we used a cutoff value of 1.5. The ratio of spheres to rods is described in chapter 5.

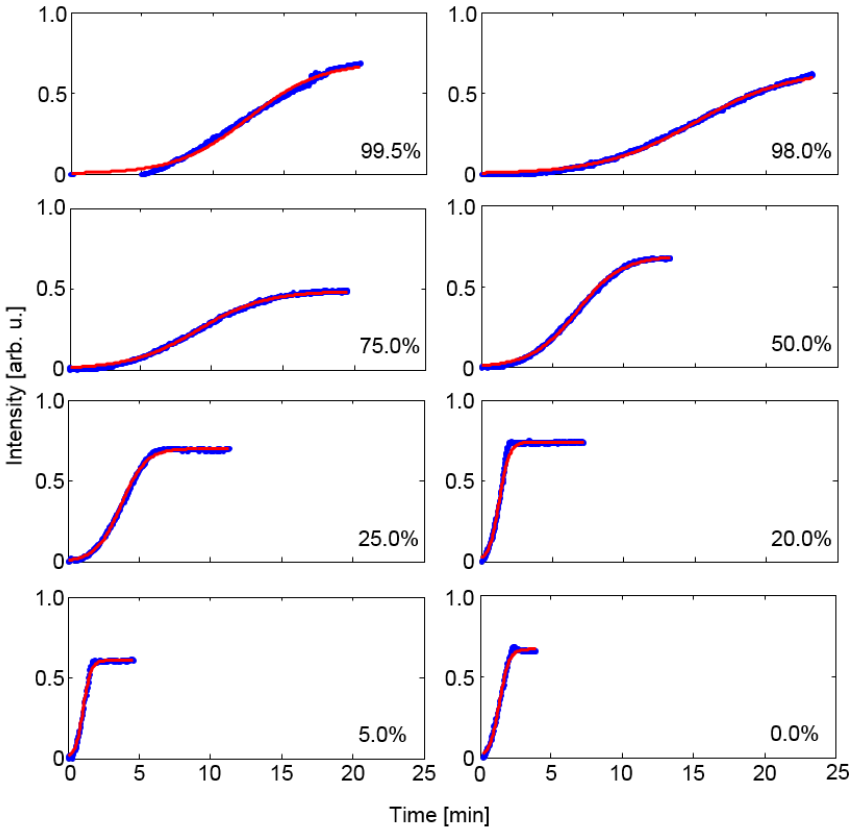

Figure C.10: Growth kinetics extracted from the absorbance spectrum in the interband region at 450 nm as a function of time for growth solutions with different CTAB to CTAC ratios, given in percentages of CTAB. The experimental data (blue dots) has been fitted with a Boltzmann function (solid red line) to extract the reaction rate constants for each solution. The figure shows an increasing trend of the reaction speed when the percentage of CTAB is decreasing (as predicted by simulation).

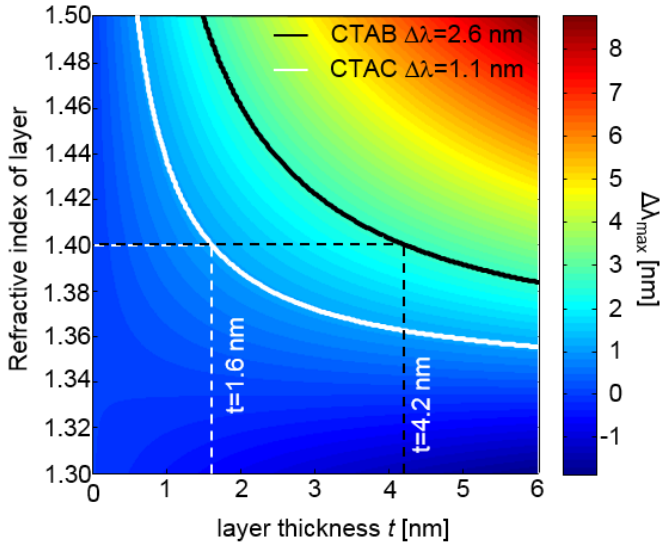

Figure C.11: Calculated resonance shift $\Delta\lambda_{res}$, for different values of layer thickness and refractive index. Solid black and white lines show contours for experimentally determined resonance shifts of CTAB and CTAC layers. Dotted black and white lines represent the conversion from resonance shift to layer thickness of CTAB and CTAC using published values for the refractive index of CTAB (n=1.4) [113], [114].

BIBLIOGRAPHY

[1] A. M. Alkilany, L. B. Thompson, S. P. Boulis, P. N. Sisco, and C. J. Murphy, "Gold nanorods: Their potential for photothermal therapeutics and drug delivery, tempered by the complexity of their biological interactions.," *Adv. Drug Deliv. Rev.*, vol. 64, pp. 190–199, 2012.

[2] L. M. Liz-Marzan, "Tailoring surface plasmons through the morphology and assembly of metal nanoparticles.," *Langmuir*, vol. 22 (1), pp. 32–41, 2006.

[3] X. H. Huang, P. K. Jain, I. H. El-sayed, and M. A. El-Sayed, "Gold nanoparticles: Interesting optical properties and recent applications in cancer diagnostics and therapy.," *Nanomedicine*, vol. 2, pp. 681–693, 2007.

[4] H. Kuwata, H. Tamaru, K. Esumi, and K. Miyano, "Resonant light scattering from metal nanoparticles: Practical analysis beyond rayleigh approximation.," *Appl. Phys. Lett.*, vol. 83, pp. 4625–4627, 2003.

[5] S. Prescott and P. Mulvaney, "Gold nanorod extinction spectra.," *J. Appl. Phys.*, vol. 99, p. 123 504, 2006.

[6] S. Link, M. Mohamed, and M. El-Sayed, "Simulation of the optical absorption spectra of gold nanorods as a function of their aspect ratio and the effect of the medium dielectric constant.," *J. Phys. Chem. B*, vol. 103, pp. 3073–3077, 1999.

[7] D. Pissuwan, S. M. Valenzuela, and M. B. Cortie, "Therapeutic possibilities ofplasmonically heated goldnanoparticles.," *Trends Biotechnol.*, vol. 24, pp. 62–67, 2006.

[8] M. Valden, X. Lai, and D. W. Goodman, "Onset of catalytic activity of gold clusters on titania with the appearance of nonmetallic properties.," *Science*, vol. 281, pp. 1647–1650, 1998.

[9] C. T. Campbell, S. C. Parker, and D. E. Starr, "The effect of size-dependent nanoparticle energetics on catalyst sintering.," *Science*, vol. 298, pp. 811–814, 2002.

[10] Z. Adriano, E. Groppo, and S. Bordiga, "Selective catalysis and nanoscience: an inseparable pair.," *Chem. Eur. J.*, vol. 13, pp. 2440–2460, 2007.

[11] R. Narayanan and M. a. El-Sayed, "Catalysis with transition metal nanoparticles in colloidal solution: nanoparticle shape dependence and stability.," *J. Phys. Chem. B*, vol. 109, no. 26, pp. 12 663–12 676, 2005.

[12] N. R. Jana, L. Gearheart, and C. J. Murphy, "Wet chemical synthesis of high aspect ratio cylindrical gold nanorods.," *J. Phys. Chem. B.*, vol. 105, pp. 4065–4067, 2001.

[13] B. Nikoobakht and M. A. El-Sayed, "Preparation and growth mechanism of gold nanorods (nrs) using seed-mediated growth method.," *Chem. Mater.*, vol. 15 (10), pp. 1957–1962, 2003.

[14] C. J. Murphy, T. K. Sau, A. M. Gole, C. J. Orendorff, J. Gao, L. Gou, S. E. Hunyadi, and T. Li, "Anisotropic metal nanoparticles: Synthesis, assembly, and optical applications.," *J. Phys. Chem. B.*, vol. 109 (29), pp. 13 857–13 870, 2005.

[15] Y. Xia, Y. Xiong, B. Lim, and S. Skrabalak, "Shape-controlled synthesis of metal nanocrystals: Simple chemistry meets complex physics?.," *Angw. Chem. Int. Ed.*, vol. 48, pp. 60–103, 2009.

[16] J. Pérez-Juste, L. Liz-Marzan, S. Carnie, D. Chan, and P. Mulvaney, "Electric-field-directed growth of gold nanorods in aqueous surfactant solutions.," *Adv. Funct. Mater.*, vol. 14(6), pp. 571–579, 2004.

[17] V. Sebastian, S.-K. Lee, C. Zhou, M. F. Kraus, J. G. Fujimoto, and K. F. Jensen, "One-step continuous synthesis of biocompatible gold nanorods for optical coherence tomography.," *Chem. Commun.*, vol. 48, pp. 6654–6656, 2012.

[18] D. K. Smith and B. A. Korgel, "The importance of the ctab surfactant on the colloidal seed-mediated synthesis of gold nanorods.," *Langmuir*, vol. 24, pp. 644–649, 2008.

[19] W. Cheng, S. Dong, and E. Wang, "Iodine-induced gold-nanoparticle fusion/fragmentation/aggregation and iodine-linked nanostructured assemblies on a glass substrate.," *Angew. Chem. Int. Ed.*, vol. 42, pp. 449–452, 2003.

[20] T. H. Ha, H.-J. Koo, and B. H. Chung, "Shape-controlled syntheses of gold nanoprisms and nanorods influenced by specific adsorption of halide ions.," *J. Phys. Chem. C*, vol. 111, pp. 1123–1130, 2007.

[21] J. E. Millstone, W. Wei, M. R. Jones, H. Yoo, and C. A. Mirkin, "Iodide ions control seed-mediated growth of anisotropic gold nanoparticles.," *Nano Lett.*, vol. 8 (8), pp. 2526–2529, 2008.

[22] M. Grzelczak, A. Sanchez-Iglesias, B. Rodriguez-Gonzalez, R. Alvarez-Puebla, J. Pérez-Juste, and L. M. Liz-Marzán, "Influence of iodide ions on the growth of gold nanorods: Tuning tip curvature and surface plasmon resonance.," *Adv. Funct. Mater.*, vol. 18, pp. 3780–3786, 2008.

[23] D. K. Smith, N. R. Miller, and B. A. Korgel, "Iodide in CTAB prevents gold nanorod formation.," *Langmuir*, vol. 25(16), pp. 9518–9524, 2009.

[24] T. Soejima and N. Kimizuka, "One-pot room-temperature synthesis of single-crystalline gold nanocorolla in water.," *J. Am. Chem. Soc.*, vol. 131, pp. 14 407–14 412, 2009.

[25] X. Fan, Z. R. Guo, J. M. Hong, Y. Zhang, J. N. Zhang, and N. Gu, "Size-controlled growth of colloidal gold nanoplates and their high-purity acquisition.," *Nanotechnology*, vol. 21, pp. 105 602–105 609, 2010.

[26] J. Zhang, M. R. Langille, M. L. Personick, K. Zhang, S. Li, and C. A. Mirkin, "Concave cubic gold nanocrystals with high-index facets.," *J. Am. Chem. Soc.*, vol. 132 (40), pp. 14 012–14 014, 2010.

[27] Z. Jiao, H. Xia, and X. Tao, "Modulation of localized surface plasmon resonance of nanostructured gold crystals by tuning their tip curvature with assistance of iodide and silver(i) ions.," *J. Phys. Chem. C*, vol. 115 (16), pp. 7887–7895, 2011.

[28] J. S. DuChene, W. Niu, J. M. Abendroth, Q. Sun, W. Zhao, F. Huo, and W. D. Wei, "Halide anions as shape-directing agent for obtaining high-quality anisotropic gold nanostructures.," *Chem. Mater.*, vol. 25, pp. 1392–1399, 2013.

[29] M. R. Langille, M. L. Personick, J. Zhangand, and C. A. Mirkin, "Defining rules for the shape evolution of gold nanoparticles.," *J. Am. Chem. Soc.*, vol. 134, pp. 14 542–14 554, 2012.

[30] M. G. A. da Silva, M. R. Meneghetti, A. Denicourt-Nowicki, and A. Roucoux, "Tunable hydroxylated surfactants: An efficient toolbox towards anisotropic gold nanoparticles.," *RSC Adv.*, vol. 4, pp. 25 875–25 879, 2014.

[31] A. Kedia and P. S. Kumar, "Halide ion induced tuning and self-organization of gold nanostars.," *RSC Adv.*, vol. 4, pp. 4782–4790, 2014.

[32] T. K. Sau and C. J. Murphy, "Role of ions in the colloidal synthesis of gold nanowires.," *Philos. Mag.*, vol. 87, pp. 14–15, 2007.

[33] S. E. Lohse, N. D. Burrows, L. Scarabelli, L. M. Liz-Marzán, and C. J. Murphy, "Anisotropic noble metal nanocrystal growth: The role of halides.," *Chem. Mater.*, vol. 26(1), pp. 34–43, 2014.

[34] M. Grzelczak, J. Pérez-Juste, P. Mulvaney, and L. M. Liz-Marzán, "Shape control in gold nanoparticle synthesis.," *Chem. Soc. Rev.*, vol. 37, pp. 1783–1791, 2008.

[35] S. E. Lohse and C. J. Murphy, "The quest for shape control: A history of gold nanorod synthesis.," *Chem. Mater.*, vol. 25 (8), pp. 1250–1261, 2013.

[36] Y. Xia, X. Xia, and H. C. Peng, "Shape-controlled synthesis of colloidal metal nanocrystals: thermodynamic versus kinetic products.," *J. Am. Chem. Soc.*, p. 150 528 140 910 003, 2015.

[37] G. Z. Wulff, *Z. Kristallogr. Mineral.*, vol. 34, pp. 449–530, 1901.

[38] C. Herring, "Some theorems on the free energies of crystal surfaces.," *Phys. Rev.*, vol. 82, pp. 87–93, 1951.

[39] C. R. Henry, "Morphology of supported nanoparticles.," *Prog. Surf. Sci.*, vol. 80, pp. 92–116, 2005.

[40] M. G. T. Burrows and W. H. Stockmayer, "The poisoning of a palladium catalyst by carbon monoxide.," *Surf. Sci.*, vol. 176, pp. 471–483, 1940.

[41] G. Ertl and P. Rau, "Chemisorption und katalytische reaktion von sauerstoff und kohlenmonoxid an einer palladium (110)-oberflache.," *Surf. Sci.*, vol. 15, pp. 443–465, 1969.

[42] A.-C. Shi and R. Masel, "The effects of gas adsorption on particle shapes in supported platinum catalysts.," *Surf. Sci.*, vol. 120, pp. 421–431, 1989.

[43] M. Roberts, "Chemisorption and reactions at metal surfaces.," *Surf. Sci.*, vol. 299, pp. 769–784, 1994.

[44] Q. Chen and N. V. Richardson, "Chemisorption and reactions at metal surfaces.," *Prog. Surf. Sci.*, vol. 73, pp. 59–77, 2003.

[45] B. Nikoobakht and M. A. El-Sayed, "Evidence for bilayer assembly of cationic surfactants on the surface of gold nanorods.," *Langmuir*, vol. 17, pp. 6368–6374, 2001.

[46] C. J. Johnson, E. Dujardin, S. A. Davis, C. J. Murphy, and S. Mann, "Growth and form of gold nanrods prepared by seed-mediated.," *J. Mater. Chem.*, vol. 12, pp. 1765–1770, 2002.

[47] C Lofton and W Sigmund, "Mechanisms controlling crystal habits of gold and silver colloids.," *Adv. Funct. Mat.*, vol. 15 (7), pp. 1197–1208, 2005.

[48] C. J. Johnson, E. Dujardin, S. A. Davis, C. J. Murphy, and S. Mann, "Growth and form of gold nanorods prepared by seed-mediated, surfactant-directed synthesis.," *J. Mater. Chem.*, vol. 12, no. 6, pp. 1765–1770, 2002.

[49] J. X. Gao, C. M. Bender, and C. J. Murphy, "Dependence of gold nanorod aspect ratio on the nature of the directing surfactant in aqueous solution.," *Langmuir*, vol. 19 (21), pp. 9065–9070, 2003.

[50] A. Henkel, O. Schubert, A. Plech, and C. Sonnichen, "Growth kinetic of a rod-shaped metal nanocrystal.," *J. Phys. Chem. C*, vol. 113, pp. 10 390–10 394, 2009.

[51] T. Pal, S. De, N. R. Jana, N. Pradhan, R. Mandal, and A. Pal, "Organized media as redox catalysts.," *Langmuir*, vol. 14(17), pp. 4724–4730, 1998.

[52] E. Carbo-Argibay, B. Rodriguez-Gonzalez, S. Gomez-Grana, A. G. Martinez, I. Pastoriza-Santos, J. Perez-Juste, and L. M. Liz-Marzan, "The crystalline structure of gold nanorods revisited: Evidence for higher-index lateral facets.," *Angew. Chem. Int. Ed.*, vol. 49, pp. 9397–9400, 2010.

[53] K. Park, L. F. Drummy, R. C. Wadams, H. Koerner, D. Nepal, L. Fabris, and R. A. Vaia, "Growth mechanism of gold nanorods.," *Chem. Mater.*, vol. 25 (4), pp. 555–563, 2013.

[54] H. Katz-Boon, C. J. Rossouw, M. Weyland, A. M. Funston, P. Mulvaney, and J. Etheridge, "Three-dimensional morphology and crystallography of gold nanorods.," *Nano Lett.*, vol. 11(1), pp. 273–278, 2011.

[55] A. S. Barnard, "Modelling of nanoparticles: Approaches to morphology and evolution.," *Rep. Prog. Phys.*, vol. 73, p. 086 502, 2010.

[56] A. Seyed-Razavi, I. K. Snook, and A. S. Barnard, "Surface area limited model for predicting anisotropic coarsening of faceted nanoparticles.," *Cryst. Growth Des.*, vol. 11(1), pp. 158–165, 2011.

[57] W. K. Burton, N. Cabrera, and F. C. Frank, "The growth of crystals and the equilibrium structure of their surfaces.," *Philos. Trans. R. Soc. London*, vol. 19, pp. 35–50, 1951.

[58] I. M. Lifshitz and V. V. Slyozov, "The kinetics of precipitation from supersaturated solid solutions.," *J. Phys. Chem. solids*, vol. 19, pp. 35–50, 1961.

[59] R. Cortes-Huerto, J. Goniakowski, and C. Noguera, "An efficient many-body potential for the interaction of transition and noble metal nano-objects with an environment.," *J. Phys. Chem.*, vol. 138, p. 244 706, 2013.

[60] R. Cortes-Huerto, J. Goniakowski, and C. Noguera, "Role of the environment in the stability of anisotropic gold particles.," *Phys. Chem. Chem. Phys.*, vol. 17, pp. 6305–6313, 2015.

[61] S. Yuan, L. Ma, X. Zhang, and L. Zheng, "Molecular dynamics studies on monolayer of cetyltrimethylammonium bromide surfactant formed at the air/water interface.," *Colloids Surf, A.*, vol. 289, pp. 1–9, 2006.

[62] B. C. Stephenson, K. Beers, and D. Blankschtein, "Complementary use of simulations and molecular-thermodynamic theory to model micellization.," *Langmuir*, vol. 22, pp. 1500–1513, 2006.

[63] J. Bocker, J. Brickmann, and P. Bopp, "Molecular dynamics simulation study of an n-decyltrimethylammonium chloride micelle in water.," *J. Phys. Chem.*, vol. 98, pp. 712–717, 1994.

[64] S. Pal, B. Bagchi, and S. Balasubramanian, "Hydration layer of a cationic micelle, C10TAB: Structure, rigidity, slow reorientation, hydrogen bond lifetime, and solvation dynamics.," *J. Phys. Chem. B.*, vol. 109, pp. 12 879–12 890, 2005.

[65] G. Srinivas, S. O. Nielsen, P. B. Moore, and M. L. Klein, "Molecular dynamics simulations of surfactant self organization at a solid-liquid interface.," *J. Am. Chem. Soc.*, vol. 128, pp. 848–853, 2006.

[66] Q. Zeng, X. Jiang, A. Yu, and G. M. Lu, "Growth mechanisms of silver nanoparticles: A molecular dynamics study.," *Nanotechnology*, vol. 18, p. 035 708, 2007.

[67] S. Corni, M. Hnilova, C. Tamerler, and M. Sarikay, "Conformational behavior of genetically-engineered dodecapeptides as a determinant of binding affinity for gold.," *J. Phys. Chem. C*, vol. 117(33), pp. 16 990–17 003, 2013.

[68] L. B. Wright, J. P. Palafox-Hernandez, P. M. Rodger, S. Corni, and T. R. Walsh, "Facet selectivity in gold binding peptides: Exploiting interfacial water structure.," *J. Phys. Chem. C*, vol. 6, pp. 5204–5214, 2015.

[69] Z. Tang, Q. Zhang, Y. Yin, and C. A. Chang, "Facet selectivity of ligands on silver nanoplates: Molecular mechanics study.," *J. Phys. Chem. C*, vol. 118, pp. 21 589–21 598, 2014.

[70] K. C. Jha, H. Liu, M. R. Bockstaller, and H. Heinz, "Facet recognition and molecular ordering of ionic liquids on metal surfaces.," *J. Phys. Chem. C.*, vol. 117, pp. 25 969–25 981, 2013.

[71] D. Frenkel and B. Smit, *Understanding molecular simulation: From algorithms to applications.* San Diego, California: Academic press, 2002.

[72] L. Verlet, "Computer "experiments" on classical fluids. i. thermodynamical properties of Lennard-Jones molecules.," *Molecules. Phys. Rev.*, vol. 159, pp. 98–103, 1967.

[73] G. Bussi, D. Donadio, and M. Parrinello, "Canonical sampling through velocity rescaling.," *J. of Chem. Phys.*, vol. 126(1), p. 014 101, 2007.

[74] M. E. Tuckerman and G. J. Martyna, "Understanding modern molecular dynamics: Techniques and applications.," *J. Phys. Chem. B*, vol. 104, no. 2, pp. 159–178, 2000.

[75] J. Hermans, H. J. C. Berendsen, W. F. V. Gunsteren, and J. P. M. Postma, "A consistent empirical potential for water-protein interactions.," *Biopolymers*, vol. 23(8), pp. 1513–1518, 1984.

[76] C. Oostenbrink, A. Villa, A. E. Mark, and W. F. V. Gunsteren, "The gromos force-field parameter sets 53a5 and 53a6.," *J. Comput. Chem.*, vol. 25, pp. 1656–1676, 2004.

[77] Z. Wang and R. G. Larson, "Molecular dynamics simulations of thread-like cetyltrimethylammonium chloride micelles: Effects of sodium chloride and sodium salicylate salts.," *J. Phys. Chem. B.*, vol. 113, pp. 13 697–13 710, 2009.

[78] H. Yu, M. Ramseier, R. Burgi, and W. F. van Gunsteren, "Comparison of properties of aib-rich peptides in crystal and solution: A molecular dynamics study.," *Chem. Phys. Chem*, vol. 5(5), pp. 633–641, 2004.

[79] H. Heinz, R. A. Farmer, and R. R. Naik, "Accurate simulation of surfaces and interfaces of face-centered cubic metals using 12-6 and 9-6 Lennard-Jones potentials.," *J. Phys. Chem. B.*, vol. 112, pp. 17 281–17 290, 2008.

[80] M. M. Reif and P. H. Hunenberger, "Computation of methodology-independent single-ion solvation properties from molecular simulations. iv. optimized lennard-jones interaction parameter sets for the alkali and halide ions in water.," *J. Chem. Phys.*, vol. 134, p. 144 104, 2011.

[81] V. Dubois, M. Seijo, and P. Archirel, "On the absorption spectrum and stability of Ag^{2+}_3 in aqueous solution.," *Chem. Phys. Lett.*, vol. 389, pp. 150–154, 2004.

[82] P. E. Blöchl, "Electrostatic decoupling of periodic images of planewave-expanded densities and derived atomic point charges.," *J. Chem. Phys.*, vol. 103, p. 7422, 1995.

[83] H. Nakahara, O. Shibata, and Y. Moroi, "Examination of surface adsorption of cetyltrimethylammonium bromide and sodium dodecyl sulfate.," *J. Phys. Chem. B.*, vol. 115, pp. 9077–9086, 2011.

[84] H. Berendsen, D. van der Spoel, and R. van Drunen, "Gromacs: A message-passing parallel molecular dynamics implementation.," *Comput. Phys. Commun.*, vol. 91, pp. 43–56, 1995.

[85] D. V. D. Spoel, E. Lindahl, B. Hess, G. Groenhof, A. E. Mark, and H. J. C. Berendsen, "Gromacs: Fast, flexible, and free.," *J. Comput. Chem.*, vol. 26, pp. 1701–1718, 2005.

[86] B. Hess, C. Kutzner, D. V. D. Spoel, and E. Lindahl, "Gromacs 4: Algorithms for highly efficient, load-balanced, and scalable molecular simulation.," *J. Chem. Theory Comput.*, vol. 4, pp. 435–447, 2008.

[87] S. Pronk, S. Pall, R. Schulz, *et al.*, "Gromacs 4.5: A high-throughput and highly parallel open source molecular simulation toolkit.," *Bioinformatics*, vol. 29, pp. 845–854, 2013.

[88] G. F. Cata, H. C. Rojas, A. P. Gramatges, C. M. Zicovich-Wilson, L. J. Alvarez, and C. Searle, "Initial structure of cetyltrimethylammonium bromide micelles in aqueous solution from molecular dynamics simulations.," *Soft Matter*, vol. 7, pp. 8508–8515, 2011.

[89] J. Feng, R. B. Pandey, R. J. Berry, B. L. Farmer, R. R. Naikc, and H. Heinz, "Adsorption mechanism of single amino acid and surfactant molecules to Au(111) surfaces in aqueous solution: Design rules for metal binding molecules.," *Soft Matter*, vol. 7, pp. 2113–2120, 2011.

[90] J. Feng, J. M. Slocik, M. Sarikaya, R. R. Naik, B. L. Farmer, and H. Heinz, "Influence of the shape of nanostructured metal surfaces on adsorption of single peptide molecules in aqueous solution.," *Small*, vol. 8, pp. 1049–1059, 2012.

[91] H. Heinz, "Computational screening of biomolecular adsorption and self-assembly on nanoscale surfaces.," *J. Comput. chem.*, vol. 130, pp. 1564–1568, 2010.

[92] S. G. Grana, F. Hubert, F. Testard, A. G. Martinez, I. Grillo, L. M. Marzan, and O. Spalla, "Surfactant (bi) layers on gold nanorods.," *Langmuir*, vol. 28, pp. 1453–1459, 2012.

[93] L. Zhong, X. zhou, S. Bao, Y. Shi, Y. Wang, S. Hong, Y. Huang, X. Wang, Z. Xie, and Q. Zhang, "Rational design and sers properties of side-by-side, end-to-end and end-to-side assemblies of au nanorods.," *J. Mater. Chem*, vol. 21, pp. 14 448–14 455, 2011.

[94] N. R. Jana, L. A. Gearheart, S. O. Obare, C. J. Johnson, K. J. Edler, S. Mann, and C. J. Murphy, "Liquid crystalline assemblies of ordered gold nanorods.," *J. Mater. Chem.*, vol. 12, pp. 2909–2912, 2002.

[95] T. S. Sreeprasad, A. K. Samal, and T. Pradeep, "One-, two-, and three-dimensional superstructures of gold nanorods induced by dimercaptosuccinic acid.," *Langmuir*, vol. 24, pp. 4589–4599, 2008.

[96] H. Kawasaki, K. Nishimura, and R. Arakawa, "Influence of the counterions of cetyltrimetylammonium salts on the surfactant adsorption onto gold surfaces and the formation of gold nanoparticles.," *J. Phys. Chem. C*, vol. 111, pp. 2683–2690, 2007.

[97] A. A. Gurtovenko and I. Vattulainen, "Calculation of the electrostatic potential of lipid bilayer from molecular dynamics simulations: Methodological issue.," *J. Chem. Phys.*, vol. 130, pp. 215 107–215 114, 2009.

[98] B. Goris, S. Bals, W. V. den Broek, E. Carbo-Argibay, S. Gomez-Grana, L. M. Liz-Marzan, and G. V. Tendeloo, "Atomic-scale determination of surface facets in gold nanorods.," *Nat. Meter.*, vol. 11, pp. 930–935, 2012.

[99] Z. Wang, M. Mohamed, S. Linkb, and M. El-Sayedb, "Crystallographic facets and shapes of gold nanorods of different aspect ratios.," *Surf. sci.*, vol. 440, pp. 809–814, 1999.

[100] H. Katz-Boon, M. Walsh, C. Dwyer, P. Mulvaney, A. M. Funston, and J. Etheridge, "Stability of crystal facets in gold nanorods.," *Nano Lett.*, vol. 15(3), pp. 1635–1641, 2015.

[101] A. B. Shah, S. T. Sivapalan, B. M. DeVetter, T. K. Yang, J. Wen, R. Bhargava, C. J. Murphy, and J.-M. Zuo, "High-index facets in gold nanocrystals elucidated by coherent electron diffraction.," *Nano Lett.*, vol. 13(4), pp. 1840–1846, 2013.

[102] S. K. Meena and M. Sulpizi, "Understanding the microscopic origin of gold nanoparticle anisotropic growth from molecular dynamics simulations.," *Langmuir*, vol. 29 (48), pp. 14 954–14 961, 2013.

[103] M. J. Walsh, S. J. Barrow, W. Tong, A. M. Funston, and J. Etheridge, "Symmetry breaking and silver in gold nanorod growth.," *ACS Nano*, vol. 9(1), pp. 715–724, 2015.

[104] C. J. Murphy, L. B. Thompson, A. M. Alkilany, P. N. Sisco, S. P. Boulos, S. T. Sivapalan, J. A. Yang, D. J. Chernak, and J. Huang, "The many faces of gold nanorods.," *J. Phys. Chem. Lett.*, vol. 1 (19), pp. 2867–2875, 2010.

[105] N. Almora-Barrios, G. Novell-Leruth, P. Whiting, L. M. Liz-Marzán, and N. López, "Theoretical description of the role of halides, silver, and surfactants on the structure of gold nanorods.," *Nano Lett.*, vol. 14(2), pp. 871–875, 2014.

[106] H. Heinz, B. L. Farmer, R. B. Pandey, J. M. Slocik, S. S. Patnaik, R. Pachter, and R. R. Naik, "Nature of molecular interactions of peptides with gold, palladium, and Pd-Au bimetal surfaces in aqueous solution.," *J. Am. Chem. Soc.*, vol. 131, pp. 9704–9714, 2009.

[107] C. Rosman, J. Prasad, A. Neiser, A. Henkel, J. Edgar, and C. Sönnichsen, "Multiplexed plasmon sensor for rapid label-free analyte detection.," *Nano Lett.*, vol. 13(7), pp. 3243–3247, 2013.

[108] J. Olson, S. Dominguez-Medina, A. Hoggard, L.-Y. Wang, W.-S. Chang, and S. Link, "Optical characterization of single plasmonic nanoparticles.," *Chem. Soc. Rev.*, vol. 44, pp. 40–57, 2015.

[109] J. Lipkowski, Z. Shi, A. Chen, B. Pettinger, and C. Bilger, "Ionic adsorption at the au(111) electrode.," *Electrochim. Acta*, vol. 43, pp. 2875–2888, 1998.

[110] O. M. Magnussen, "Ordered anion adlayers on metal electrode surfaces.," *Chem. Rev.*, vol. 102, pp. 679–725, 2002.

[111] P. Jungwirth and D. J. Tobias, "Specific ion effects at the air/water interface.," *Chem. Rev.*, vol. 106, pp. 1259–1281, 2006.

[112] D. Horinek and R. R. Netz, "Specific ion adsorption at hydrophobic solid surfaces.," *Phys. Rev. Lett.*, vol. 99, p. 226 104, 2007.

[113] C. Yu, L. Varghese, and J. Irudayaraj, "Surface modification of cetyl tri methyl ammonium bromide-capped gold nanorods to make molecular probes.," *Langmuir*, vol. 23, pp. 9114–9119, 2007.

[114] A. A. Ashkarran and A. Bayat, "Surface plasmon resonance of metal nanostructures as a complementary technique for microscopic size measurement.," *Int. Nano Lett.*, vol. 3, p. 50, 2013.

[115] U. Hohenester and A. Trügler, "Mnpbem-a matlab toolbox for the simulation of plasmonic nanoparticles.," *Comput. Phys. Commun.*, vol. 183, pp. 370–381, 2012.

[116] M. Liu and P. Guyot-Sionnest, "Mechanism of silver(i)-assisted growth of gold nanorods and bipyramids.," *J. Phys. Chem. B*, vol. 109, pp. 22192–22 200, 2005.

[117] Y. Niidome, Y. Nakamura, K. Honda, Y. Akiyama, K. Nishioka, H. Kawasakic, and N. Nakashima, "Characterization of silver ions adsorbed on gold nanorods: Surface analysis by using surface-assisted laser desorption/ionization time-of-flight mass spectrometry.," *Chem. Commun.*, vol. (Cambridge U.K.) Pp. 1754–1756, 2009.

[118] S. R. Jackson, J. R. McBride, S. J. Rosenthal, and D. W. Wright, "Where's the silver? Imaging trace silver coverage on the surface of gold nanorods.," *J. Am. Chem. Soc*, vol. 136 (14), pp. 5261–5263, 2014.

[119] N. R. Jana, L. Gearheart, and C. J. Murphy, "Seed-mediated growth approach for shape-controlled synthesis of spheroidal and rod-like gold nanoparticles using a surfactant template.," *Adv, Mater.*, vol. 13 (18), pp. 1389–1393, 2001.

[120] R. Michalitsch, B. J. Palmer, and P. E. Laibinis, "Formation of a more noble underpotentially deposited silver layer on gold by the adsorption of chloride.," *Langmuir*, vol. 16 (16), pp. 6533–6540, 2000.

[121] C. J. Orendorff and C. J. Murphy, "Quantitation of metal content in the silver-assisted growth of gold nanorods.," *J. Phys. Chem. B*, vol. 110(9), pp. 3990–3994, 2006.

[122] M. H. Kowsari, S. Alavi, M. Ashrafizaadeh, and B. Najafi, "Molecular dynamics simulation of imidazolium-based ionic liquids. i. dynamics and diffusion coefficient.," *J. Chem. Phys.*, vol. 129, p. 224 508, 2008.

[123] G. J. Nusz, A. C. Curry, S. M. Marinakos, A. Wax, and A. Chilkoti, "Rational selection of gold nanorod geometry for label-free plasmonic biosensors.," *ACS Nano*, vol. 3, pp. 795–806, 2009.

[124] A. Henkel, *Rod-shaped plasmonic sensors : Synthesis and single particle spectroscopy.* Universität Mainz, Zentralbibliothek, 2014, XII 125 S.